Astronomy Letters, Vol. 29, No. 2, 2003, pp. 105–110. Translated from Pis'ma v Astronomicheskiĭ Zhurnal, Vol. 29, No. 2, 2003, pp. 125–131.

Variability of the Hα and Na I D Line Profiles in the Spectrum of FU Ori

L. Errico[1], A. Vittone[1], and S. A. Lamzin[2]*

[1] *Capodimonte Astronomical Observatory, Naples, Italy*

[2] *Sternberg Astronomical Institute, Universitetskiĭ pr. 13, Moscow, 119992 Russia*

Received August 13, 2002

Abstract—The variations of line profiles in the spectrum of FU Ori during several consecutive nights, from January 3 through January 8, 1999, have been traced for the first time in the entire history of studying this star. The variations of the Hα and Na I D line profiles are regular in pattern; at each time, the profiles of these lines were similar to a particular profile observed previously, suggesting that the phenomenon is periodic. We argue that the profile variations result from the axial rotation of the inner accretion-disk and disk-wind regions for which the temperature distribution and the wind-streamline orientation are not axisymmetric. The cause of the asymmetry could be the interaction of circumstellar matter with the stellar magnetic field if the magnetic axis is greatly inclined to the rotation axis. The possible binary nature of FU Ori seems a less likely cause of the asymmetry. © *2003 MAIK "Nauka/Interperiodica".*

Key words: *stars—variable, peculiar, and young, FU Ori.*

INTRODUCTION

FU Ori is the prototype of a subclass of young stars in which a brightening by 4^m–6^m over a period of less than ten years was observed (Herbig 1966, 1977). A large increase in the rate of accretion from the disk around a T Tauri star is currently believed to be responsible for its outburst [see Hartmann and Kenyon (1996) and references therein]. As a result, the accretion luminosity is several hundred times higher than the luminosity of the central star. Therefore, the observed spectrum of FU Ori objects is an accretion-disk spectrum.

The α-disk model (Shakura and Sunyaev 1973) allowed the following major features of the FU Ori spectra to be explained not only qualitatively but also quantitatively: the dependence of spectral type on the spectral range under study, the decrease in the width of absorption lines with increasing wavelength, and the double-peaked structure of their profiles. However, the α-disk model predicts that the gas temperature $T_{\rm bl}$ in the boundary layer between the star and the disk exceeds 10^4 K, whereas Kenyon *et al.* (1989) found no evidence of emission from such a hot gas in the wavelength range 2600–3200 Å when studying the IUE spectra of FU Ori star.

To overcome this contradiction, Popham *et al.* (1993, 1996) suggested taking into account advection (the so-called slim model) when describing the structure of the inner disk regions in FU Ori stars. Based on their model, these authors were able to reproduce the observed ultraviolet spectral energy distribution of FU Ori with the following parameters: an accretion rate $\dot{M}_{\rm a} \simeq 2 \times 10^{-4} M_\odot$ yr^{-1}, a stellar mass $M_* \simeq 0.7 M_\odot$, a stellar radius $R_* \simeq 5.8 R_\odot$, and a stellar rotation period $P \simeq 8.5$ days. For these parameters, the maximum temperature is $T_{\rm bl}^{\rm max} = T_{\rm R=2.2R_*} \simeq 8200$ K, in agreement with the IUE observations.

The accuracy of the parameters obtained for FU Ori by Popham *et al.* (1993, 1996) should not be overestimated, because their model contains a number of simplifying assumptions. In particular, in describing accretion, the authors disregarded the disk-wind contribution to the balance of energy and angular momentum. Meanwhile, the Balmer lines, along with the Na I D and Ca II K in the spectrum of FU Ori, exhibit deep and broad P Cyg profiles, suggesting an intense mass outflow from the neighborhoods of the star (see Fig. 1 and Herbig 1966; Bastian and Mundt 1985; Croswell *et al.* 1987; Welty *et al.* 1992). Croswell *et al.* (1987) estimated the mass loss rate to be $\sim 10^{-5} M_\odot$ yr^{-1}. This estimate was obtained under the assumption of a spherically symmetric wind, but Calvet *et al.* (1993) obtained the same value in a more realistic (cylindrical) geometry. Hartmann and Calvet (1995) gave convincing arguments for the outflow from the surface of a Keplerian disk.

According to Calvet *et al.* (1993), the wind observed in optical lines blows from the inner ($R \leq 3 \times 10^{12}$ cm) accretion-disk regions, with the outflowing

*E-mail: lamzin@sai.msu.ru

1063-7737/03/2902-0105$24.00

gas having a low temperature ($T_w < 6000$ K) and a high density ($N \sim 10^{12}$–10^{13} cm^{-3}). To explain the presence of emission components in the Hα, Na I D, Ca II K, and Mg II h, k lines, D'Angelo *et al.* (2000) assumed that there were regions with temperature inversion (chromosphere) at the wind base. Using a phenomenological model, they were able to reproduce the observed Hα profiles in the spectrum of FU Ori with a reasonable accuracy by assuming that the wind streamlines and the line of sight were perpendicular to the disk.

D'Angelo *et al.* (2000) interpreted the observed variations of the Hα profile as resulting from axysymmetric variations in the physical parameters of the wind or, to be more precise, in the temperature and velocity distributions along streamlines. Here, our goal is to present new observational data showing that the variations of the Hα and Na I D line profiles in the spectrum of FU Ori follow a certain pattern. We also consider the possible causes of this phenomenon.

OBSERVATIONS

The optical spectra of FU Ori were observed on each night from January 3 through January 8, 1999. The spectra were taken with a Reosc echelle spectrograph and a 1.82-m telescope at the Padova Astronomical Observatory at Mount Ecar near the town of Asiago (Italy). The detector was a Thompson THX 31156 1024 × 1024 CCD array with a pixel size of 19 μm. The dispersion of the spectra near the Na I D and Hα lines was 9.1 and 10.2 Å mm^{-1}, respectively. The Na I D and Hα line profiles obtained during our observations are shown in Fig. 1.

The high-resolution IUE ultraviolet spectra were retrieved from the INES database (http://ines.laeff.esa.es) and were not subjected to additional reduction. Since the spectra had a low signal-to-noise ratio, we were able to obtain information only on the Mg II line profiles near 2800 Å. Figure 2 shows the profiles of the h (2802.77 Å) and k (2795.59 Å) uv1 multiplet lines and the 2790.84 Å uv3 multiplet line (below, all wavelengths are given for air). The 2790.84 Å line profile for spectrum LWR 16741 is not shown because of the low signal-to-noise ratio. Spectra LWR 13943, LWR 16741, and LWP 12005 were taken on August 14, 1982 (UT 02:30), September 5, 1983 (UT 21:50), and October 3, 1987 (UT 20:39), respectively.

DISCUSSION

It follows from Fig. 1 that, over the period of our observations, the Hα and Na I D line profiles varied not randomly but with a certain pattern. In all three lines, the width of the absorption component initially decreased but subsequently, having reached a minimum, began to increase. For Hα, the intensity of the emission component also varied synchronously. To quantitatively describe the variability of the Hα profile, we introduce a quantity $W_{1/2}$, the width of the absorption component in the line at $(I_{max} + I_{min})/2$, where I_{max} is the maximum intensity of its emission component and I_{min} is the minimum intensity of its absorption component. It is important to note that $W_{1/2}$ does not depend on the level of the continuum whose location in the spectrum of FU Ori is determined with a low accuracy.

Figure 3 shows how $W_{1/2}$ varied between January 3 and January 8, 1999: we clearly see a regular pattern of variations in the Hα profile. It is important to note that all of the Hα profiles found in the literature [see D'Angelo *et al.* (2000) and references therein]) have the same shape as the profiles in Fig. 1. Having measured $W_{1/2}$ for the published profiles, we found the following: in all cases, it lay within the same range as that for our spectra and only in one case did it slightly exceed our observed maximum value. These findings suggest that the variations of the Hα and Na I D line profiles in the spectrum of FU Ori are periodic in pattern.

The following two factors can be responsible for the (quasi-)periodic variations in the profiles of the lines under considerations: (1) azimuthally nonuniform structure of the axially rotating disk and the disk wind and (2) synchronous variations in the parameters of the disk and the disk wind with axial symmetry. To choose between these cases, let us consider the pattern of variations in the ultraviolet Mg II line profiles with time.

Let us first consider the Mg II h and k resonance lines shown in Fig. 2. In contrast to the Hα and Na I D lines, the uv1 doublet lines always exhibit an emission component whose intensity is variable (Kenyon *et al.* 1989). The IUE sensitivity is too low to judge the continuum level in FU Ori near 2800 Å. However, we are sure that the Mg II h and k lines have P Cyg profiles, because the Ca II K line has such a profile [see Fig. 3 from Bastian and Mundt (1985)] and the profile of its emission component is identical to the profiles of the emission components of the h and k lines.

The continuum of FU Ori is formed in the disk (Hartmann and Kenyon 1996), i.e., precisely where the wind originates. Therefore, it would be natural to assume that the observed shape of the Mg II h, k, and Ca II K line profiles results from a superposition of the blue absorption feature formed in the wind on the broad, initially more or less symmetric emission line formed at the outflow base (see also D'Angelo *et al.*

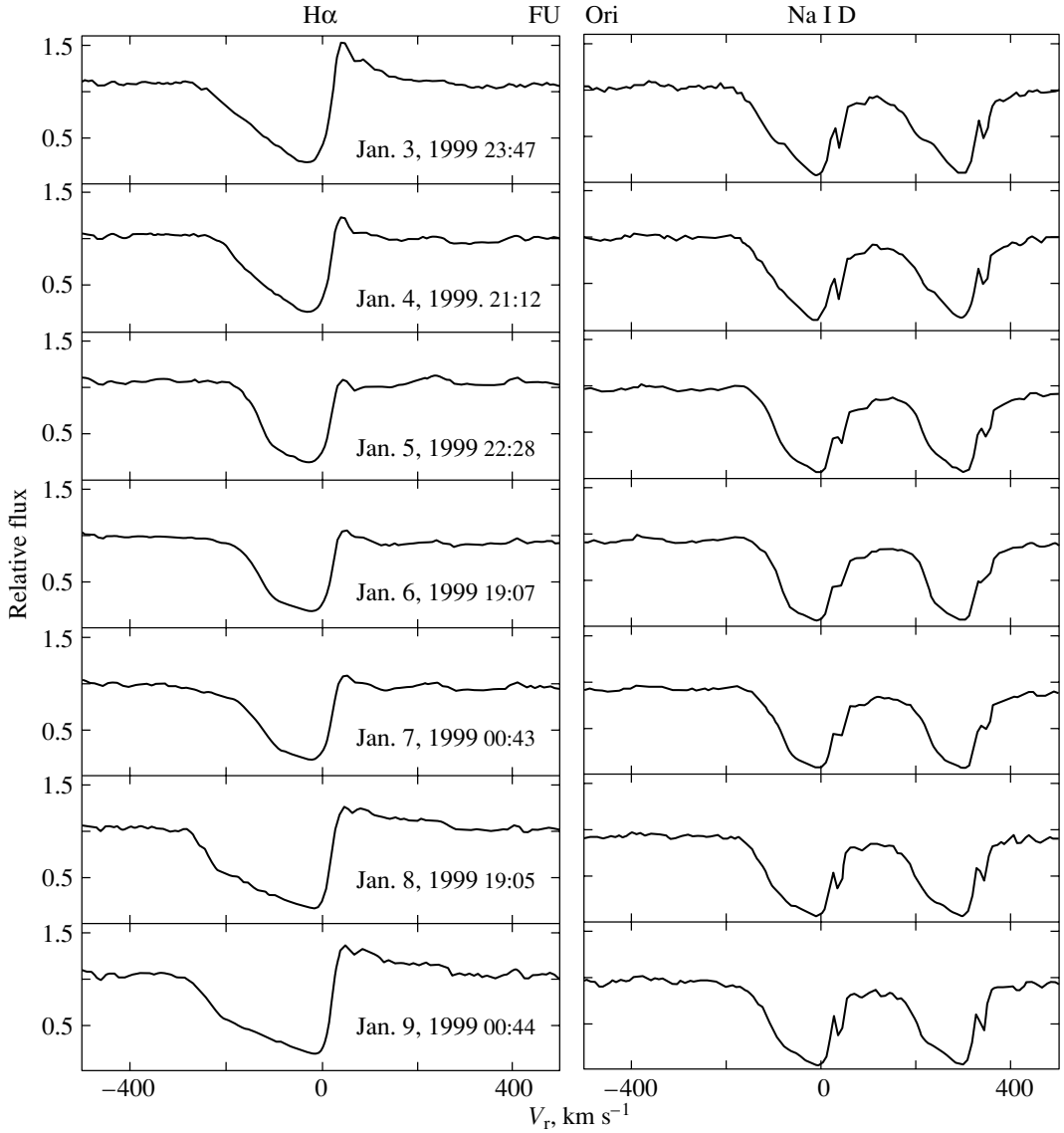

Fig. 1. Variations of the Hα and Na I D line profiles in the spectrum of FU Ori from January 3 through January 8, 1999.

2000). We can give an additional argument for this assumption. According to Herbig (1966), the Ca II H line has no emission component (although the Ca II K line has such a component) probably because the blue absorption wing of the Hε line is superimposed on it. The wavelength difference between the Ca II H and Hε lines, in units of velocity, is 120 km s^{-1}; i.e., it is smaller than the length of the Balmer-line absorption wings [see Fig. 1 here and Fig. 7 from Welty *et al.* (1992)]. Thus, the emission components of the Ca II H line and, most likely, the Mg II h, k, and Hα lines are formed behind the region occupied by the wind along the line of sight, i.e., in the inner regions of the accretion disk and/or the boundary layer. Below, the emission-component formation region is called the E region.

Figure 4 shows part of the Grotrian diagram for Mg II on which the subordinate uv3 multiplet lines are marked by letters a, b, and c. The b (2790.84 Å) line in the spectrum of FU Ori has an abnormally high intensity: it is more than an order of magnitude stronger than the a and c lines and only a factor of 3 to 6 weaker than the h and k resonance lines. The excitation of the $^2D_{3/2}$ upper level of the b line by k-line photons is probably responsible for this phenomenon.[1] Since the b and k lines are comparable in intensity, it should be recognized that the excitation is

[1] As we see from Fig. 4, $^2D_{3/2}$ is also the upper level for the a line, but the transition probability for this line is approximately a factor of 5 lower than that for the b line (van Hoof 2002).

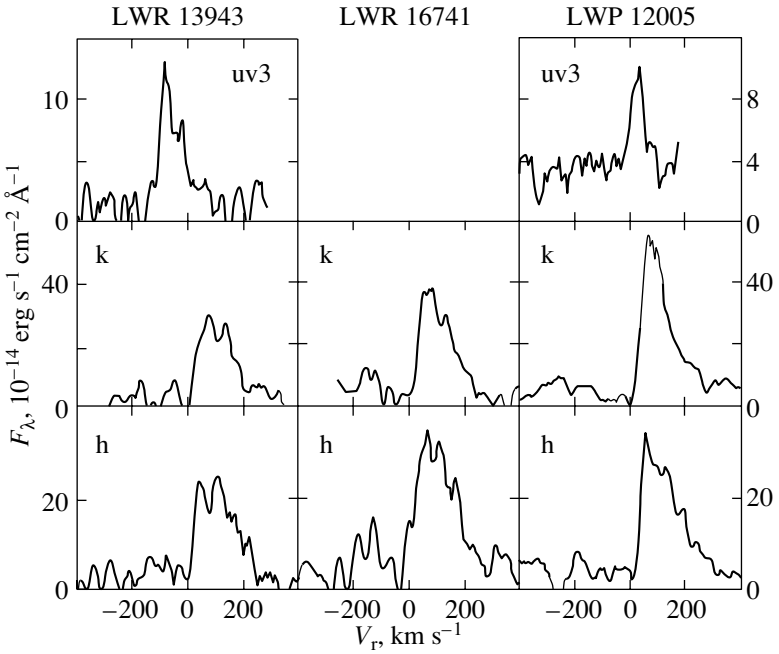

Fig. 2. The ultraviolet Mg II line profiles in the spectrum of FU Ori.

produced by photons of the central part of the k-line profile. The wavelength difference between the k and b lines, in units of velocity, is $\simeq$280 km s^{-1}. It thus follows that the b-line formation region recedes from the E region, where the k line is formed, at a velocity close to 280 km s^{-1}: under this condition, in the frame of reference associated with the moving gas, the energy of the k photon that arrives from the outside is equal to the energy difference between the b-line levels and the $^2D_{3/2}$ level is excited most effectively.

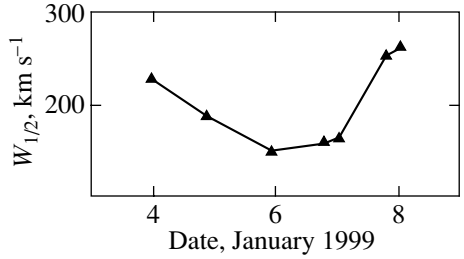

Fig. 3. Variations in the characteristic Hα width $W_{1/2}$ from January 3 through January 8, 1999.

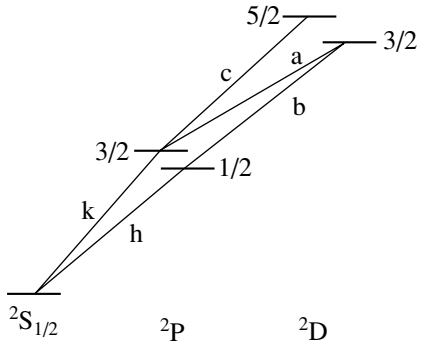

Fig. 4. Part of the Grotrian diagram for Mg II.

Thus, it would be reasonable to assume that the b line originates in the matter outflowing from the neighborhoods of the star, i.e., in the disk wind. To be more precise, this line originates in the part (b region) that moves relative to the E region at a velocity of about 280 km s^{-1}. At the same time, we see from Fig. 2 that the FWHM of the b-line profile is $\leq$50 km s^{-1}. An even more surprising result is that the radial velocity determined from the b-line peak is variable: the radial-velocity difference between the b-line intensity peak and the absorption spectral lines is nearly zero in spectrum LWP 12005 but reaches almost 100 km s^{-1} in spectrum LWR 13943.[2]

We see no reason why such a large shift in the b line can arise if it is formed in an axisymmetric region. However, the observed features of the b-line profiles can be naturally explained if the wind is not axisymmetric and if the b line is formed in a region confined within a narrow range of azimuthal angles $\Delta\varphi$. In this case, the radial velocity of the b line must vary because of the different orientation of the

[2]Here, we took into account the fact that the radial velocity of FU Ori determined from optical absorption lines is +28 km s^{-1} (Hartmann and Kenyon 1987).

b region relative to the observer as the disk and its associated wind rotate. This interpretation primarily suggests that the streamline orientation in the disk wind is asymmetric. It would be natural to assume that the variations of the H_α and Na I D line profiles are also attributable to the rotational modulation of an asymmetric disk wind. Since the variations in the shape of the absorption components of these lines are accompanied by variations in the intensity of their emission components, we conclude that the thermal structure of the inner disk regions (E region) is not axisymmetric either (see Fig. 5).

Since the gas velocity in the b region is $\simeq 280$ km s^{-1}, its streamlines were almost perpendicular to the line of sight when spectrum LWP 12005 was taken and were inclined to the line of sight at an angle of about 70° when spectrum LWR 13943 was taken. However, we cannot estimate the streamline inclination in the b region relative to the disk plane from our data or determine the azimuthal extent of the region $\Delta\varphi$ from the observed 2790.84-Å line width, because we do not know the phase at which the IUE spectra were taken.

We can say even less about the streamline orientation outside the b region. Therefore, it makes sense to postpone discussing the disk-wind streamline topology and the azimuthal dependence of the temperature in the E region until new observational data will appear. Instead, we consider the possible causes of the asymmetric disk and wind structure in FU Ori.

Our data are too scarce to answer the question of whether the variations of the Hα and Na I D line profiles are strictly periodic. However, if they are periodic, then the rotation period of the region in which the lines under consideration are formed must exceed 5–6 days; i.e., it must be close to the rotation period of the central star $P \simeq 8.5^d$ (Popham *et al.* 1996). This circumstance prompted us to consider the effect of the stellar magnetic field on the structure of the inner regions in the disk and the disk wind.

According to Shu *et al.* (2000), a dipole stellar magnetic field limits the inner accretion-disk radius to

$$R_x \simeq \left(\frac{B_e^4 R_*^{12}}{GM_*\dot{M}_a^2}\right)^{1/7}, \qquad (1)$$

where B_e is the magnetic-field strength on the stellar equator. In the case of FU Ori, the magnetic field probably does not destroy the disk, and it reaches the stellar surface. However, if we substitute R_* for R_x in (1), then we can determine B_e at which the field is

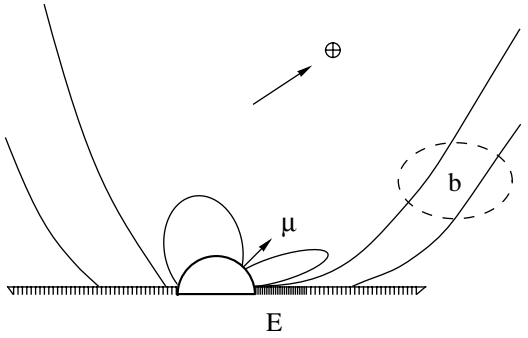

Fig. 5. A schematic view of the FU Ori neighborhoods. The star, its surrounding disk (hatched region), stellar magnetic field lines, and disk-wind streamlines are shown. The emission components of the lines (E region) are formed in the more densely hatched disk region, while the b and Mg II lines are formed in the wind region bounded by the dashed oval. The arrows indicate the direction of the Earth ⊕ and the orientation of the stellar magnetic axis μ.

capable of controlling the gas motion in the disk near the stellar surface and in the disk wind:

$$B_e \simeq \frac{G^{1/4}M_*^{1/4}\dot{M}_a^{1/2}}{R_*^{5/4}}.$$

Substituting M_*, R_*, and $\dot{M}_a$ from Popham *et al.* (1996) into this relation yielded $B_e \sim 2$ kG, a value typical of the T Tauri stars (Guenther *et al.* 1999; Johns-Krull *et al.* 1999). Thus, if the field strength on the FU Ori surface exceeds 1 kG and if the magnetic axis is appreciably inclined to the rotation axis, then the structure of the inner regions in the disk and the disk wind will most likely be nonaxisymmetric.

Based on this hypothesis, we might expect the degree of asymmetry to decrease with distance from the star and the disk and the wind must be axisymmetric at large distances. We found from the relation $B^2/8\pi = \rho V^2/2$ and from the wind parameters determined by Calvet *et al.* (1993) that a magnetic field with strengths of $\sim$200 and 25 G is enough to control the motion of the outflowing gas near the inner and outer wind boundaries, respectively. Thus, if $B_e \sim 2$ kG and $B \propto R^{-3}$, then the stellar magnetic field can affect the orientation of the wind streamlines almost up to its outer boundary.

Alternatively, the binary nature of FU Ori can cause the disk and wind asymmetry: through the tidal interaction of the companion with the matter surrounding the central star. In this case, the outer disk and wind regions must be subjected to the strongest distortion and the orbital period of the binary system must be the variation time scale of the line profiles. While observing FU Ori with the Palomar Testbed Interferometer at a wavelength of 2.2 μm, Malbet

et al. (1998) found that the star was not a pointlike source. The data obtained admit a two-fold interpretation: the star can appear as an extended source because it is surrounded by an accretion disk and because it has a companion. If the star is binary, the separation between its components cannot be less than 0.3 AU and its orbital period $P_{\rm orb}$ must exceed $60(M/M_\odot)^{-1/2}$ days, where M is the total mass of the binary system. This value of $P_{\rm orb}$ is almost an order of magnitude larger than the variation time scale of the Hα and Na I D line profiles. Therefore, it seems less likely that the binary nature of FU Ori is responsible for the asymmetric structure of its disk and wind.

CONCLUSIONS

To explain the regular pattern of variations in the Hα and Na I D line profiles that we observed from January 3 through January 8, 1999, we assume that they are (quasi-)periodic and have a period equal to the rotation period of the star. Having analyzed the ultraviolet Mg II line profiles, we concluded that the variability of the optical and ultraviolet line profiles arose from the rotation of the disk and wind whose azimuthal structure is not axisymmetric. Asymmetry can result from the interaction of the stellar magnetic field with circumstellar matter if the stellar field strength is $\geq$1 kG and if the magnetic axis is greatly inclined to the rotation axis. We cannot rule out the possibility that the asymmetry is due to the binary nature of FU Ori. However, this interpretation seems less plausible.

For the structure of the disk wind and the E region in FU Ori to be determined, we must have much more observational data than we have at our disposal. First, it should be established whether the variations of the Hα and Na I D line profiles are periodic and if they are periodic, then what their period is. In our view, the parameter $W_{1/2}$ introduced here can be used for these purposes. We are sure that a systematic study of the variations in the Ca II H and K line profiles and analysis of high-quality spectra at wavelengths shorter than 3000 Å will yield much useful information.

In conclusion, note the absorption feature that is superimposed on the emission component of the Hα line [see Fig. 1 here and Fig. 1 from Bastian and Mundt (1985)]. The depth of this feature increases with increasing intensity of the emission peak in Hα, implying that the feature originates in the region between the E region and the observer. Unfortunately, because of the low spectral resolution and low signal-to-noise ratio, we were unable to unequivocally identify this feature. However, we can assert that its wavelength does not vary with time, which seems quite strange.

ACKNOWLEDGMENTS

We wish to thank the referee for valuable remarks and V.M. Lipunov for helpful discussions. S. Lamzin is also grateful to the Russian Foundation for Basic Research (project no. 02-02-16070).

REFERENCES

1. U. Bastian and R. Mundt, Astron. Astrophys. **144**, 57 (1985).
2. N. Calvet, L. Hartmann, and S. J. Kenyon, Astrophys. J. **402**, 623 (1993).
3. K. Croswell, L. Hartmann, and E. H. Avrett, Astrophys. J. **312**, 227 (1987).
4. G. D'Angelo, L. Errico, M. T. Gomez, *et al.*, Astron. Astrophys. **356**, 888 (2000).
5. E. Guenther, H. Lehmann, J. P. Emerson, and J. Staude, Astron. Astrophys. **341**, 768 (1999).
6. L. Hartmann and N. Calvet, Astron. J. **109**, 1846 (1995).
7. L. Hartmann and S. J. Kenyon, Astrophys. J. **312**, 243 (1987).
8. L. Hartmann and S. J. Kenyon, Annu. Rev. Astron. Astrophys. **34**, 207 (1996).
9. G. H. Herbig, Vistas Astron. **8**, 109 (1966).
10. G. H. Herbig, Astrophys. J. **217**, 693 (1977).
11. C. M. Johns-Krull, J. A. Valenti, and C. Koresko, Astrophys. J. **516**, 900 (1999).
12. S. J. Kenyon, L. R. Hartmann, C. L. Imhoff, and A. Cassatella, Astrophys. J. **344**, 925 (1989).
13. F. Malbet, J.-P. Berger, M. M. Colavita, *et al.*, Astrophys. J. Lett. **507**, L149 (1998).
14. R. Popham, R. Narayan, L. R. Hartmann, and S. J. Kenyon, Astrophys. J. Lett. **415**, L127 (1993).
15. R. Popham, S. J. Kenyon, L. R. Hartmann, and R. Narayan, Astrophys. J. **473**, 422 (1996).
16. N. I. Shakura and R. A. Sunyaev, Astron. Astrophys. **24**, 337 (1973).
17. F. H. Shu, J. R. Najita, H. Shang, and Z.-Y. Li, in *Protostars and Planets IV,* Ed. by V. Mannings, A. P. Boss, and S. S. Russell (Univ. of Arizona Press, Tucson, 2000), p. 789.
18. P. van Hoof, *The Atomic Line List Database,* www.pa.uky.edu/~peter/atomic (2002).
19. A. D. Welty, S. E. Strom, S. Edwards, *et al.*, Astrophys. J. **397**, 260 (1992).

Translated by V. Astakhov

Astronomy Letters, Vol. 29, No. 2, 2003, pp. 111–115. Translated from Pis'ma v Astronomicheskiĭ Zhurnal, Vol. 29, No. 2, 2003, pp. 132–136.

Role of Anisotropy of the Initial Particle Distribution in the Acceleration in Collapsing Solar-Flare Traps

V. A. Kovalev[1]* and B. V. Somov[2]

[1] *Institute of Terrestrial Magnetism, Ionosphere, and Radiowave Propagation, Russian Academy of Sciences, Troitsk, Moscow oblast, 142190 Russia*

[2] *Sternberg Astronomical Institute, Universitetskiĭ pr. 13, Moscow, 119992 Russia*

Received May 20, 2002

Abstract—We consider the behavior of charged particles with an anisotropic initial velocity distribution in a magnetic trap with approaching mirrors in connection with the problem of particle acceleration in solar flares. We show that, irrespective of the charge sign, the efficiency of confinement and acceleration increases with increasing anisotropy factor of the initial distribution $\alpha = (T_\perp/T_{||})^{1/2}$. For a positive electric potential of the trap plasma relative to the mirrors, the emerging additional effect of ion expulsion form the trap increases with α_i. The derived estimate of the electric potential suggests an amplification of the initial perturbation and the development of instability. © *2003 MAIK "Nauka/Interperiodica".*

Key words: *solar flares, magnetic traps, trapping coefficient, anisotropy parameter, electric potential, particle confinement region.*

INTRODUCTION

This work is a continuation of our study of the effect of electric fields on the acceleration of charged particles in collapsing magnetic traps with converging magnetic mirrors (Kovalev and Somov 2002). Such traps can be produced by fast magnetic reconnection during the impulsive phase of solar flares (Somov and Kosugi 1997; Bogashev and Somov 2001). The trapped particles are accelerated when they are reflected from the magnetic mirrors (the Fermi acceleration mechanism of the first order) located at the intersection of the trap magnetic lines with a shock front or at the footpoints of flare loops, where the magnetic field becomes stronger as its photospheric sources are approached. In the above paper (Kovalev and Somov 2002), we formulated and investigated the problem of the effect of a specified electric potential on the particle acceleration in a simple mirror trap with a decreasing length l. We showed that, for an isotropic Maxwellian distribution of injected particles in the presence of a positive electrostatic potential of the trap relative to the mirrors, the efficiency of confinement and acceleration increased for electrons and decreased for ions compared to the case without an electric field. This effect results from the change in the shape of the boundary of the particle confinement region in a trap with an electric potential. Instead of a cone in velocity space, the confinement region becomes a two-sheet hyperboloid for electrons and a one-sheet hyperboloid for ions (Pastukhov 1984).

Meanwhile, according to current theoretical views, the most probable distributions of the particles injected into a trap are anisotropic. This anisotropy is attributable to the conditions of particle energization (heating and acceleration) in a high-temperature turbulent current sheet (Somov 1992) and escape of fast particles from the current sheet [see the monograph of Somov (2000) for a discussion of the problem]. In addition, according to Spicer and Emslie (1998), the magnetic-trap electric potential itself results from anisotropy of the trapped and precipitating particles. The kinetic processes in a dynamic collapsing trap can generate strong electric fields that affect the Fermi acceleration mentioned above. The question arises as to the statement of a self-consistent problem in which the electric potential depends on the particle distributions. This problem is more general and is naturally of interest in the physics of solar flares, particularly in interpreting the latest Yohkoh and HESSI X-ray observational data.

THE DISTRIBUTION OF INJECTED PARTICLES

We use the following anisotropic Maxwellian distributions as the distribution functions of injected charged particles [electrons (e) and ions (i)]:

$$f_0^{e,i}(v_{||}, v_\perp) = f_{0||}^{e,i}(v_{||}), f_\perp^{e,i}(v_\perp), \qquad (1)$$

*E-mail: vkovalev@izmiran.troitsk.ru

1063-7737/03/2902-0111$24.00

where

$$f_{0||}^{e,i}(v_{||}) = \frac{\exp\left(-v_{||}^2/V_{T_{e,i}||}^2\right)}{\sqrt{\pi}V_{T_{e,i}||}},$$

$$f_{0\perp}^{e,i}(v_\perp) = \frac{\exp\left(-v_\perp^2/V_{T_{e,i}\perp}^2\right)}{\pi V_{T_{e,i}\perp}^2}.$$

Here,

$$V_{T_{e,i}||} = \left(\frac{2kT_{e,i||}}{m_{e,i}}\right)^{1/2}$$

and

$$V_{T_{e,i}\perp} = \left(\frac{2kT_{e,i\perp}}{m_{e,i}}\right)^{1/2}$$

are the thermal electron and ion velocities in the longitudinal and transverse directions relative to the magnetic field, respectively.

Because of the presence of magnetic mirrors, the particles are separated into trapped and escaping ones. The fragments that correspond to the particles satisfying the escape conditions are removed from the distributions of the particles injected into the trap. Such particles immediately precipitate into the loss cone and are no longer involved in the acceleration. Therefore, in the initial problem of the acceleration of trapped particles, the initial distribution that corresponds to the dimensionless trap length $l = 1$ differs from the injected one: $f(1) \neq f_0$.

For generality, we assume the injected electrons and ions to have different temperatures, with $T_\mathrm{e} \gg T_\mathrm{i}$ for high-temperature current sheets with ion-acoustic turbulence (Somov 1992). Furthermore, the electrons and ions can have different anisotropies. However, their initial densities are equal: $n_{0e} = n_{0i}$.

TRAPPED PARTICLES IN THE CASE $\varphi = 0$

In this simplest case, the cone that corresponds to the trapped particles (both electrons and ions, irrespective of the charge) is

$$0 \le v_{0||} < v_*, \quad 0 \le v_{0\perp} < \infty,$$

where

$$v_* = Rlv_{0\perp}, \quad R = (B_2/B_1 - 1)^{1/2}.$$

However, different injection functions (1) correspond to the electrons and ions. We omit the subscripts e and i thus far. For the total number of particles in the trap and for the distribution function, we have (Bogachev and Somov 1999)

$$N(l) = 4\pi N_0 \int_0^\infty v_{0\perp}dv_{0\perp} \int_0^{v_*} f_0(v_{0||}, v_{0\perp})v_{0\perp}dv_{0||}, \tag{2}$$

where

$$f(v_{||}, v_\perp, l) = \frac{N_0 l}{N(l)}\Theta(Rlv_\perp - v_{||})f_0(lv_{||}, v_\perp) \tag{3}$$

and

$$\Theta(x \ge 0) = 1, \quad \Theta(x < 0) = 0.$$

For the anisotropic Maxwellian distribution (1), we rewrite expression (2) as

$$\frac{N_e(l)}{N_0} = \frac{4}{\sqrt{\pi}} \int_0^\infty y \cdot \exp\left(-y^2\right) J_1(y)dy, \tag{4}$$

where

$$J_1(y) = \int_0^{u_*} \exp\left(-x^2\right) dx$$

and

$$x = v_{0||}/V_{T||}, \quad y = v_{0\perp}/V_{T\perp}, \quad u_* = Rly.$$

We integrate formula (4) by parts as follows:

$$J_1(y) = t, \quad dt = \frac{du_*(y)}{dy}\exp\left(-u_*^2(y)\right)dy,$$

$$dz = y\exp\left(-y^2\right)dy, \quad z = -\frac{1}{2}\exp\left(-y^2\right).$$

Since $J_1(0) = 0$ and

$$\frac{1}{\sqrt{\pi}} \int_0^\infty \frac{\exp\left(-\xi^2\right)d\xi}{\xi} = 1,$$

we obtain

$$\frac{N(l)}{N_0} = ql \tag{5}$$

or

$$\frac{n(l)}{n_0} = q, \tag{6}$$

where

$$q = \frac{\alpha R}{\sqrt{1 + \alpha^2 R^2 l^2}}, \quad \alpha = \sqrt{\frac{T_\perp}{T_{||}}}.$$

The results obtained differ from those in the isotropic case (Bogachev and Somov 1999) by the coefficient α, which describes the degree of anisotropy of the injected particles. For $\alpha_{e,i} > 1$, the particles are trapped more efficiently than they are in the isotropic case, because the transverse velocity component prevails. As a result, $N_e(l)$ and $N_i(l)$ differ in behavior for $\alpha_e \neq \alpha_i$. In the isotropic case, there is no difference. Increasing α causes the trapping coefficient q to increase.

For the electrons and ions, the temperatures and anisotropy parameters can differ: $T_e \neq T_i$ and $\alpha_e \neq \alpha_i$. In this case,

$$q_e = \frac{\alpha_e R}{\sqrt{1+\alpha_e^2 R^2 L^2}}, \quad \alpha_e = \sqrt{\frac{T_{e\perp}}{T_{e||}}}$$

and

$$q_i = \frac{\alpha_i R}{\sqrt{1+\alpha_i^2 R^2 l^2}}, \quad \alpha_i = \sqrt{\frac{T_{i\perp}}{T_{i||}}}.$$

TRAPPED ELECTRONS IN THE CASE $\varphi > 0$

Now, the integration domain is (Kovalev and Somov 2002)

$$0 \leq v_{0||} < v_*, \quad 0 \leq v_{0\perp} < \infty,$$

where

$$v_* = l\left(v_{0\perp}^2 R^2 + v_{\varphi e}^2\right)^{1/2}, \quad v_{\varphi e}^2 = 2e\varphi/m_e.$$

The distribution function is then

$$N_e(l) = 4\pi N_0 \int\limits_0^\infty v_{0\perp} dv_{0\perp} \int\limits_0^{v_*} f_0(v_{0||}, v_{0\perp}) dv_{||}. \quad (7)$$

The latter expression for function (1) can be written as

$$\frac{N_e(l)}{N_0} = \frac{4}{\sqrt{\pi}} \int\limits_0^\infty y \exp\left(-y^2\right) dy J_1(y), \quad (8)$$

where

$$J_1(y) = \int\limits_0^{u_*(y)} \exp\left(-x^2\right) dx$$

and

$$x = v_{0||}/V_{T_{e||}}, \quad y = v_{0\perp}/V_{T_{e\perp}},$$

$$u_* = \alpha_e l (R^2 y^2 + u_{\varphi e}^2)^{1/2}, u_{\varphi e} = v_{\varphi e}/V_{T_{e\perp}}.$$

We integrate (8) by parts:

$$J_1(y) = t, dt = \frac{du_*(y)}{dy} \exp\left(-u_*^2(y)\right) dy,$$

$$dz = y \exp\left(-y^2\right) dy, z = -\frac{1}{2} \exp\left(-y^2\right).$$

As a result, given

$$J_1(0) = \frac{\sqrt{\pi}}{2} \mathrm{erf}(l u_{\varphi e})$$

and

$$\frac{1}{\sqrt{\pi}} \int\limits_0^\infty \frac{\exp(-\xi)}{(\xi+a)^{1/2}} d\xi = e^a [1 - \mathrm{erf}(\sqrt{a})],$$

$$\mathrm{erf}(x) = \frac{2}{\sqrt{\pi}} \int\limits_0^x \exp\left(-\xi^2\right) d\xi, \quad a = \frac{u_\varphi^2}{q^2},$$

$$\xi = y\sqrt{1+R^2 l^2},$$

we obtain

$$\frac{N_e(l)}{N_0} = q_e l \exp\left(\frac{u_\varphi^2}{R^2}\right) \times \left[1 - \mathrm{erf}\left(\alpha_e \frac{u_{\varphi e}}{q_e}\right)\right] + \mathrm{erf}(\alpha_e l u_{\varphi e}). \quad (9)$$

For a weak potential $u_{\varphi e} \ll 1$, using

$$\mathrm{erf}(x) \simeq \frac{2}{\sqrt{\pi}} x + \frac{2}{3\sqrt{\pi}} x^3,$$

we have

$$\frac{N_e(l)}{N_0} \simeq q_e l \left(1 + \frac{u_{\varphi e}^2}{R^2}\right), \quad (10)$$

$$\frac{n_e(l)}{n_0} \simeq q_e \left(1 + \frac{u_{\varphi e}^2}{R^2}\right). \quad (11)$$

We see that the additional effect of electron confinement due to a positive electric potential [the second term in (11)] is enhanced with increasing α_e.

TRAPPED IONS IN THE CASE $\varphi > 0$

The integration domain is (Kovalev and Somov 2002)

$$0 \leq v_{0||} < v_{*i}, \quad v_{\varphi i} < v_{0\perp} < \infty,$$

$$v_{*i} = l(v_{0\perp}^2 R^2 - v_{\varphi i}^2)^{1/2}.$$

Then,

$$N(l) = 4\pi N_0 \int\limits_{v_{\varphi i}}^\infty v_{0\perp} dv_{0\perp} \int\limits_0^{v_{*i}} f_0(v_{0||}, v_{0\perp}) dv_{||}. \quad (12)$$

Here,

$$u_{\varphi i}^2 = \frac{v_{\varphi i}^2}{V_{T_{i\perp}}^2} = \frac{e\varphi}{kT_{i\perp}}.$$

Repeating the same operations as those for electrons, we obtain

$$\frac{N_i(l)}{N_0} = \exp\left(-u_{\varphi i}^2\right) \mathrm{erf}(\alpha_i l r u_{\varphi i}) + q_i l \exp(l^2 u_{\varphi i}^2) \frac{2}{\sqrt{\pi}} \int\limits_b^\infty \xi \frac{\exp\left(-\xi^2\right)}{(\xi^2 - a^2)^{1/2}} d\xi. \quad (13)$$

Here,

$$r = \sqrt{R^2 - 1}, \quad a = \frac{u_{\varphi i}}{q},$$
$$b = u_{\varphi i}\sqrt{1 + R^2 l^2}, \quad \xi = \frac{v_{0\perp}}{V_{T_{i\perp}}}\sqrt{1 + R^2 l^2}.$$

In contrast to the previous case, the integral in (13)

$$J(u) = \int\limits_{b(u)}^{\infty} f(\xi, u) d\xi,$$

where

$$f(\xi, u)\xi \frac{\exp\left(-\xi^2\right)}{(\xi^2 - u^2/q^2)^{1/2}} d\xi$$

cannot be calculated analytically. However, in the case concerned, $u_{\varphi i} \ll 1$, and using the expansion at $u = 0$

$$J(u) \simeq J(0) + \left.\frac{dJ(u)}{du}\right|_{u=0} u,$$

where the derivative is

$$\frac{dJ(u)}{du} = \int\limits_{b(u)}^{\infty} \frac{f(\xi, u)}{du} d\xi - \left.\frac{db(u)}{du} f(\xi, u)\right|_{\xi=b(u)},$$

we obtain

$$\frac{N_i(l)}{N_0} \simeq q_i l - \frac{2}{\sqrt{\pi}} \frac{R^2}{r} \alpha_i l u_{\varphi i} \qquad (14)$$

$$\frac{n_i(l)}{n_0} \simeq q_i - \frac{2}{\sqrt{\pi}} \frac{R^2}{r} \alpha_i u_{\varphi i}. \qquad (15)$$

We see from the latter expression that the effect of ion expulsion from the trap due to a positive electric potential is enhanced with increasing α_i. The competing effects of ion explusion and anisotropy for $\alpha_i > 1$ can offset each other.

DETERMINING THE ELECTRIC POTENTIAL

In the preceding sections, we calculated the particle distributions as a function of the specified potential. Meanwhile, it is of interest to determine the potential itself from the Poisson equation. The latter contains the length parameter, the Debye screening length,

$$D = \sqrt{\frac{kT_e}{4\pi n_e e^2}}.$$

For solar-flare plasma with $T \simeq 10^8$ K and $n_e \simeq 5 \times 10^9$ cm^{-3}, we have $D \simeq 1$ cm. The corresponding Langmuir frequency ω_{P_e} is 4×10^9 rad s^{-1}. However, the plasma becomes anisotropic in a dynamic trap; there is no concept of Debye screening for it. In nonequilibrium plasma, a large-scale charge separation is possible.

An estimate is easiest to obtain by assuming that the plasma is quasineutral: $n_e = n_i$. This assumption is valid when we consider motions whose scale lengths are much larger than the Debye screening length (Gurevich and Pitaevskiĭ 1980). Or, as applied to our problem, the condition under discussion is valid on time scales $t \gg \omega_{P_e}^{-1}$. Equating (11) and (15), for $\alpha_i - \alpha_e \ll \alpha_e$, we then obtain

$$u_{\varphi_e} \simeq \frac{\sqrt{\pi}}{2} \frac{r}{R^2} \sqrt{\frac{T_{i\perp}}{T_{e\perp}}} \frac{1 - \alpha_e/\alpha_i}{\sqrt{1 + \alpha_e^2 R^2 l^2}}. \qquad (16)$$

We see that the positive electric potential increases as the trap is contracting. This suggests the amplification of the initial perturbation and the growth of instability. The initial potential (for $l = 1$) is determined by the mirror ratio and by the difference between the ion and electron anisotropy coefficients.

It follows that in a trap with the mirror ratio $B_1/B_2 = 4$, the electric potential is $\simeq$50 V (10 eV) at the initial time for an isotropic electron distribution ($\alpha_e = 1$) and anisotropic ion distribution ($\alpha_i = 1.1$). The value of $u_\varphi = e\varphi/kT$ is 0.02. For the temperature of the flare plasma $T_e = 10^8$ K, it corresponds to energy $\simeq$200.

CONCLUSIONS

Thus, we have solved the kinetic problem of charged-particle acceleration in a collapsing magnetic trap with a specified electric potential and with converging magnetic mirrors for an anisotropic initial particle distribution. In addition to the conclusions of our previous study (with isotropic injection), we inferred the following.

(1) The particles with an anisotropic distribution injected into a magnetic trap are trapped and, naturally, accelerated more efficiently than they are in the isotropic case if the anisotropy parameter $\alpha = (T_\perp/T_{||})^{1/2} > 1$ (irrespective of the charge).

(2) A specified positive electric potential of the trap plasma relative to the mirrors produces an additional effect of decrease in the fraction of the ions confined in the trap. In this case, the effect is enhanced as α_i increases.

(3) The estimate obtained for a weak electric potential in the approximation of quasineutral plasma indicates that the initial potential determined by the mirror ratio and by the difference between the ion and electron anisotropy coefficients increases with decreasing trap length. This suggests the amplification of the initial perturbation and the growth of instability.

ACKNOWLEDGMENTS

This work was supported by the Russian Foundation for Basic Research (project no. 02-02-16201), the Federal Program "Astronomy" (V.A.K.), and the Russian Foundation for Basic Research (project no. 99-02-16344) (B.V.S.).

REFERENCES

1. S. A. Bogachev and B. V. Somov, Izv. Akad. Nauk, Ser. Fiz. **63**, 1555 (1999).
2. S. A. Bogachev and B. V. Somov, Astron. Zh. **78**, 187 (2001) [Astron. Rep. **45**, 157 (2001)].
3. A. V. Gurevich and L. P. Pitaevskiĭ, in *Reviews of Plasma Physics*, Ed. by M. A. Leontovich (Atomizdat, Moscow, 1980; Consultants Bureau, New York, 1986), Vol. 10.
4. V. A. Kovalev and B. V. Somov, Pis'ma Astron. Zh. **28**, 554 (2002) [Astron. Lett. **28**, 488 (2002)].
5. V. P. Pastukhov, in *Reviews of Plasma Physics*, Ed. by B. B. Kadomtsev (Énergoatomizdat, Moscow, 1984; Consultants Bureau, New York, 1987), Vol. 13.
6. B. V. Somov, *Physical Processes in Solar Flares* (Kluwer, Dordrecht, 1992), p. 64.
7. B. V. Somov, *Cosmic Plasma Physics* (Kluwer, Dordrecht, 2000), p. 652.
8. B. V. Somov and T. Kosugi, Astrophys. J. **485**, 859 (1997).
9. D. S. Spicer and A. G. Emslie, Astrophys. J. **330**, 997 (1998).

Translated by G. Rudnitskii

Astronomy Letters, Vol. 29, No. 2, 2003, pp. 116–125. Translated from Pis'ma v Astronomicheskiĭ Zhurnal, Vol. 29, No. 2, 2003, pp. 137–147.

Parametric Generation of Magnetoacoustic-Gravity Waves in the Solar Atmosphere

M. Yu. Petukhov and Yu. V. Petukhov*

Institute of Applied Physics, Russian Academy of Sciences, ul. Ul'yanova 46, Nizhni Novgorod, 603600 Russia

Received July 9, 2002

Abstract—Based on a plane-parallel isothermal solar model atmosphere permeated by a horizontal magnetic field whose strength is proportional to the square root of the plasma density and in the approximation of a specified field for vertically propagating and nonpropagating magnetoacoustic-gravity waves, we consider the nonlinear interaction between the corresponding disturbances, to within quantities of the second order of smallness. We investigate the efficiency of the nonlinear generation of waves at difference and sum frequencies and of an acoustic flow (wind) as a function of the magnetic-field strength and the excitation frequency of the initial disturbances at the lower atmospheric boundary. © *2003 MAIK "Nauka/Interperiodica".*

Key words: *Sun, atmosphere, waves, parametric generation, magnetic field.*

INTRODUCTION

As previously (Kaplan *et al.* 1977; Dubov 1978; Priest 1982), considerable attention is currently being given to the linear (Dzhalilov and Zhugzhda 1984a, 1984b, 1984c; Cadez *et al.* 1998) and nonlinear (Ostrovskii and Petrukhin 1981; Petukhov and Petukhov 2001, 2002) processes of energy transfer by various types of waves into the upper solar atmosphere. The latter circumstance largely stems from an elucidation of the upper-chromosphere and coronal heating mechanisms that dominate at different heights and of the solar-wind acceleration mechanism (Kaplan *et al.* 1977; Priest 1982). Therefore, the question of whether vertically propagating acoustic-gravity (AG) waves can exist up to coronal heights at relatively low frequencies below the Lamb cutoff frequency ω_L seems of current interest (Kaplan *et al.* 1977; Dubov 1978; Priest 1982; M. Petukhov and Yu. Petukhov 2001, 2002).

As we showed previously (M. Petukhov and Yu. Petukhov 2001), such waves can exist in an isothermal atmosphere without a magnetic field or, more specifically, during the nonlinear interaction between the initially propagating AG waves at radiation frequencies $\omega_1 > \omega_L$ and $\omega_2 > \omega_L$ that are generated by nonpropagating oscillations and propagating waves at the difference frequency $\Omega = \omega_2 - \omega_1$ in the corresponding range $\Omega < \omega_L$ forbidden for the propagation of AG waves during their linear generation (Kaplan *et al.* 1977; Dubov 1978; Priest 1982).

In actual conditions, the solar atmosphere is permeated by a magnetic field (see Kaplan *et al.* 1977; Dubov 1978; Priest 1982) whose regular vertical component (for a plane-parallel model atmosphere) plays a significant role in the energy transfer by various types of waves almost over the entire height range (Ulrich 1996). As a result, vertically propagating Alfvén waves (Ulrich 1996) can clearly show up in certain frequency and height ranges (see Kaplan *et al.* 1977; M. Petukhov and Yu. Petukhov 2002). As was shown previously (M. Petukhov and Yu. Petukhov 2002), during the nonlinear interaction, these waves will generate propagating AG waves at a difference frequency $\Omega < \omega_L$, as in M. Petukhov and Yu. Petukhov (2001).

In contrast to the vertical component (see Ulrich 1996), the regular horizontal magnetic field in the solar atmosphere can affect the corresponding wave processes only at chromospheric heights (Campbell and Roberts 1989; Evans and Roberts 1990). Nevertheless, studying this effect on the nonlinear interaction and, in particular, on the generation of vertically propagating magnetoacoustic-gravity (MAG) waves at a difference frequency $\Omega < \omega_L$ are of considerable interest, because the horizontal magnetic field can fundamentally change the pattern of the linear vertical propagation of MAG waves (Nye and Thomas 1976a, 1976b; An *et al.* 1989; Musielak and Stark 1993).

That is why our goal here is to study the nonlinear interaction between vertically propagating MAG waves in an isothermal solar atmosphere permeated by a horizontal magnetic field. Since the mathematical description of vertically propagating MAG waves

*E-mail: petukhov@hydro.appl.sci-nnov.ru

1063-7737/03/2902-0116$24.00

in a uniform horizontal magnetic field is less clear (see Nye and Thomas 1976a, 1976b; An *et al.* 1989; Musielak and Stark 1993) than that of Alfvén waves in a uniform vertical magnetic field (M. Petukhov and Yu. Petukhov 2002), we use a model dependence of its strength proportional to the square root of the ambient density (Miles and Roberts 1992; Jain and Roberts 1994). Naturally, in this solar model atmosphere commonly used in the corresponding calculations, the numerical values of its characteristic parameters should be chosen to satisfy the condition for its stable static equilibrium (Thomas and Nye 1975).

FORMULATION OF THE PROBLEM AND BASIC EQUATIONS

Let us consider the vertical propagation of plane MAG waves in a plane-parallel isothermal atmosphere, $z \geqslant 0$, permeated by a horizontal magnetic field. Assume that the z axis is directed vertically upward against the action of gravity whose free-fall acceleration is constant and equal to g, the magnetic induction vector $\mathbf{B}_0 = (B_0, 0, 0)$ is directed horizontally along the x axis, and its corresponding component falls off with increasing height as the square root of the decreasing ambient density. The equilibrium density ρ_0, pressure p_0, and magnetic field B_0 then depend on height z as follows:

$$\begin{aligned} \rho_0 &= \rho_{00}\exp(-z/H), \\ p_0 &= \frac{\rho_{00}c_0^2}{\gamma}\exp(-z/H), \\ B_0 &= B_{00}\exp(-z/2H). \end{aligned} \tag{1}$$

Here, c_0 is the constant adiabatic speed of sound, γ is the adiabatic index, H is the scale height:

$$c_0^2 = \gamma p_0/\rho_0\,, \quad H = \frac{1}{g}\left(\frac{c_0^2}{\gamma} + \frac{c_\mathrm{A}^2}{2}\right)\,, \tag{2}$$

ρ_{00} and B_{00} are the density and the magnetic induction at the lower atmospheric boundary ($z = 0$), respectively; c_A is the Alfvén velocity, which, as follows from (1), is constant:

$$c_\mathrm{A} = B_0/\sqrt{\mu_0\rho_0} = B_{00}/\sqrt{\mu_0\rho_{00}}\,, \tag{3}$$

μ_0 is the magnetic constant. We also assume that the lower atmospheric boundary executes steady-state (in time t) vertical oscillations at frequencies ω_1 and ω_2 with the respective amplitudes A_1 and A_2 of the vertical oscillation velocity $v_z = v$:

$$\begin{aligned} v|_{z=0} &= A_1\cos\omega_1 t + A_2\cos(\omega_2 t + \varphi)\,, \\ &-\infty < t < +\infty, \end{aligned} \tag{4}$$

where $A_1 \times A_2 > 0$ and φ is a certain phase.

The frequency range $0 < \omega < \omega_\mathrm{cf}$ forbidden for the linear propagation of MAG waves is known (Dzhalilov and Zhugzhda 1984a) to exist in such an atmosphere:

$$\omega_\mathrm{cf} = \frac{(c_0^2 + c_A^2)^{1/2}}{2H} = \omega_\mathrm{L}\beta\frac{\sqrt{1+\beta^2}}{\frac{\gamma}{2}+\beta^2}, \tag{5}$$

where ω_cf is the characteristic cutoff frequency of the MAG waves ($\omega_\mathrm{cf} < \omega_\mathrm{L}$), $\omega_\mathrm{L} = \gamma g/2c_0$ is the Lamb cutoff frequency of the AG waves in the absence of a magnetic field ($B_0 = 0$), and $\beta = c_0/c_\mathrm{A}$ is a parameter that characterizes the relative dominance of the acoustic or magnetic effects during the propagation of the MAG waves.

The range of difference frequencies $\Omega = \omega_2 - \omega_1$ forbidden for the linear propagation of MAG waves (Kaplan *et al.* 1977; Dubov 1978; Priest 1982) is of greatest interest in studying their parametric generation:

$$0 < \Omega < \omega_\mathrm{cf}. \tag{6}$$

Therefore, below, we mainly analyze the fundamental pattern of the parametric generation of MAG waves for the specified conditions (1)–(4) and (6), under which the primary waves at frequencies $\omega_1 > \omega_\mathrm{cf}$ and $\omega_2 > \omega_\mathrm{cf}$ are propagating ones (M. Petukhov and Yu. Petukhov 2001).

For an approximate analytical description of the processes concerned, the following nonlinear equation can be derived from the equations for the conservation of momentum, mass, and energy and from the induction equation (see Priest 1982) for an arbitrary dependence $B_0(z)$, to within terms of the second order of smallness in perturbations of the corresponding hydrodynamic (ρ'/ρ_0, p'/p_0, v/c_0) and magnetic (B'/B_0) quantities:

$$\widehat{L}v = G, \tag{7}$$

in which $\widehat{L}$ is a linear operator:

$$\widehat{L} = \frac{\partial^2}{\partial t^2} - \left(c_0^2 + c_\mathrm{A}^2\right)\frac{\partial^2}{\partial z^2} + \frac{c_0^2 + c_\mathrm{A}^2}{H}\frac{\partial}{\partial z}\,, \tag{8}$$

and the function G combines the nonlinear terms:

$$\begin{aligned} G = &\frac{\gamma}{\rho_0}\frac{\partial}{\partial z}\left(p'\frac{\partial v}{\partial z}\right) - \frac{\rho'}{\rho_0}\frac{\partial^2 v}{\partial t^2} - \frac{\partial v}{\partial t}\frac{\partial v}{\partial z} \\ &- 2v\frac{\partial^2 v}{\partial t\partial z} + \frac{B_0 B'}{\mu_0\rho_0}\frac{\partial^2 v}{\partial z^2} + \frac{B_0}{\mu_0\rho_0}\frac{\partial B'}{\partial z}\frac{\partial v}{\partial z} \\ &+ \frac{v}{\mu_0\rho_0}\left(\frac{\partial B_0}{\partial z}\frac{\partial B'}{\partial z} - \frac{B'}{2H}\frac{\partial^2 B_0}{\partial z^2}\right) - \frac{1}{2\mu_0\rho_0}\frac{\partial^2 B'^2}{\partial t\partial z}\,. \end{aligned} \tag{9}$$

Here, ρ', p', B' are the density, pressure, and magnetic-induction perturbations, respectively. Note that the density, pressure, and magnetic-induction perturbations in (9) are linearly related to the oscillation

velocity (see M. Petukhov and Yu. Petukhov 2001):

$$\frac{\partial \rho'}{\partial t} = \rho_0 \left(\frac{1}{H} - \frac{\partial}{\partial z}\right) v,$$
$$\frac{\partial p'}{\partial t} = \rho_0 c_0^2 \left(\frac{1}{\gamma H} - \frac{\partial}{\partial z}\right) v, \qquad (10)$$
$$\frac{\partial B'}{\partial t} = B_0 \left(\frac{1}{2H} - \frac{\partial}{\partial z}\right) v.$$

THE NONLINEAR GENERATION OF MAG DISTURBANCES AT A DIFFERENCE FREQUENCY BY PROPAGATING WAVES

To solve the nonlinear equation (7), we use the method of successive approximations to within quantities of the second order of smallness for this equation:

$$v = v^{(1)} + v^{(2)}, \quad \rho' = \rho^{(1)} + \rho^{(2)}, \qquad (11)$$
$$p' = p^{(1)} + p^{(2)}, \quad B' = B^{(1)} + B^{(2)}.$$

Here, $v^{(1)}$, $\rho^{(1)}$, $p^{(1)}$, $B^{(1)}$ and $v^{(2)}$, $\rho^{(2)}$, $p^{(2)}$, $B^{(2)}$ are the quantities of the first and second orders of smallness, respectively. In the linear approximation, we derive a standard linear equation (see Priest 1982) from (7) and (11). Its solutions for upward-propagating and nonpropagating waves with frequency ω and initial (at the $z = 0$ surface) amplitude A are

$$v^{(1)} = A \begin{cases} \exp\left[\eta z + i\left(\omega t - \sqrt{\dfrac{\omega^2}{\omega_{\rm cf}^2} - 1}\,\eta z\right)\right], \\ \omega > \omega_{\rm cf} \\ \exp\left[i\omega t + \left(1 - \sqrt{1 - \dfrac{\omega^2}{\omega_{\rm cf}^2}}\right)\eta z\right], \\ \omega < \omega_{\rm cf}, \end{cases} \qquad (12)$$

where $\eta = 1/2H$. Note that by solution (12) we mean its real part $v_{\rm R}^{(1)} = {\rm Re}\left\{v^{(1)}\right\}$. Therefore, taking into account the boundary condition (4) and using (10) and (12), we obtain the following solutions for the corresponding quantities:

$$\mathrm{v}_{\rm R}^{(1)} = e^{\eta z} \sum_{j=1}^{2} A_j \cos\left(\omega_j t - \alpha_j z + \varphi_j\right),$$

$$\rho_{\rm R}^{(1)} = \frac{\rho_{00}}{c_{\rm F}} e^{-\eta z}$$
$$\times \sum_{j=1}^{2} A_j \left\{ \sqrt{1 - \frac{\omega_{\rm cf}^2}{\omega_j^2}} \cos(\omega_j t - \alpha_j z + \varphi_j) \right.$$
$$\left. + \frac{\omega_{\rm cf}}{\omega_j} \sin\left(\omega_j t - \alpha_j z + \varphi_j\right) \right\},$$

$$p_{\rm R}^{(1)} = \frac{\rho_{00} c_0^2}{c_{\rm F}} e^{-\eta z} \qquad (13)$$
$$\times \sum_{j=1}^{2} A_j \left\{ \sqrt{1 - \frac{\omega_{\rm cf}^2}{\omega_j^2}} \cos\left(\omega_j t - \alpha_j z + \varphi_j\right) \right.$$
$$\left. + \frac{2-\gamma}{\gamma} \frac{\omega_{\rm cf}}{\omega_j} \sin\left(\omega_j t - \alpha_j z + \varphi_j\right) \right\},$$

$$B_{\rm R}^{(1)} = \frac{B_{00}}{c_{\rm F}} \sum_{j=1}^{2} A_j \sqrt{1 - \frac{\omega_{\rm cf}^2}{\omega_j^2}} \cos\left(\omega_j t - \alpha_j z + \varphi_j\right),$$

where

$$\rho_{\rm R}^{(1)} = {\rm Re}\left\{\rho^{(1)}\right\}, \quad p_{\rm R}^{(1)} = {\rm Re}\left\{p^{(1)}\right\}, \qquad (14)$$
$$B_{\rm R}^{(1)} = {\rm Re}\left\{B^{(1)}\right\},$$
$$\alpha_j = \eta \sqrt{\frac{\omega_j^2}{\omega_{\rm cf}^2} - 1}, \quad c_{\rm F} = \sqrt{c_0^2 + c_{\rm A}^2},$$
$$\varphi_1 = 0,\ \varphi_2 = \varphi.$$

For the quantity of the second order of smallness $v^{(2)}$, we derive from (7) and (11)

$$\widehat{L} v^{(2)} = G^{(2)}, \qquad (15)$$

$$G^{(2)} = \frac{\gamma}{\rho_0} \frac{\partial}{\partial z}\left(p_{\rm R}^{(1)} \frac{\partial v_{\rm R}^{(1)}}{\partial z}\right) - \frac{\rho_{\rm R}^{(1)}}{\rho_0} \frac{\partial^2 v_{\rm R}^{(1)}}{\partial t^2} \qquad (16)$$
$$- \frac{\partial v_{\rm R}^{(1)}}{\partial t} \frac{\partial v_{\rm R}^{(1)}}{\partial z} - 2 v_{\rm R}^{(1)} \frac{\partial^2 v_{\rm R}^{(1)}}{\partial t \partial z} + \frac{B_0 B_{\rm R}^{(1)}}{\mu_0 \rho_0} \frac{\partial^2 v_{\rm R}^{(1)}}{\partial z^2}$$
$$+ \frac{B_0}{\mu_0 \rho_0} \frac{\partial B_{\rm R}^{(1)}}{\partial z} \frac{\partial v_{\rm R}^{(1)}}{\partial z} + \frac{v_{\rm R}^{(1)} B_0}{2\mu_0 H \rho_0} \left(\frac{\partial B_{\rm R}^{(1)}}{\partial z} - \frac{B_{\rm R}^{(1)}}{2H}\right)$$
$$- \frac{1}{2\mu_0 \rho_0} \frac{\partial^2 \left(B_R^{(1)}\right)^2}{\partial t \partial z},$$

where the quantities $v_{\rm R}^{(1)}$, $\rho_{\rm R}^{(1)}$, $p_{\rm R}^{(1)}$, and $B_{\rm R}^{(1)}$ are defined by expressions (13). Separating out the terms in $G^{(2)}$ (16) responsible for the wave generation at the difference frequency Ω, we transform Eq. (15) to the following approximate form:

$$\widehat{L} v^{(2)} \simeq {\rm Re}\left\{D \exp\left[2\eta z + i\left(\Omega t - \xi z + \varphi\right)\right]\right\}, \qquad (17)$$

in which, for convenience, we use the notation

$$D = D_1 - i D_2,$$

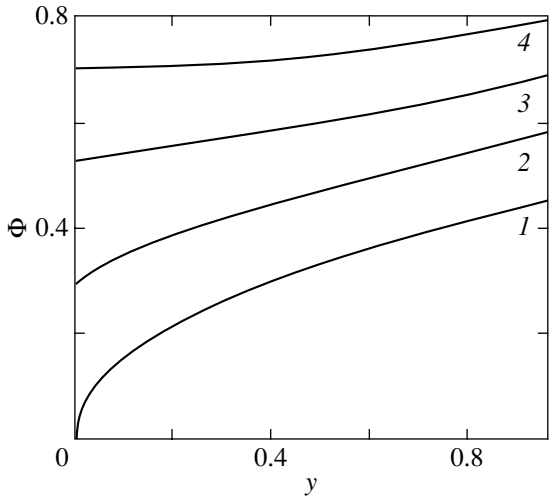

Fig. 1. Normalized quantity Φ versus dimensionless difference frequency $y = \Omega/\omega_{cf}$ for $\beta = 1$, $\varphi = 0$: $\omega = \omega_{cf}$ (*1*), $\omega = 1.1\omega_{cf}$ (*2*), $\omega = 1.5\omega_{cf}$ (*3*), and $\omega = 10\omega_{cf}$ (*4*).

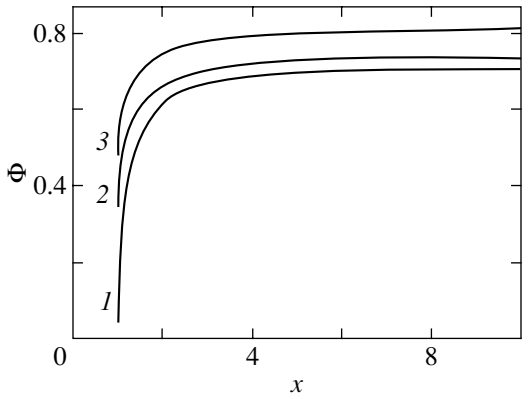

Fig. 2. Normalized quantity Φ versus dimensionless excitation frequency $x = \omega_1/\omega_{cf}$ for $\beta = 1$, $\varphi = 0$: $\Omega = 0.001\omega_{cf}$ (*1*), $\Omega = 0.5\omega_{cf}$ (*2*), and $\Omega = \omega_{cf}$ (*3*).

$$D_1 = \frac{A_1 A_2 \Omega}{2\omega_2\omega_1}\left\{\xi c_0^2\left[(2-\gamma)\eta^2 - \gamma\alpha_1\alpha_2\right] - \alpha_2\omega_1(\omega_1+2\omega_2) + \alpha_1\omega_2(\omega_2+2\omega_1) - 3c_A^2\alpha_1\alpha_2\xi\right\}, \quad (18)$$

$$D_2 = \frac{A_1 A_2 \eta}{2\omega_2\omega_1}\left\{\xi c_0^2\left[\gamma(\alpha_1\omega_2+\alpha_2\omega_1) + (2-\gamma)(\alpha_2\omega_2+\alpha_1\omega_1)\right] - \Omega^3 + 2c_A^2\left[\alpha_1\alpha_2\Omega + \left(\alpha_2^2\omega_1 - \alpha_1^2\omega_2\right)\right]\right\},$$

$$\xi = \alpha_2 - \alpha_1.$$

In solving Eq. (17), we use the natural boundary condition

$$v^{(2)}|_{z=0} = 0, \quad (19)$$

which corresponds to the absence of difference-frequency waves at the $z = 0$ boundary surface, and choose only those solutions which would definitely correspond to the waves traveling along the z axis at $\Omega > \omega_{cf}$. Representing the general solution of Eq. (17) as a sum of the solutions of the corresponding inhomogeneous and homogeneous equations, we then obtain

$$v_R^{(2)} = \mathrm{Re}\left\{v^{(2)}\right\}, \quad (20)$$

$$v^{(2)} = T\left\{e^{\eta z + i(\Omega t+\varphi)}\left[e^{(\eta - i\xi)z} - e^{-\sqrt{1-\Omega^2/\omega_{cf}^2}\eta z}\right]\right\}, \quad (21)$$

$$T = \frac{D}{c_F^2\left[\xi^2 + 2i\eta\xi - \Omega^2/c_F^2\right]}. \quad (22)$$

The first term in (21), which is the solution of the inhomogeneous equation (17), corresponds to upward-propagating MAG waves at frequencies $\Omega < \omega_{cf}$. Their oscillation velocity amplitude increases in inverse proportion to the decreasing ambient density, while for linear MAG waves at frequencies ω_1 and ω_2, this quantity increases with height in inverse proportion to the square root of the ambient density. In contrast, the second term in (21), which is the solution of the corresponding homogeneous equation (17), corresponds to nonpropagating (inhomogeneous) MAG waves at frequencies $\Omega < \omega_{cf}$ whose oscillation velocity amplitude increases with height much more slowly than that for propagating waves.

Note that the complex quantity D in (18) can clearly be represented as a finite sum of exponential functions with different complex exponents:

$$D = A_1 A_2 \sum_{n=1}^{N} \exp(a_n + ib_n), \quad (23)$$

where a_n and b_n are the real quantities whose expressions are simple only in the absence of a magnetic field ($B_0 = 0$, $N = 8$; see M. Petukhov and Yu. Petukhov 2001). Therefore, these expressions are not given here, because they are cumbersome.

It follows from (22) and (23) that each term in (21) describes the corresponding group of a certain number of waves. More specifically, the first and second groups consist of propagating and nonpropagating MAG waves, respectively. The amplitudes and phases of the waves in each group are different, while their phase velocities are equal. The latter implies that a complex interference structures of the MAG wave field is formed during the parametric generation of MAG waves in an isothermal atmosphere at a difference frequency $\Omega < \omega_{cf}$.

The following conclusions can be drawn from the numerically computed Ω, ω_1, and $\sigma = 1/\beta$ dependences of the normalized quantity $\Phi = |c_0 T/A_1 A_2|$

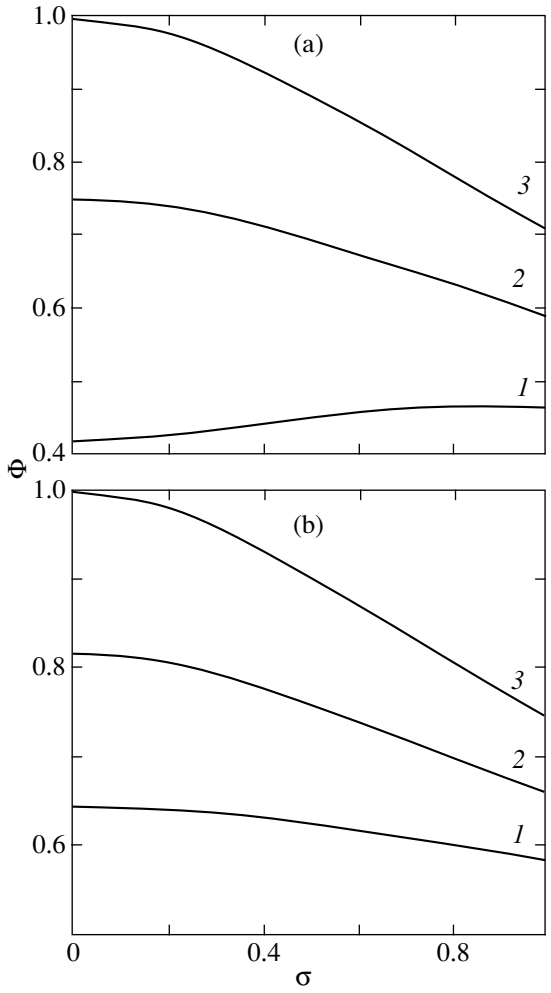

Fig. 3. Normalized quantity Φ versus $\sigma = 1 / \beta$ for $\varphi = 0$ и $\Omega = 0$ (a), $\Omega = 0.5\omega_L$ (b): $\omega = 1.1\omega_L$ (*1*), $\omega = 1.5\omega_L$ (*2*), and $\omega = 10\omega_L$ (*3*).

at $\varphi = 0$ (see Figs. 1–3), which characterizes the oscillation velocity amplitude at a difference frequency in each of the two groups of waves at $z = 0$.

First, as would be expected (see M. Petukhov and Yu. Petukhov 2001), the amplitude of the generated MAG waves increases with difference frequency (see Fig. 1) in such a way that for $\omega_1 \approx 4\omega_{cf}$ the quantity Φ takes on almost equal values over the entire frequency range $0 < \Omega < \omega_{cf}$ of interest (see Fig. 2).

Second, as the Alfvén velocity increases, the amplitude of the MAG waves generated at difference frequencies decreases for initial radiation frequencies ω_1 that exceed a certain value ω_* and increases (or has a maximum) for $\omega_{cf} < \omega_1 < \omega_*$. The frequency ω_* itself decreases with increasing difference frequency Ω. It should be noted, however, that at radiation frequencies $\omega_{cf} < \omega_1 < \omega_*$, the increase of Φ with Alfvén velocity (see Fig. 3) causes the amplitudes of the MAG waves to increase only at z smaller than a certain height z_c, because the exponential factor $e^{\eta z}$ in (21), which decreases with increasing Alfvén velocity (the scale height H increases), causes the amplitude to fall at $z > z_c$.

Third, the fact that at $\Omega = 0$ the quantity Φ is nonzero (see Figs. 1–3), as is the quantity

$$v_0 = \lim_{\Omega \to 0} \left(v_R^{(2)} \right) \neq 0 \qquad (24)$$

at $z > 0$ and $\varphi = 0$ [see (21)], implies that, as we showed previously (M. Petukhov and Yu. Petukhov 2001), the nonlinear interaction between MAG waves in the case under consideration gives rise to a flow—an acoustic wind.

Let us analyze in more detail the dependence of the acoustic wind velocity on characteristic quantities. To this end, we derive the following expression from (24) using (21):

$$v_0 = -\frac{A_1 A_2 \cos\varphi}{2H\omega_1} \sqrt{\frac{\omega_1^2}{\omega_{cf}^2} - 1} \left(e^{2\eta z} - 1 \right). \qquad (25)$$

This expression describes only the part of the acoustic wind that results from the interaction between two waves with amplitudes A_1 and A_2. In deriving a complete expression for the acoustic flow V, we must take into account the fact that each of these waves at a zero difference frequency also produces an acoustic flow with velocities v_1 and v_2, respectively. Using an asymptotic procedure ($\Omega = \omega_1 - \omega_1 \to 0$, $\Omega = \omega_2 - \omega_2 \to 0$) similar to that described when deriving relation (25), we obtain the following expression for the terms additional to v_0:

$$v_j = -\frac{A_j^2 \cos^2 \varphi_j}{4\omega_j H} \sqrt{\frac{\omega_j^2}{\omega_{cf}^2} - 1} \left(e^{2\eta z} - 1 \right), \qquad (26)$$

where $j = 1, 2$ and $\varphi_1 = 0$, $\varphi_2 = \varphi$. Since we used the passage to the limit $\omega_2 \to \omega_1$ when deriving relation (25), we obtain the sought-for expression for the acoustic flow velocity from (25) and (26):

$$V = \sum_{j=0}^{2} v_j \qquad (27)$$

$$= -\frac{(A_1 + A_2 \cos\varphi)^2}{4H\omega_1} \sqrt{\frac{\omega_1^2}{\omega_{cf}^2} - 1} \left(e^{2\eta z} - 1 \right).$$

It follows from relation (27) that the acoustic flow velocity significantly depends on the initial phase difference between the initial oscillations [see (4)], which was disregarded previously (M. Petukhov and Yu. Petukhov 2001). There is no acoustic flow at $\omega_1 \leqslant \omega_{cf}$, while, at relatively high frequencies $\omega_1 \gg \omega_{cf}$, its velocity is virtually independent of the initial radiation frequency.

Furthermore, as follows from our analysis of the behavior of $\Phi(\sigma)$ (see Fig. 3a) and expression (27), the dependence of the acoustic flow velocity on magnetic-field strength [i.e., $V(\sigma)$] can have a maximum only at radiation frequencies close to the Lamb frequency ω_L. The latter can be shown analytically by using the approximate dependences that follow from (27) at $\sigma \ll 2\sqrt{\gamma-1}/\gamma$ and $\omega_1 = \omega_L$, $\omega_1 \gg \omega_L$:

$$V \approx -\frac{(A_1 + A_2\cos\varphi)^2\sqrt{\gamma-1}}{4\omega_L H_L} \times \begin{cases} \dfrac{z}{H_L}\sigma\left(1-a\sigma^2\right), & z/H_L \ll 1 \\ e^{\frac{z}{H_L}}\sigma e^{-\frac{\gamma z}{2H_L}\sigma^2}, & z/H_L \gg 1, \end{cases} \quad \omega_1 = \omega_L, \tag{28}$$

$$V \approx -\frac{(A_1 + A_2\cos\varphi)^2}{4\omega_L H_L} \times \begin{cases} \dfrac{z}{H_L}\left(1-\dfrac{\gamma+2}{\gamma}\sigma^2\right), & z/H_L \ll 1 \\ e^{\frac{z}{H_L}}\left(1-\sigma^2\right)e^{-\frac{\gamma z}{2H_L}\sigma^2}, & z/H_L \gg 1, \end{cases} \quad \omega_1 \gg \omega_L,$$

It clearly follows from (28) that only at $\omega_1 \to \omega_L$ does $V(\sigma)$ reach its maximum for certain $\sigma = \sigma_m$:

$$\sigma_m \simeq \begin{cases} 1/\sqrt{3a}\,, & z/H_L \ll 1 \\ \sqrt{H_L/\gamma z}, & z/H_L \gg 1\,, \end{cases} \tag{29}$$

where

$$H_L = c_0/2\omega_L,\ a = \frac{7\gamma^2 - 4\gamma - 4}{8(\gamma-1)}. \tag{30}$$

As we see from (29), the magnetic-field strength for which the flow velocity is at a maximum is constant at relatively small heights and decreases with increasing z at relatively large heights.

We see from the numerically computed dependences $\sigma_m(z)$ shown in Fig. 4 that, as follows from the approximate analytical expressions (28) and (29), the position of the σ_m maximum in $V(\sigma)$ at relatively low radiation frequencies $\omega_{cf} < \omega_1 \leqslant \omega_L$ asymptotically approaches zero as $z \to \infty$, while, at relatively high frequencies $\omega_1 \gg \omega_L$, the maximum is always located at $\sigma_m = 0$. However, it turned out that, for radiation frequencies slightly exceeding the Lamb frequency ω_L, the maximum in $V(\sigma)$ at $\sigma_m = 0$ exists only at certain heights; i.e., σ_m decreases to zero at a finite height z, which, in turn, decreases with increasing ω_1.

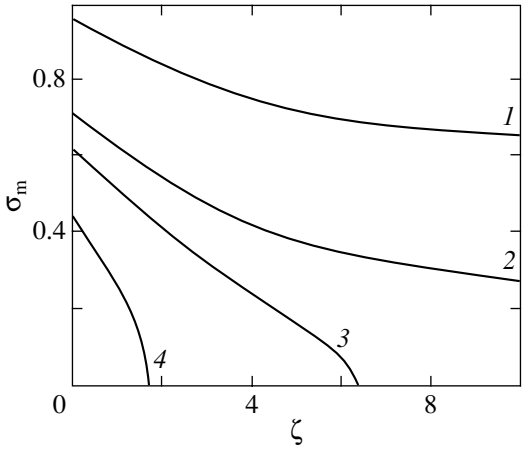

Fig. 4. The position of the σ_m maximum versus dimensionless height $\zeta = z/H_L$ for various radiation frequencies $\omega = 0.94\omega_L$ (*1*), $\omega = \omega_L$ (*2*), $\omega = 1.02\omega_L$ (*3*), and $\omega = 1.05\omega_L$ (*4*).

THE NONLINEAR GENERATION OF MAG WAVES AT THE SECOND HARMONIC BY NONPROPAGATING DISTURBANCES

Consider the nonlinear generation of MAG waves at the second harmonic by disturbances from the forbidden frequency range (see M. Petukhov and Yu. Petukhov 2001). The latter is of considerable interest in studying the energy transfer in the solar atmosphere by the propagating waves generated by nonpropagating disturbances. To this end, we assume that the following relations hold:

$$A_1 = A_2 = A/2, \qquad \omega_1 = \omega_2 = \omega < \omega_{cf}, \quad 2\omega > \omega_{cf}\,. \tag{31}$$

We then obtain the following expressions for the hydrodynamic and magnetic quantities for nonpropagating disturbances from (10) and (12):

$$v_R^{(1)} = Ae^{(\eta-\chi)z}\cos\omega t, \tag{32}$$

$$\rho_R^{(1)} = \frac{\rho_{00}A(\eta-\chi)}{\omega}e^{-(\eta+\chi)z}\sin\omega t,$$

$$p_R^{(1)} = \frac{\rho_{00}Ac_0^2}{2\omega H} \times \left(\frac{2-\gamma}{\gamma} + \sqrt{1-\frac{\omega^2}{\omega_{cf}^2}}\right)e^{-(\eta+\chi)z}\sin\omega t,$$

$$B_R^{(1)} = \frac{AB_{00}\chi}{\omega}e^{-\chi z}\sin\omega t,$$

where

$$\chi = \eta\sqrt{1-\frac{\omega^2}{\omega_{cf}^2}}\,. \tag{33}$$

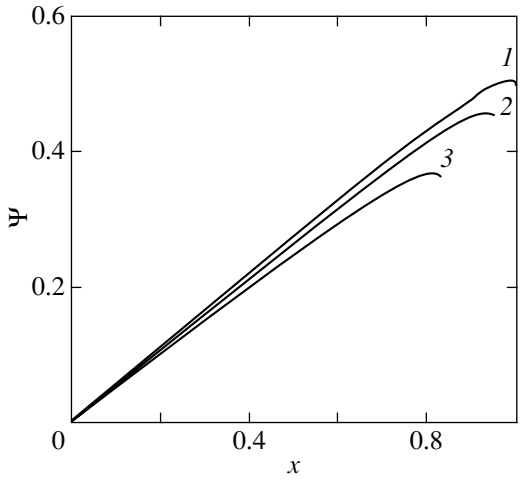

Fig. 5. Normalized quantity $\Psi = c_0 |T_{11}| / A^2$ versus dimensionless excitation frequency $x = \omega/\omega_L$ for $\sigma = 0$ (*1*), $\sigma = 0.5$ (*2*), and $\sigma = 1$ (*3*).

Separating out the term in (16) responsible for the generation of the second harmonic using (32), we then transform Eq. (15) to the approximate form

$$\widehat{L}v^{(2)} \simeq A_{11} e^{2(\eta-\chi)z} \sin 2\omega t, \qquad (34)$$

where

$$A_{11} = A^2 \left\{ -\frac{\gamma c_0^2 \eta\chi}{\omega}(\eta-\chi)\left(\frac{2-\gamma}{\gamma} + \sqrt{1-\frac{\omega^2}{\omega_{cf}^2}}\right) + \omega(2\eta-\chi) - \frac{2c_A^2(\eta-\chi)\chi^2}{\omega}\right\}.$$

The solution of Eq. (34) that satisfies the boundary condition (19) is a sum of the corresponding solutions of the homogeneous and inhomogeneous equations:

$$v_R^{(2)} = T_{11}\left\{U - e^{2(\eta-\chi)z}\sin 2\omega t\right\}, \qquad (35)$$

where

$$T_{11} = \frac{A_{11}}{4\omega_{cf}^2\left(1-\sqrt{1-\omega^2/\omega_{cf}^2}\right)},$$

$$U = \begin{cases} \exp\left[\left(1-\sqrt{1-\dfrac{4\omega^2}{\omega_{cf}^2}}\right)\eta z\right]\sin(2\omega t), \\ 2\omega < \omega_{cf} \\ \exp(\eta z)\sin\left[2\omega t - \left(\sqrt{\dfrac{4\omega^2}{\omega_{cf}^2}-1}\right)\eta z\right], \\ 2\omega > \omega_{cf}. \end{cases} \qquad (36)$$

We see from (35) and (36) that, as in the absence of a magnetic field (see M. Petukhov and Yu. Petukhov 2001), disturbances from the forbidden frequency range can excite propagating MAG waves at the second harmonic at $\omega > \omega_{cf}/2$. The oscillation velocity amplitude of the latter increases with height in inverse proportion to the square root of the decreasing ambient density, i.e., as in the case of linear MAG waves at the corresponding frequencies $\omega > \omega_{cf}$. The oscillation velocity amplitude for nonpropagating waves at the second harmonic for frequencies $\sqrt{3}\omega_{cf} < 2\omega \leqslant 2\omega_{cf}$ increases with height faster than that for propagating MAG waves. Thus, only at certain oscillation frequencies $\dfrac{\sqrt{3}}{2}\omega_{cf} < \omega \leqslant \omega_{cf}$ of the boundary ($z = 0$) surface do nonpropagating disturbances mainly contribute to the MAG wave field at the second harmonic and at large heights $z > H$.

The following conclusions can be drawn from the dependence of the normalized quantity $\Psi = c_0 |T_{11}| / A^2$, which characterizes the amplitude of the MAG waves at the second harmonic, on the initial excitation frequency ω.

First, the amplitude of the MAG waves at the second harmonic increases with radiation frequency almost over the entire frequency range $0 < \omega < \omega_{cf}$ under consideration, except a comparatively narrow frequency interval $\omega_m \leqslant \omega \leqslant \omega_{cf}$ $(1 - \omega_m/\omega_{cf} \ll 1)$, in which it decreases; for $\omega = \omega_m$, the amplitude reaches its maximum.

Second, the decrease in Ψ (see Fig. 5) and in the amplitude exponential factors in solution (35) with increasing Alfvén velocity c_A over the entire range of radiation frequencies implies a similar decrease in the amplitude of the MAG waves at the second harmonic over the entire height range $z > 0$.

PECULIARITIES OF THE NONLINEAR INTERACTION BETWEEN PROPAGATING AND NONPROPAGATING MAG WAVES

Given the importance of the nonlinear energy transformation of oscillations at frequencies $\omega < \omega_{cf}$, let us now consider the parametric generation of MAG waves at a difference frequency that result from the nonlinear interaction between primary nonpropagating waves at frequency ω_1 $(\omega_1 < \omega_{cf})$ and propagating waves at frequency $\omega_2 (\omega_2 > \omega_{cf})$. In this case, the solution of the linear equation (7) with the boundary condition (4) is

$$v_R^{(1)} = A_1 e^{(\eta-\chi_1)z}\cos\omega_1 t + A_2 e^{\eta z}\cos(\omega_2 t - \alpha_2 z + \varphi), \qquad (37)$$

where

$$\chi_1 = \eta\sqrt{1-\omega_1^2/\omega_{cf}^2}.$$

By analogy with the aforesaid, we obtain an equation for the oscillation velocity $v^{(2)}$ at a difference frequency from (10), (16), and (37):

$$\widehat{L}v^{(2)} \simeq \mathrm{Re}\left\{R\exp\left[(2\eta-\chi_1)z+i\left(\Omega t-\alpha_2 z+\varphi\right)\right]\right\}, \tag{38}$$

where

$$R = R_1 - iR_2, \tag{39}$$

$$R_1 = \frac{c_0^2\alpha_2(\eta-\chi_1)\Omega}{2\omega_1\omega_2}\left[(2-\gamma)\eta+\gamma\chi_1\right] + \frac{\alpha_2}{2\omega_2}\left(\omega_1^2+\omega_1\omega_2-2\omega_2^2\right) + \frac{c_\mathrm{A}^2\alpha_2\chi_1(\eta-\chi_1)\Omega}{\omega_1\omega_2},$$

$$R_2 = \frac{c_0^2}{2}\left[\frac{\alpha_2^2+\chi_1\eta}{\omega_1}\left[(2-\gamma)\eta+\gamma\chi_1\right] + \frac{\eta-\chi_1}{\omega_2}\left[\gamma\alpha_2^2-(2-\gamma)\eta\chi_1\right]\right] + c_\mathrm{A}^2\left[\frac{\chi_1}{\omega_1}\left(\alpha_2^2+\eta\chi_1\right)+\frac{\alpha_2^2}{\omega_2}(\eta-\chi_1)\right] + \frac{1}{2}\left[\frac{\omega_1^2}{\omega_2}\eta-\frac{\omega_2^2}{\omega_1}(\eta+\chi_1) + \omega_2(3\eta-\chi_1)-\omega_1(3\eta-2\chi_1)\right].$$

As above, representing the general solution of Eq. (38) as a sum of the solutions of the corresponding inhomogeneous and homogeneous equations using the boundary condition (19), we obtain

$$v^{(2)} = T_{12}\left\{\exp\left[(2\eta-\chi_1)z+i\left(\Omega t-\alpha_2 z+\varphi\right)\right]-K\right\}, \tag{40}$$

where

$$T_{12} = \frac{R}{c_\mathrm{F}^2\left[\alpha_2^2+(2\eta-\chi_1)\chi_1+2i(\eta-\chi_1)\alpha_2-\Omega^2/c_\mathrm{F}^2\right]}, \tag{41}$$

$$K = \begin{cases} \exp\left[i\left(\Omega t+\varphi\right)+\left(1-\sqrt{1-\Omega^2/\omega_\mathrm{cf}^2}\right)\eta z\right], \\ \Omega<\omega_\mathrm{cf} \\ \exp\left[\eta z+i\left(\Omega t-\alpha_2 z+\varphi\right)\right], \quad \Omega>\omega_\mathrm{cf}. \end{cases} \tag{42}$$

The first term in (40), which is the solution of the inhomogeneous equation (38), corresponds to propagating MAG waves over the entire range of difference frequencies Ω; the higher the frequency ω_1 of the primary nonpropagating wave, the faster is the increase in the amplitude of these waves with height. In contrast, the second term in (40), which is the solution of the corresponding homogeneous equation (38), corresponds to propagating or nonpropagating MAG waves, depending on whether the difference frequency Ω is higher or lower than the cutoff frequency.

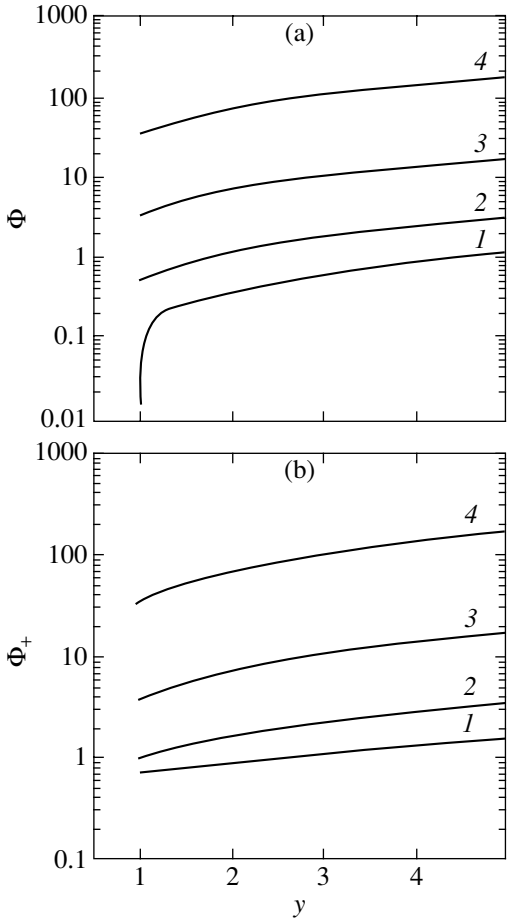

Fig. 6. Quantities Φ (a) and Φ_+ (b) versus dimensionless frequency $y=\omega_2/\omega_\mathrm{cf}$ for $\sigma=1$: $\omega_1=0.999\omega_\mathrm{cf}$ (*1*), $\omega_1=0.5\omega_\mathrm{cf}$ (*2*), $\omega_1=0.1\omega_\mathrm{cf}$ (*3*), and $\omega_1=0.01\omega_\mathrm{cf}$ (*4*).

It should be noted here that expressions (39)–(42) can formally be used to describe the generation of MAG waves at the sum frequency $\Omega_+=\omega_2+\omega_1$ ($\omega_1<\omega_\mathrm{cf}$, $\omega_2>\omega_\mathrm{cf}$) if they are transformed as follows:

$$\omega_1\to-\omega_1, \quad \Omega\to\Omega_+. \tag{43}$$

We see from (40), (42), and (43) that, if one of the primary MAG waves is a propagating one, then solely propagating waves are generated at the sum frequency.

The following conclusions can be drawn from the numerically computed ω_1, ω_2, and $\sigma=1/\beta$ dependences of the normalized quantities $\Phi=|T_{12}c_0/A_1A_2|$

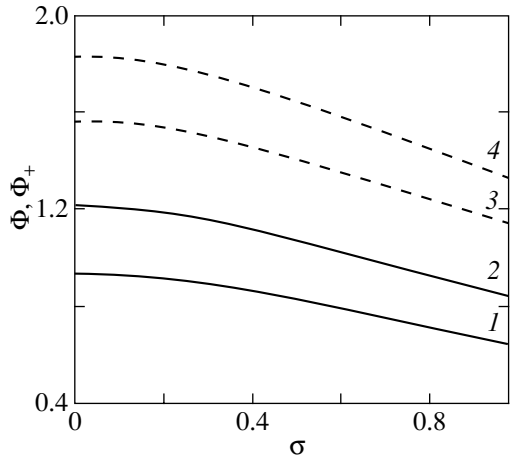

Fig. 7. Normalized quantities Φ (solid line) and Φ_+ (dotted line) versus σ for $\omega_1 = 0.5\omega_L$: $\Omega = 0.7\omega_L$ (*1*, *3*); $\Omega = \omega_L$ (*2*, *4*).

and Φ_+ [the expression for Φ_+ follows from Φ after transformations (43)] shown in Figs. 6 and 7, which characterize the oscillation velocity amplitudes at the difference and sum frequencies in each of the two groups of waves at $z = 0$, respectively.

First, Φ and Φ_+ increase with increasing difference and sum frequencies, respectively; as follows from Fig. 6 and from expressions (40)–(43), they indefinitely increase as $\omega_1 \to 0$ and $\omega_2 \to \infty$. However, such an indefinite increase in the amplitudes of each of the waves at frequencies Ω and Ω_+ does not cause a similar increase in the amplitude of the total oscillation in the corresponding limiting situations, because the following relations hold:

$$v^{(2)}\Big|_{\Omega} \to -\,v^{(2)}\Big|_{\Omega_+}, \quad \begin{cases} \Omega|_{\omega_1 \to 0} \to \Omega_+ \\ \Omega|_{\omega_2 \to \infty} \to \Omega_+. \end{cases} \qquad (44)$$

Naturally, significant differences in the behavior of Φ and Φ_+ show up only at radiation frequencies ω_1 and ω_2 close to ω_{cf} (see Fig. 6). In this case, the sharp decrease in the wave amplitudes at difference frequencies to zero at $\omega_1 \to \omega_{cf}$ and $\omega_2 \to \omega_{cf}$ is attributable to the absence of an acoustic wind in the corresponding situation: $V = 0$ for $\omega_1 = \omega_2 = \omega_{cf}$ [see (27)].

Second, as the Alfvén velocity increases, the amplitudes of the nonlinearly generated MAG waves decrease appreciably (see Fig. 7); the rate of their increase with height z also decreases [see (40), (42)].

CONCLUSIONS

Below, we formulate our main results and the conclusions that follow from them.

Based on a plane-parallel isothermal solar model atmosphere permeated by a horizontal magnetic field whose strength is proportional to the square root of the ambient density, we investigated the parametric generation of MAG waves in the approximation of a specified field for vertically propagating MAG waves at frequencies above their cutoff frequency.

We showed that both nonpropagating (inhomogeneous) and propagating MAG waves are excited in the frequency range of interest above the cutoff frequency and, hence, forbidden for the propagation of MAG waves during their linear generation at the corresponding difference frequency through the nonlinear interaction between initially propagating MAG waves, as in the case of interaction between AG waves (see M. Petukhov and Yu. Petukhov 2001). The oscillation velocity amplitude for propagating MAG waves at a difference frequency increases with height in inverse proportion to the decreasing ambient density, i.e., appreciably faster than it does for primary waves at the corresponding frequency. For the latter waves, this amplitude increases in inverse proportion to the square root of the decreasing ambient density. The quantity Φ, which characterizes the oscillation velocity amplitude for the MAG waves at a difference frequency near the lower atmospheric boundary, reaches its maximum $\Phi \approx 1$ in the absence of a magnetic field (see Fig. 3). We found that, as the magnetic-field strength increases, the amplitude of the MAG waves at a difference frequency decreases at radiation frequencies of the primary waves above a certain selected frequency and increases at radiation frequencies below this selected frequency only at relatively small heights. We also noticed that the selected radiation frequency itself decreases with increasing difference frequency.

We established that during the interaction between MAG waves, as well as AG waves (see M. Petukhov and Yu. Petukhov 2001), an acoustic flow (wind) is formed at a zero difference frequency. Its velocity depends on the initial phase difference between the oscillations at the lower solar atmospheric boundary. Increasing with height in inverse proportion to the decreasing ambient density, it is directed oppositely to the propagation of MAG waves. We found the following: first, the acoustic wind velocity does not depend on the radiation frequency and decreases with increasing magnetic-field strength at relatively high radiation frequencies, well above the cutoff frequency; second, at relatively low radiation frequencies close to the cutoff frequency, the dependence of the acoustic wind velocity on magnetic-field strength has a maximum whose position changes only slightly at relatively small (compared to the scale height) heights and significantly, in inverse proportion to the square root of the height, at relatively large heights.

In addition, we investigated the nonlinear interaction between nonpropagating and propagating MAG

waves. We showed that both nonpropagating and propagating MAG waves are generated during the interaction between initial disturbances from the forbidden frequency range at a sum frequency above the cutoff frequency. Their amplitude decreases with increasing magnetic-field strength. The quantity Ψ, which characterizes the amplitude of the MAG waves at a sum frequency, reaches its maximum $\Psi \approx 0.6$ in the absence of a magnetic field (see Fig. 5). We also found that, as in the case of interaction between AG waves (see M. Petukhov and Yu. Petukhov 2001), nonpropagating MAG oscillations mainly contribute to the field of the MAG waves at a sum frequency and at relatively large heights in a certain range of radiation frequencies.

We established that during the nonlinear interaction between initially nonpropagating and propagating MAG waves, both nonpropagating and propagating MAG waves are generated at a difference frequency below the cutoff frequency and only propagating MAG waves are generated at a sum frequency. The amplitudes of the latter decrease with increasing magnetic-field strength. The dependences of the MAG wave amplitudes on radiation frequency at difference (see Φ in Fig. 6) and sum (see Φ_+ in Fig. 6) frequencies significantly differ only near the cutoff frequency, where the MAG wave amplitude decreases sharply at a difference frequency. However, at radiation frequencies well above the cutoff frequency, the amplitudes of these waves become equal $\Phi/\Phi_+ \approx 1$ (see Fig. 6).

Thus, the transfer of acoustic energy into the upper solar atmosphere by MAG waves is possible at relatively low difference frequencies, which are generated through the nonlinear interaction not only between propagating waves (see M. Petukhov and Yu. Petukhov 2001) but also between nonpropagating and propagating MAG waves. Furthermore, acoustic energy from the forbidden frequency range can also be effectively transferred into the upper solar atmosphere by MAG waves at relatively low sum frequencies, which are generated through the nonlinear interaction not only between nonpropagating waves but also between nonpropagating and propagating MAG waves.

ACKNOWLEDGMENTS

This study was supported by the Russian Foundation for Basic Research (project nos. 02-02-17374, 00-15-96619).

REFERENCES

1. C.-N. An, R. L. Moore, Z. E. Musielak, and S. T. Suess, Astrophys. J. **344**, 478 (1989).
2. V. Cadez, M. Gossens, B. Pinter, W. J. Tirray, and P. Vanlammel, Astrophys. J. **503**, 422 (1998).
3. W. R. Campbell and B. Roberts, Astrophys. J. **338**, 538 (1989).
4. É. E. Dubov, Itogi Nauki Tekh., Ser.: Astron. **14**, 148 (1978).
5. N. S. Dzhalilov and Y. D. Zhugzhda, Astron. Astrophys. **132**, 45 (1984a).
6. N. S. Dzhalilov and Y. D. Zhugzhda, Astron. Astrophys. **132**, 52 (1984b).
7. N. S. Dzhalilov and Y. D. Zhugzhda, Astron. Astrophys. **132**, 333 (1984c).
8. D. J. Evans and B. Roberts, Astrophys. J. **356**, 704 (1990).
9. R. Jain and B. Roberts, Astron. Astrophys. **286**, 243 (1994).
10. S. A. Kaplan, S. B. Pikel'ner, and V. N. Tsytovich, *Plasma Physics of the Solar Atmosphere* (Nauka, Moscow, 1977).
11. A. J. Miles and B. Roberts, Sol. Phys. **141**, 205 (1992).
12. Z. E. Musielak and B. A. Stark, Astrophys. J. **409**, 450 (1993).
13. A. N. Nye and J. H. Thomas, Astrophys. J. **204**, 573 (1976a).
14. A. N. Nye and J. H. Thomas, Astrophys. J. **204**, 582 (1976b).
15. L. A. Ostrovskiĭ and N. S. Petrukhin, Astron. Zh. **58**, 848 (1981) [Sov. Astron. **25**, 483 (1981)].
16. M. Yu. Petukhov and Yu. V. Petukhov, Pis'ma Astron. Zh. **27**, 220 (2001) [Astron. Lett. **27**, 186 (2001)].
17. M. Yu. Petukhov and Yu. V. Petukhov, Pis'ma Astron. Zh. **28**, 382 (2002) [Astron. Lett. **28**, 335 (2002)].
18. E. R. Priest, *Solar Magnetohydrodynamics* (Reidel, Dordrecht, 1982; Mir, Moscow, 1985).
19. J. H. Thomas and A. H. Nye, Phys. Fluids **18**, 490 (1975).
20. R. K. Ulrich, Astrophys. J. **465**, 436 (1996).

Translated by V. Astakhov

Astronomy Letters, Vol. 29, No. 2, 2003, pp. 126–132. Translated from Pis'ma v Astronomicheskiĭ Zhurnal, Vol. 29, No. 2, 2003, pp. 148–155.

The Region of Stable Motions around a Periodic Eight-Like Orbit in the General Three-Body Problem

V. V. Orlov[1*], A. V. Rubinov[1], and A. D. Chernin[2,3]

[1] *Astronomical Institute, St. Petersburg State University, Universitetskiĭ pr. 28, Petrodvorets, 198504 Russia*

[2] *Sternberg Astronomical Institute, Universitetskiĭ pr. 13, Moscow, 119992 Russia*

[3] *Tuorla Observatory, Turku University, Piikkio, 21500 Finland*

Received July 4, 2002

Abstract—We investigate the neighborhood of the periodic eight-like orbit found by Moore (1993) and Chenciner and Montgomery (2000). One-, two-, and three-dimensional scans in body coordinates, velocities, and masses were constructed. We found the regions of initial conditions in which the maximum mutual separation did not exceed 5 distance units during 2000 time units (about 300 periods of the initial solution). Larger deviations from the periodic solution lead to distant body ejections and escapes. The identified regions of finite motions are complex in structure. In some sections, these are simple-connected manifolds, while in other sections, stability zones alternate with escape zones. We estimated the fractal dimensions of the stability regions in three-dimensional scans: it typically ranges from 2 to 3. In some cases, we found transitions between motions along the figure of eight in its neighborhood and motions in the vicinity of a periodic Broucke orbit in the isosceles three-body problem. © *2003 MAIK "Nauka/Interperiodica"*.

Key words: *celestial mechanics*.

INTRODUCTION

The three-body problem is known to admit no general analytical solution, which makes special cases with exactly integrable equations of motion particularly interesting. These include, for example, the periodic orbits of von Schubart (1956) and Broucke (1979) in the rectilinear and isosceles three-body problems, respectively. Recently, the small collection of such solutions has been supplemented with a remarkable periodic solution in which three bodies move one after another along a closed curve similar to the figure of eight (Chenciner and Montgomery 2000).

Of particular interest are the stability of exact solutions and the behavior of neighboring orbits in the vicinity of a periodic orbit. According to the general theory of nonlinear dynamical systems, stable periodic orbits are commonly surrounded by regions of regular finite motions. In contrast, a complex trajectory behavior arises in the vicinity of unstable periodic orbits. This behavior leads to the development of dynamic chaos [see, e.g., Schuster 1984).

Simo (2002) was the first to analyze the stability of a eight-like periodic orbit. He showed that this solution was stable and constructed the stability region in the two-dimensional section of the set of initial conditions. Simo also analyzed the variations in the shape of the stability region with body masses and showed that the fraction of stable orbits rapidly decreased even in the case of small variations in the body masses ($\sim 10^{-3}$). A number of accompanying periodic orbits (choreographies) were also found. In contrast to the figure of eight, these orbits are unstable.

Here, we continue to study the stability of eight-

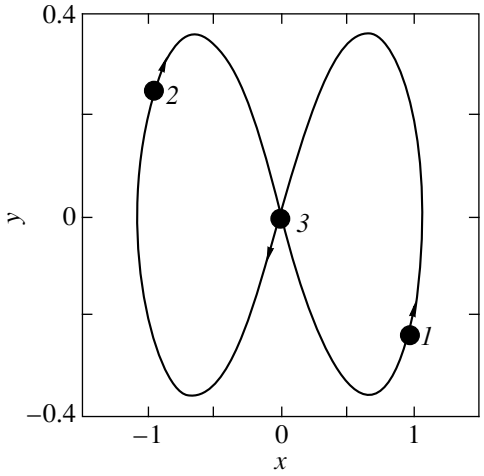

Fig. 1. The initial conditions for a periodic eight-like orbit.

*E-mail: vor@astro.spbu.ru

The intervals of deviation from the central solution within which $t > 2000$

Parameter	Body		
	1	2	3
x	$[-0.022, 0.018]$	$[-0.018, 0.022]$	$[-0.122, 0.122]$
	$[-0.022, 0.017]$	$[-0.018, 0.022]$	
y	$[-0.009, 0.011]$	$[-0.009, 0.008]$	$[-0.009, 0.009]$
	$[-0.009, 0.009]$		
z	$[-0.230, 0.230]$	$[-0.230, 0.230]$	$[-0.121, 0.121]$
	$[-0.230, 0.230]$		
vx	$[-0.020, 0.015]$	$[-0.020, 0.027]$	$[-0.022, 0.006]$
	$[-0.025, 0.025]$		
vy	$[-0.006, 0.003]$	$[-0.005, 0.003]$	$[-0.013, 0.010]$
	$[-0.008, 0.005]$		
vz	$[-0.078, 0.078]$	$[-0.076, 0.076]$	$[-0.168, 0.168]$
m	$[-0.00010, 0.00005]$	$[-0.00007, 0.00010]$	$[-0.00005, 0.00003]$
	$[-0.00006, 0.00004]$	$[-0.00007, 0.00005]$	$[-0.00005, 0.00003]$

like orbits. To this end, we constructed a set of one-, two-, and three-dimensional scans in the space of initial conditions for the problem. Based on new material and using a new method, we confirm Simo's conclusion that regions of finite motions exist in the vicinity of the initial orbit. Our set of scans also gives an idea of the structure of these domains and the geometry of their boundaries. We describe the eight-like orbit and our method and present our results.

THE EIGHT-LIKE ORBIT

This orbit was found in the plane three-body problem with equal-mass components and zero angular momentum (Chenciner and Montgomery 2000). The initial conditions are (see Fig. 1):

$$x_1 = -x_2 = 0.97000436,$$
$$y_1 = -y_2 = -0.24308753,$$
$$x_3 = y_3 = 0 = z_1 = z_2 = z_3 = 0,$$
$$\dot{x}_3 = -2\dot{x}_1 = -2\dot{x}_2 = -0.93240737,$$
$$\dot{y}_3 = -2\dot{y}_1 = -2\dot{y}_2 = -0.86473146,$$
$$\dot{z}_1 = \dot{z}_2 = \dot{z}_3 = 0.$$

The period of the system is $\bar{T} = 6.32591398$ time units in the system of units used by Chenciner and Montgomery (2000), where the gravitational constant is $G = 1$ and the body masses are $m_1 = m_2 = m_3 = 1$.

The bodies move one after another along the figure of eight with no close double and triple encounters. Note that this orbit was first found numerically by Moore (1993).

THE SCANNING ALGORITHM

We carried out all our computations by using the TRIPLE code that was kindly provided by S. Aarseth (Cambridge University, Great Britain). This code uses the regularization of the equations of motion

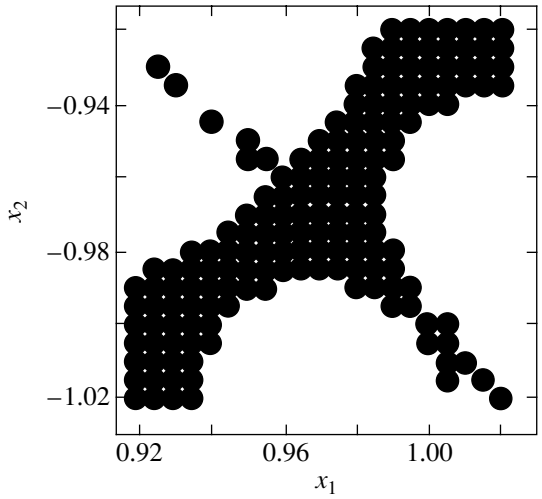

Fig. 2. A more detailed structure of the stability region on the two-dimensional scan in coordinates x_1 and x_2 of the extreme bodies. The scanning step is 0.005 in both coordinates.

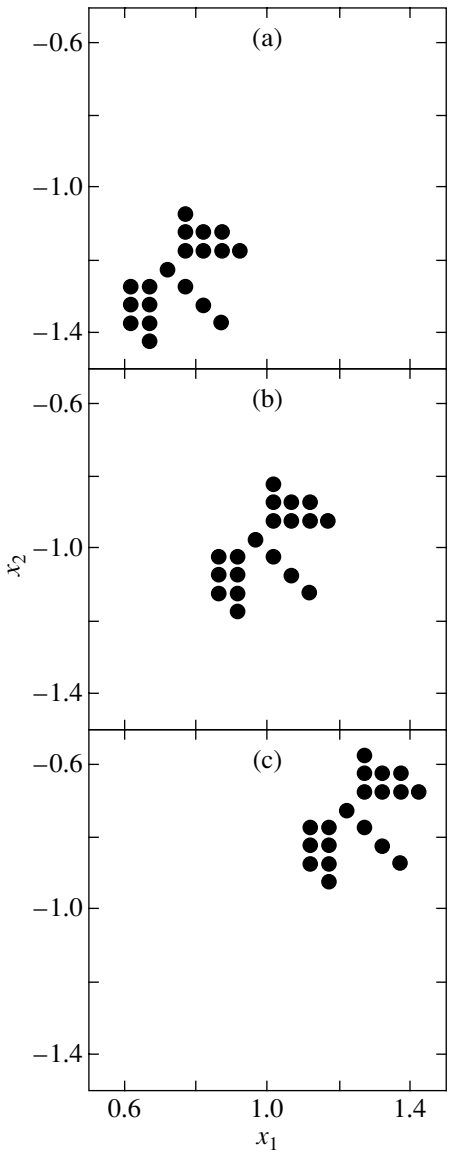

Fig. 3. Displacement of the stability region on the (x_1, x_2) plane as the coordinate x_3 of the central body varies: (a) $\Delta x_3 = -0.25$; (b) $\Delta x_3 = 0$, and (c) $\Delta x_3 = 0.25$. The scanning step is 0.05 in both coordinates x_1, x_2.

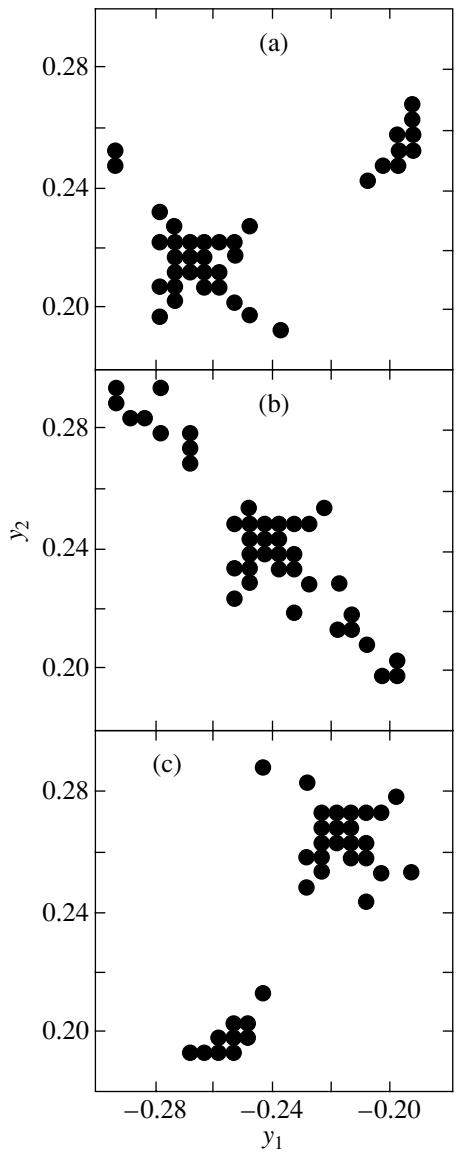

Fig. 4. Displacement of the stability region on the (y_1, y_2) plane as the coordinate y_3 of the central body varies: (a) $\Delta y_3 = -0.025$; (b) $\Delta y_3 = 0$, and (c) $\Delta y_3 = 0.025$. The scanning step is 0.005 in both coordinates y_1, y_2.

for the three-body problem by the method of Aarseth and Zare (1974) and the integrator of Bulirsch and Stoer (1966). For checking purposes, we also made some of the one-dimensional scans by using our CHAIN code implementing the chain regularization by the method of Mikkola and Aarseth (1993) and a fourth-order Runge–Kutta integrator. The two codes yielded similar results.

First, we made one-dimensional scans in each of the initial body coordinates and velocities starting from the initial eight-like solution and proceeding by increasing and decreasing the corresponding coordinate or velocity. Similarly, we performed scanning in each of the body masses. In the case of one-dimensional scanning, the remaining body coordinates, velocities, and masses were assumed to be equal to the values corresponding to the initial solution.

The scanning step was 0.001 in coordinates and velocities and 0.00001 in masses. For each set of initial conditions, the computations continued either until 2000 time units (about 300 periods of the solution $\bar{T}$) or until the maximum mutual separation exceeded five distance units. Note that at the initial time, the maximum mutual separation was equal to two distance units. Test computations showed that in the cases where the latter condition was satisfied,

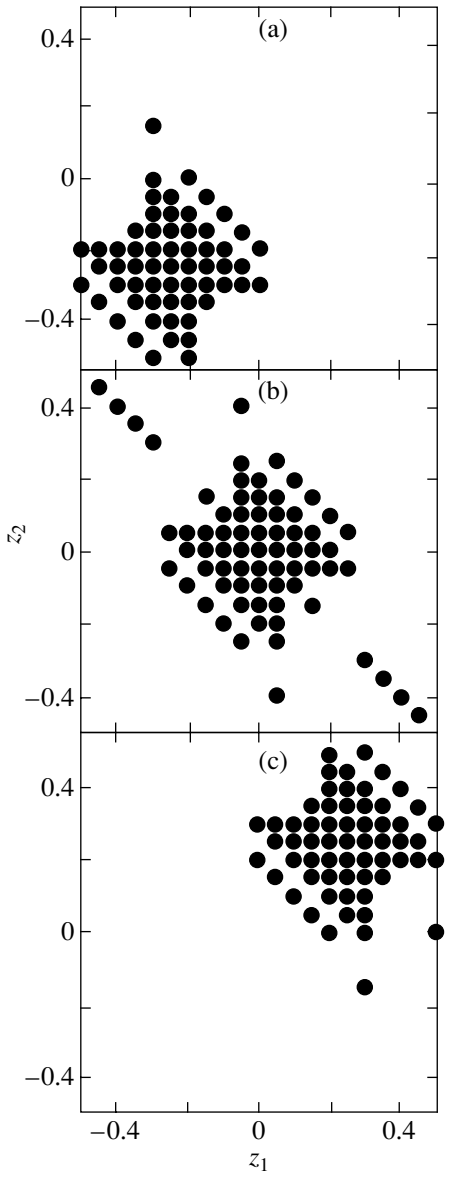

Fig. 5. Displacement of the stability region on the (z_1, z_2) plane as the coordinate z_3 of the central body varies: (a) $\Delta z_3 = -0.25$; (b) $\Delta z_3 = 0$, and (c) $\Delta z_3 = 0.25$. The scanning step is 0.05 in both coordinates z_1, z_2.

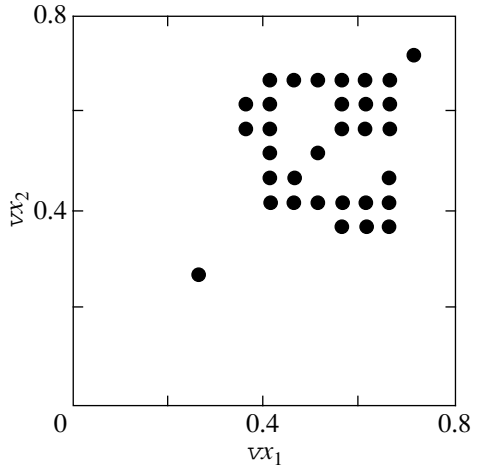

Fig. 6. The stability region on the (vx_1, vx_2) plane for $\Delta vx_3 = 0$. The scanning step in vx_1 and vx_2 is 0.05.

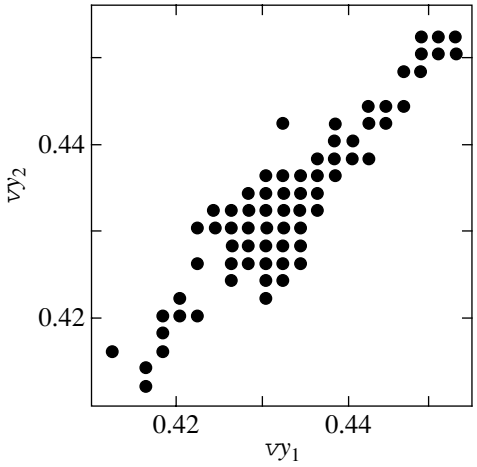

Fig. 7. The stability region on the (vy_1, vy_2) plane for $\Delta vy_3 = 0$. The scanning step in vy_1 and vy_2 is 0.002.

motions in the triple system almost always lead to distant body ejections and, in the long run, to the breakup of the triple system.

We constructed three-dimensional scans in the vicinity of the initial solution for various combinations of body coordinates, velocities, and masses and with various scanning steps. In the process, we identified the points of the three-dimensional grid at which $t > t_c = 2000$ time units; the manifold of these grid points represented the stability region in the scan considered. Below, we use the term "stability" to mean "the boundedness of the motions within the above limits during at least 2000 time units."

We estimated the fractal dimensions of these manifolds. To this end, we constructed a rectangular parallelepiped around each of the points that were not too close to the scan boundary that contained the same number of grid points along each of its faces and determined the number of points with $t > 2000$ within this parallelepiped. We then determined the mean number N of such points over all possible parallelepipeds and plotted $\log N$ against $\log n$, where n is the number of grid points lying on the parallelepiped face. The slope of the $\log N(\log n)$ curve yields an estimate of the fractal dimension D. The error of D can be estimated, for example, by the least-squares method.

To test the stability of our method against the choice of a critical time t_c, apart from 2000 time units, we also considered a critical value of 5000 time units for some of the scans. The two critical times yielded

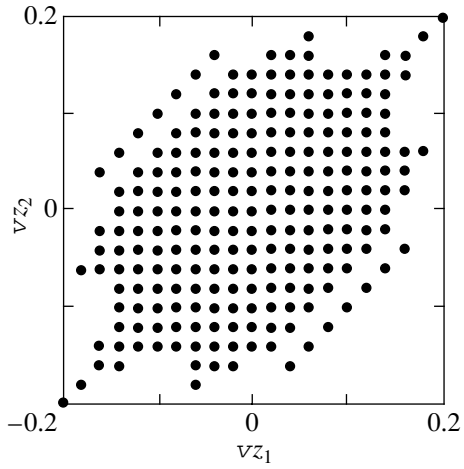

Fig. 8. The stability region on the (vz_1, vz_2) plane for $\Delta vz_3 = 0$. The scanning step in vz_1 and vz_2 is 0.02.

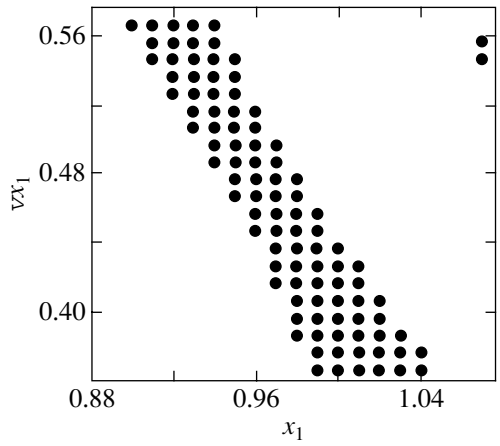

Fig. 9. The (x_1, vx_1) section with a scanning step of 0.01.

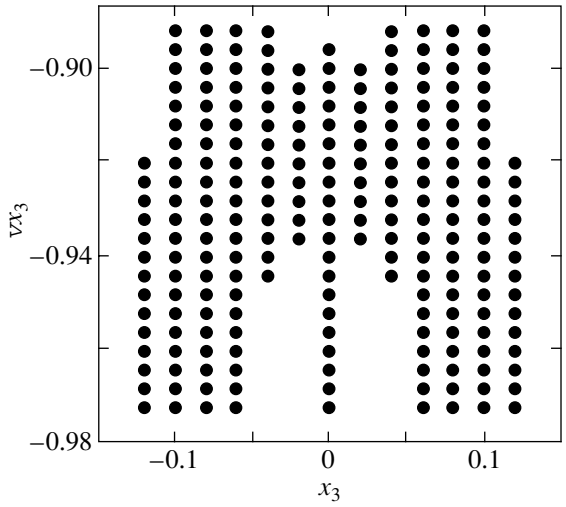

Fig. 10. The (x_3, vx_3) section with a scanning step of 0.02 in x_3 and of 0.005 in vx_3.

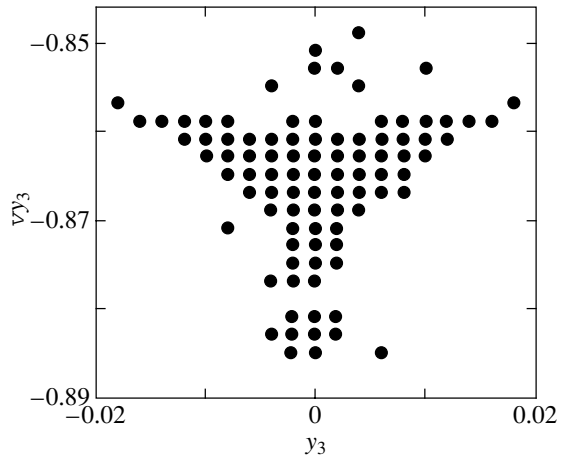

Fig. 11. The (y_3, vy_3) section with a scanning step of 0.002.

similar boundaries of the stability region. We found only a relatively small intermediate zone of points with $2000 < t < 5000$ (see the "Results" below).

This result agrees with the analysis by Simo (2002), who showed that the fraction of nondisrupted trajectories decreases slowly with increasing time. This quantity apparently tends to some constant value as $t \to \infty$.

RESULTS

The results of our one-dimensional scanning are presented in the table. It gives the boundaries of the ranges of body coordinates, velocities, and masses within which $t > 2000$ time units. Also listed are the deviations from the initial solution toward smaller and larger values of a particular parameter. For some of the scans, independent results were also obtained by using the CHAIN code. These results are given in the lower rows of the table. In general, the boundaries found with the two different codes are in agreement.

We see from the table that, in the case of one-dimensional scanning, the maximum size of the stability region in a given scan is reached when the extreme bodies are displaced along the z axis, when the central body is displaced along the x and z axes, and when the z velocity components vary. The stability of motions is most sensitive to variations in the body masses.

Consider two- and three-dimensional scans in several pairs and triples of parameters in the space of initial conditions. The results are presented in Figs. 2–15. These figures show the two-dimensional sections of the three-dimensional scans obtained. The filled circles correspond to the initial conditions with $t > 2000$ time units. At the remaining grid

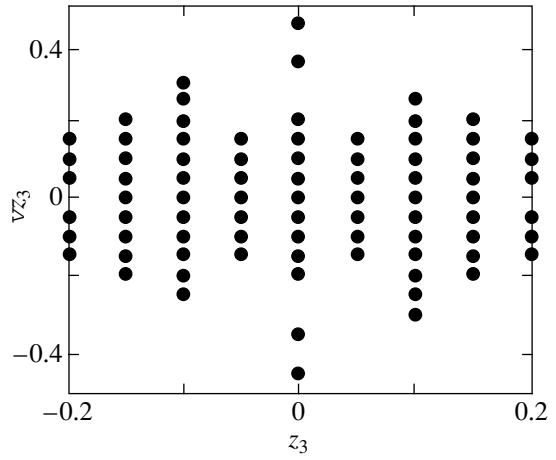

Fig. 12. The (z_3, vz_3) section with a scanning step of 0.05.

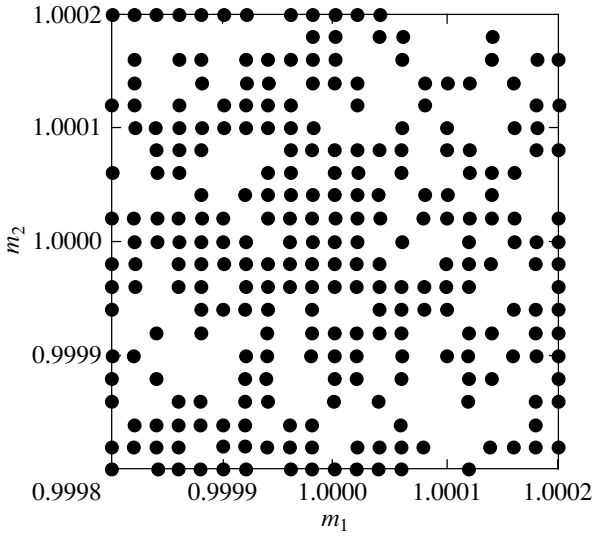

Fig. 13. The (m_1, m_2) section with a scanning step of 2×10^{-5}.

points, the maximum separation between the bodies exceeded five distance units in less than 2000 time units. The characteristics of the scans and sections (the parameters in which the scanning was made and the scanning step) are given in the captions to the figures.

When the coordinates x_1 and x_2 of the extreme bodies are varied for a fixed coordinate x_3 of the central body, the stability region has the shape of a cross oriented along the $x_1 = x_2$ and $x_1 = -x_2$ diagonals (Fig. 2). As the coordinate x_3 increases, this structure is displaced from the lower left corner to the upper right corner while remaining self-similar (Fig. 3). The similarity stems from the fact that the initial configuration as a whole is displaced. Therefore, the evolution is closely reproduced.

A similar effect also shows up during the displacement in y and z coordinates (Figs. 4 and 5). During the displacement in y coordinate, other stability regions also appear in the upper right and lower left corners when the central body is displaced in y-coordinate.

When the y and z coordinates of the central body are varied, the stability region is elongated along the $y_2 = -y_1$ or $z_2 = -z_1$ diagonal. In addition to the continuous region, isolated "tails" elongated along this diagonal are observed in the vicinity of the initial solution.

Figures 6–8 show our results for the variations in initial velocities. The stability regions are elongated along the principal diagonals $vx_1 = vx_2$, $vy_1 = vy_2$, and $vz_1 = vz_2$. Note that the stability regions are followed by the "tails" of trajectories with long lifetimes oriented along the same diagonals. As the velocity of the central body is changed, the entire structure is displaced along the principal diagonal, as observed in Figs. 3–5.

Figures 9–12 show examples of the sections in one of the coordinates and the corresponding velocity component. These are a kind of Poincare sections. The stability regions have a variety of shapes in these sections.

The body masses can be treated as the parameters of the problem. Figures 13–15 show how the shape of the stability region depends on the masses. We can see from the table that even small mass variations ($\sim 10^{-4}$) result in the loss of system stability in the case of one-dimensional scanning. Such a strong sensitivity of the results to mass variations is confirmed by two-dimensional scans (Figs. 13–15). Here, the stability regions have a complex multiply connected structure. Their fractal dimension is $D \approx 2.6$ for a scanning step of $\Delta m_1 = \Delta m_2 = \Delta m_3 = 0.002$ and $D \approx 3.0$ for smaller scanning steps, 0.0002 and 0.00002, in each of the masses. Thus, the distribution of points approaches a uniform distribution with decreasing scanning step.

Note that at a 2×10^{-6} step, a continuous stability region exists around the initial solution. It also shows up in Fig. 13. This region is also preserved if we increase the critical time to 5000 units (almost 800 initial periods). Only in the vicinity of the boundary of the stability region do several trajectories become unstable in the time interval from 2000 to 5000 time units.

The strong sensitivity of the results to small mass variations agrees with the results of Simo (2000), who also pointed out a rapid decrease in the fraction of stable orbits with increasing scanning step in body masses.

When the initial body coordinates and/or velocities are varied, the constructed stability regions also

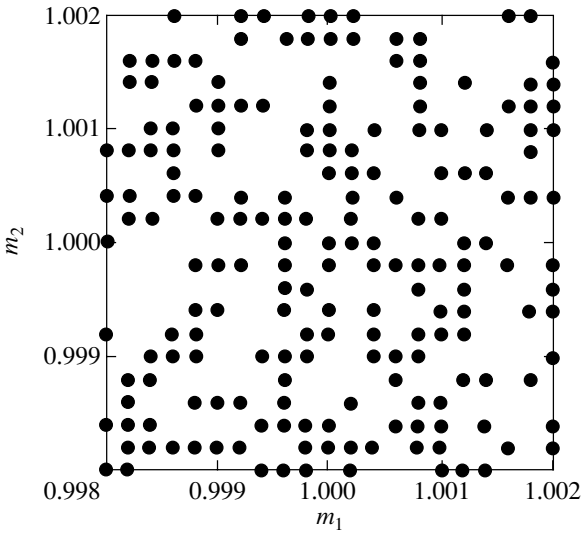

Fig. 14. The (m_1, m_2) section with a scanning step of 2×10^{-4}.

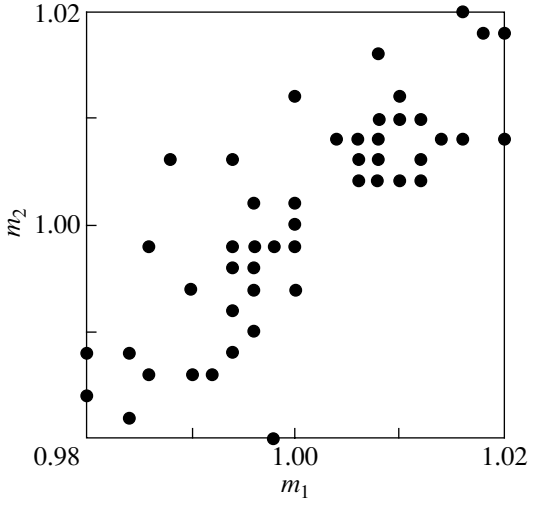

Fig. 15. The (m_1, m_2) section with a scanning step of 2×10^{-3}.

exhibit fractal properties, with the fractal dimension varying between 2 and 3. The specific value of D depends (within these limits) on the scanning step.

Previously, Heinämäki *et al.* (1998) found a fractal dimension slightly exceeding 2 by analyzing the time series generated by three-body systems in numerical simulations. A low fractal dimension is characteristic of the dynamics of triple systems that exhibit the property of intermittency (Chernin and Valtonen 1998).

Finally, when analyzing the trajectories in the vicinity of the figure of eight, we found the remarkable cases of the rearrangement of motions from one periodic orbit to another and back: the motions along the figure of eight change to oscillations near the orbit of Broucke (1979) for the isosceles three-body problem and then return to the neighborhood of the figure of eight. In this case, the motions remain bounded during at least 2000 time units. This probably means that the regions of regular finite motions generated by the periodic Broucke and eight-like orbits close up in phase space. This effect is currently being analyzed in more detail and the results will be published separately.

Note that Simo (2002) performed a detailed analysis of the stability of a periodic eight-like orbit both in the linear approximation (by calculating the eigenvalues of the Poincare mapping) and in the general case (using numerical differentiation). He proved the stability of this periodic solution in both cases. For further studies, it is of interest to analyze the stability of other choreographies and the relative positions of the stability regions in phase space.

ACKNOWLEDGMENTS

V. Orlov and A. Rubinov wish to thank the Foundation for Support of Leading Scientific Schools (project no. 00-15-96775), the Russian Foundation for Basic Research (project no. 02-02-17516), and the "Universities of Russia" Program of the Ministry of Education of Russia (project no. UR.02.01.027). We are grateful to the referee for several valuable remarks.

REFERENCES

1. S. J. Aarseth and K. Zare, Celest. Mech. **10**, 185 (1974).
2. R. Broucke, Astron. Astrophys. **73**, 303 (1979).
3. R. Bulirsch and J. Stoer, Numer. Math. **8**, 1 (1966).
4. A. Chenciner and R. Montgomery, Ann. Math. **52**, 881 (2000).
5. A. D. Chernin and M. J. Valtonen, New Astron. Rev. **42**, 41 (1998).
6. P. Heinämäki, H. J. Lehto, M. J. Valtonen, and A. D. Chernin, Mon. Not. R. Astron. Soc. **298**, 790 (1998).
7. S. Mikkola and S. J. Aarseth, Celest. Mech. Dyn. Astron. **57**, 439 (1993).
8. C. Moore, Phys. Rev. Lett. **70**, 3675 (1993).
9. H. G. Schuster, *Deterministic Chaos* (Physik-Verlag, Weinheim, 1984; Mir, Moscow, 1988).
10. C. Simó, Preprint (Univ. Barselona, Spain, 2002).
11. J. von Schubart, Astron. Nachr. **283**, 17 (1956).

Translated by A. Dambis

Astronomy Letters, Vol. 29, No. 2, 2003, pp. 65–69. Translated from Pis'ma v Astronomicheskiĭ Zhurnal, Vol. 29, No. 2, 2003, pp. 83–87.

Delay of Emission from Extragalactic Gamma-Ray Burst Sources As a Test for Selecting a Model of the Universe

E. G. Vertogradova, Yu. S. Grishkan, and V. B. Petkov*

Institute for Nuclear Research, Russian Academy of Sciences, pr. Shestidesyatiletiya Oktyabrya 7a, Moscow, 117312 Russia

Received March 13, 2002

Abstract—We obtained an order-of-magnitude estimate for the dispersion of light caused by the effect of quantum fluctuations on the propagation of electromagnetic waves in four-dimensional spacetime. We calculated the delay of the photons from cosmological gamma-ray bursts (GRBs) for the flat, open, and closed cosmological models. This delay is attributable to the effect of expansion of the Universe on the propagation of a dispersive light wave in space. Analysis shows that the delay of GRB photons contains a regular component related to the expansion of the Universe. We conclude that cosmological models of the Universe can be selected by the delay of emission of various energies from GRBs; the accuracy of measuring the parameter $\Delta t/\Delta E_\gamma$ must be no lower than 10^{-6} s MeV^{-1}. © *2003 MAIK "Nauka/Interperiodica".*

Key words: *cosmology, gamma-ray bursts.*

INTRODUCTION

It has recently been hypothesized that the global Lorentz invariance in nature is only an approximate symmetry and can be violated at sufficiently high energies of the elementary particles involved in various physics interactions (Amelino-Camelia *et al.* 1998; Coleman and Glashow 1999; Stecker and Glashow 2001). The generation of non-Lorentzian spacetime metric components through quantum fluctuations (Ellis *et al.* 1998) is considered as a possible mechanism of this violation. For Planckian spacetime scales, quantum fluctuations significantly affect the large-scale spacetime structure (Hawking *et al.* 1980) by initiating, in particular, the birth of the Universe from a vacuum and quantum inflation (Vertogradova and Grishkan 2000). Quantum fluctuations on such small scales also exist at present and can affect the propagation of light in spacetime. Indeed, as was shown by Ellis *et al.* (1998, 2000a), the quantum fluctuations that constitute spacetime foam can effectively influence the macroscopic properties of the flat space metric by forming virtual D-brane-type topological defects (see, e.g., Rubakov 2001). When propagating in such space, the photons and other (almost) massless particles (e.g., neutrinos) are scattered by defects and the nondiagonal spacetime metric components are generated during the scattering (Ellis 2000):

$$g_{0\alpha} \sim \frac{u_\alpha}{c}.$$

Here, the Greek subscripts take on the values $\alpha = 1, 2, 3$ and c is the speed-of-light constant. The vector u_α is the effective defect recoil velocity when the particles propagate in spacetime foam, with its magnitude being $u \ll c$.

The existence of a macroscopic recoil velocity vector u_α violates the global Lorentz invariance (Coleman and Glashow 1999) and causes the dispersive properties of the light waves propagating in space to change:

$$c(E) = c\left(1 - \frac{u}{c}\right), \tag{1}$$

where $E = \hbar\omega$ is the energy of the photons of frequency ω. In quantum gravity, in particular, in the theory of spacetime foam (Ellis *et al.* 2000a), the velocity vector u_α must arise from quantum fluctuations and at a given energy E is of the order of the ratio of the energy scale for the recorded photons to the energy scale on which quantum spacetime fluctuations show up:

$$\frac{u}{c} \sim \frac{E}{M_{\rm QG}}, \tag{2}$$

where $M_{\rm QG}$ is the characteristic quantum-gravity energy scale. To a first approximation, the time delay of the light signal from an emitting source attributable to the path difference between the photons that travel at speeds c and $c - \Delta u$ is

$$\Delta t = \frac{\Delta L}{c} = \int_t^{t_0} \frac{\Delta u(E)}{c} dt. \tag{3}$$

*E-mail: vpetkov@yandex.ru

1063-7737/03/2902-0065$24.00

Here, L is the distance traveled by the light, t is the photon emission time, and t_0 is the photon detection time that corresponds to the age of the Universe.

Since the light propagates in space filled with small quantum fluctuations, the spacetime foam composed of them can be probed by the signals from distant radiation sources (primarily gamma-ray burst (GRB) sources) with a sufficiently high energy E. For delays Δt of the signals from radiation sources, the fundamental physical constant $M_{\rm QG}$, which characterizes the order of magnitude of the quantum-gravitational processes, can then be defined as the ratio

$$M_{\rm QG} \sim \frac{L\Delta E}{c\Delta t}. \tag{4}$$

Extragalactic GRBs can be used as pulsed sources of high-energy gamma-ray photons. Ellis *et al.* (2000b) and Nanopoulos (2000) studied the time delay in the arrival of photons with various energies from GRBs by using BATSE and OSSE data (Paciesas *et al.* 1999; OSSE Collaboration 1999). For the quantum-gravity energy scale $M_{\rm QG}$ to be estimated, the signal delays in the expanding Universe calculated from the formulas that were derived in terms of currently accepted cosmological models must be associated with the experimentally determined times Δt. In this case, the possible appearance of the time delay in the arrival of photons with various energies attributable to the nature of the GRBs is disregarded.

THE DELAY OF THE LIGHT PROPAGATING IN THE EXPANDING UNIVERSE AS A FUNCTION OF THE REDSHIFT OF EXTRAGALACTIC OBJECTS

In the expanding Friedmann–Robertson–Walker Universe with an arbitrary curvature of three-dimensional space, the 0–0 component of the Einstein equations is [see, e.g., the review article by Sahni and Starobinsky 2000; Hagiwara *et al.* 2002]

$$\frac{\dot a^2}{a^2} + \frac{kc^2}{a^2} = H_0^2\left[\Omega_m\left(\frac{a_0}{a}\right)^3 + \Omega_\Lambda\left(\frac{a_0}{a}\right)^{3(w+1)} + \Omega_r\left(\frac{a_0}{a}\right)^4\right], \tag{5}$$

where a_0 is the scale factor at present; a is the scale factor at time t; and the parameter $k = 1, 0, -1$ for the closed, flat, and open models of the Universe, respectively. The parameters Ω_Λ, Ω_m, and Ω_r are the ratios of the vacuum, matter, and radiation energy densities at present time t_0 to the critical density

$$\rho_c = \frac{3H_0^2}{8\pi G}.$$

The parameter $-1 < w < 0$ specifies the equation of state $p = w\rho$ for quintessence (Sahni and Starobinsky 2000; Huterer and Turner 1999; Peebles and Ratra 2002). The Hubble constant was taken from Wang *et al.* (2001):

$$H_0 = 100h\ {\rm km\ s^{-1}\ Mpc^{-1}}, \quad h = 0.7 \pm 0.1.$$

At moderately high redshifts $z \ll 1000$, we can disregard the radiation energy density and write Eq. (5) directly in terms of the redshift and the dimensionless curvature of three-dimensional space Ω_K

$$z = \frac{a_0}{a} - 1, \qquad \Omega_K = -\frac{kc^2}{a_0^2H_0^2},$$

$$H^2 \equiv \frac{\dot a^2}{a^2} = H_0^2\left[\Omega_m(1+z)^3 + \Omega_\Lambda(1+z)^{3(w+1)} + \Omega_K(1+z)^2\right]. \tag{6}$$

The condition for the relationship between the cosmological parameters follows from relations (6):

$$\Omega_m + \Omega_\Lambda + \Omega_K = 1. \tag{7}$$

As we know from observations (Wang *et al.* 2001; Efstatiou *et al.* 2001), the following constraints were imposed on these parameters:

$$\Omega_n = 0.3 \pm 0.1, \quad \Omega_\Lambda = 0.7 \pm 0.1,$$
$$\Omega_K = 0.0 \pm 0.06.$$

Integrating (6) together with (3) yields an expression for the delay of the light from a source:

$$\Delta t = \frac{1}{H_0}\int_1^{z+1}\frac{\Delta u}{c} \times \frac{dx}{x[\Omega_m x^3 + \Omega_\Lambda x^{3(w+1)} + \Omega_K x^2]^{1/2}}. \tag{8}$$

We now take into account the fact that the dispersion of light in the linear approximation as it propagates in curved spacetime is given by expressions (1) and (2) and that the energy difference between the photons changes as $\Delta E = \Delta E_\gamma(1+z)$, where ΔE_γ is the photon energy difference at the detection time. The ratio of the delay to the energy difference between the detected photons then takes the form

$$\frac{\Delta t}{\Delta E_\gamma} = \frac{1}{H_0 M_{\rm QG}} \times \int_1^{z+1}\frac{dx}{[\Omega_m x^3 + \Omega_\Lambda x^{3(w+1)} + \Omega_K x^2]^{1/2}}. \tag{9}$$

For $w = -1$ (a stable cosmic vacuum without quintessence), the asymptotic expressions for Δt

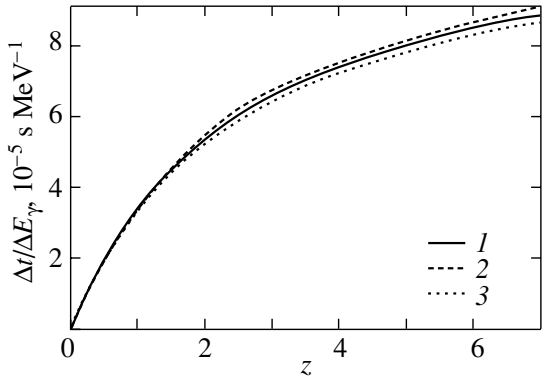

Fig. 1. Theoretical dependences of $\Delta t/\Delta E_\gamma$ on redshift z for various values of $k = 0, \pm 1$: (*1*) for the flat cosmological model, (*2*) for the closed cosmological model, (*3*) for the open cosmological model. The range of high redshifts $3 < z < 5.5$ is shown separately in Fig. 2.

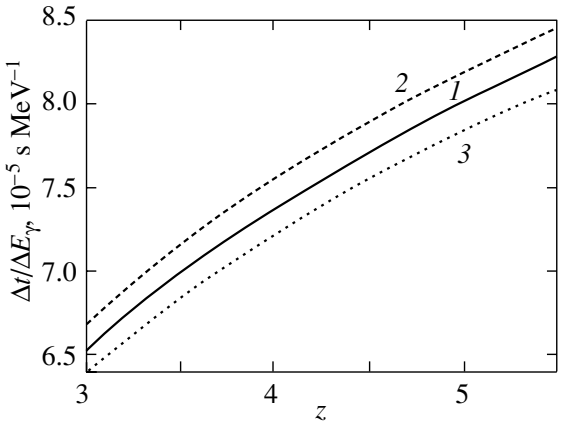

Fig. 2. Theoretical dependences of $\Delta t/\Delta E_\gamma$ on redshift $3 < z < 5.5$: (*1*) for the flat cosmological model at cosmological parameters $\Omega_m = 0.3$, $\Omega_\Lambda = 0.7$, $\Omega_K = 0$; (*2*) for the closed model at $\Omega_m = 0.3$, $\Omega_\Lambda = 0.76$, $\Omega_K = -0.06$; (*3*) for the open cosmological model at $\Omega_m = 0.3$, $\Omega_\Lambda = 0.64$, $\Omega_K = 0.06$.

match the expressions from Ellis *et al.* (2000b) to within constants of the order of unity:

$$\frac{\Delta t}{\Delta E_\gamma} = \frac{1}{\Omega_\Lambda^{1/2} H_0 M_{\rm QG}} z \quad (z \to 0), \qquad (10)$$

$$\frac{\Delta t}{\Delta E_\gamma} = \frac{2}{\Omega_m^{1/2} H_0 M_{\rm QG}} \tilde{z} \quad (z \to \infty), \qquad (11)$$

where

$$\tilde{z} = 1 - (1+z)^{-1/2}.$$

Formulas (10) and (11) correspond to the Hubble and Friedmann expansion of the Universe, respectively.

Thus, formula (11) in the Einstein theory is obtained only in the limit $z \to \infty$. That is why the redshift dependence of the signal delay changes in the exact theory compared to the result obtained in the Friedmann flat model (Ellis *et al.* 2000b), which is important in analyzing experimental data.

POSSIBILITIES FOR SELECTING COSMOLOGICAL MODELS USING OBSERVATIONAL DATA ON THE TIME DELAY OF THE SIGNALS FROM GAMMA-RAY BURST SOURCES

A stable cosmic vacuum (see, e.g., Saini *et al.* 2000; Peebles and Ratra 2002) is among the most probable realizations of dark energy in our Universe. Therefore, all our calculations were performed by disregarding quintessence ($w = -1$). Figure 1 shows the dependences of $\Delta t/\Delta E_\gamma$ on redshift z obtained from formula (9) for three cosmological models. The range of high redshifts $3 < z < 5.5$ is shown separately in Fig. 2. Here, curves *1*, *2*, and *3* correspond to the flat, closed, and open cosmological models,

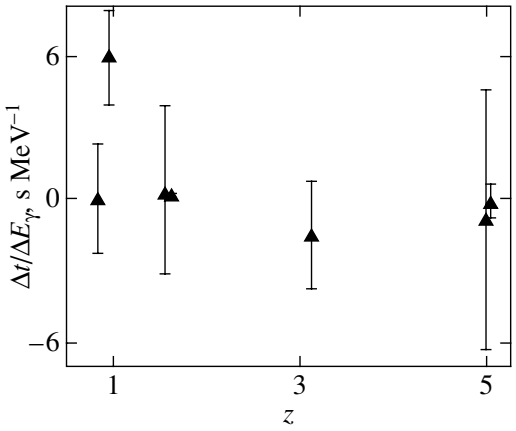

Fig. 3. Fits to the experimental data for GRBs from the BATSE and OSSE catalogs.

respectively. In this case, the quantum-gravity energy scale was fixed at a Planckian value of 10^{19} GeV. We see from the figure that the models are distinguishable between themselves if the accuracy of measuring $\Delta t/\Delta E_\gamma$ is not lower than 10^{-6} s MeV^{-1}.

Thus, the delays between gamma-ray photons of various energies and the GRB redshifts must be measured to choose a cosmological model (and to determine the quantum-gravity energy scale). Based on BATSE and OSSE data (Paciesas *et al.* 1999; OSSE Collaboration 1999), Ellis *et al.* (2000b) studied the time delay in the arrival of gamma-ray photons with various energies for five GRBs with measured redshifts: (1) GRB970508, $z = 0.835$; (2) GRB971214, $z = 3.14$; (3) GRB980329, $z = 5.0$; (4) GRB980703, $z = 0.966$; and (5) GRB990123,

$z = 1.60$. The time delay between the pulses recorded in channel 1 (energy range 20–50 keV) and in channel 3 (100–300 keV) was obtained for all five GRBs. Two GRBs, GRB980329 and GRB990123, were also detected by OSSE (1–5 MeV); the delay between OSSE and BATSE channel 3 was obtained for them. Figure 3 shows the values of $\Delta t/\Delta E_\gamma$ that we determined from the data of Ellis *et al.* (2000b) for five GRBs and two energy measuring channels as a function of redshift z. It follows from comparison of Figs. 1, 2, and 3 that the accuracy of the currently available experimental data is too low to choose between the cosmological models even if $M_{\rm QG}$ is known.

CONCLUSIONS

One might expect that the analysis of a more representative statistical sample of GRB sources with the simultaneous measurement of the time delays between gamma-ray photons of various energies at a known redshift will allow more accurate comparisons to be made between theory and experiment than is currently possible. Clearly, the quantum-gravity energy scale $M_{\rm QG}$ and the cosmological parameters cannot be simultaneously determined from the experimental data on the delay of gamma-ray emission with various energies from GRBs with measured z.

Two variants of measurements are possible.

(1) The parameter $M_{\rm QG}$ can be determined from independent measurements, for example, from the time delay between the gamma-ray photons of various energies from AGN outbursts. For Markarian 421, such measurements were carried out at the Whipple Observatory (Biller *et al.* 1999), which allowed a constraint to be imposed on the quantum-gravity energy scale:

$$M_{\rm QG} \gtrsim 10^{16}\ \ {\rm GeV}.$$

Given $M_{\rm QG}$, the cosmological parameters can then be determined in principle from the z dependence of $\Delta t/\Delta E_\gamma$.

(2) The cosmological parameters can be reliably determined from the photometric distance D_L for supernovae (Starobinsky 1998; Huterer and Turner 1999; Nakamura and Chiba 1999; Saini *et al.* 2000; Weller and Albrecht 2001; Kujat *et al.* 2001). The proposed measurements then allow the quantum-gravity energy scale $M_{\rm QG}$ to be obtained. Note that the possibility of using GRBs (and their optical afterglows) at high redshifts $z \gtrsim 5$ to study the large-scale structure of the early Universe is currently being discussed in the literature (Lamb and Reichart 2000).

A lower limit on the quantum-gravity energy scale can be estimated by using the experimental data from Ellis *et al.* (2000) and formula (9):

$$M_{\rm QG} \gtrsim 10^{15}\ \ {\rm GeV}.$$

If the quantum-gravity energy scale is assumed to be $M_{pl} \sim 10^{19}$ GeV, then the ratio $\Delta t/\Delta E_\gamma$ must be measured with an accuracy of $\sim 10^{-6}$ s MeV^{-1} to study the delays of the signals from cosmological GRBs.

ACKNOWLEDGMENTS

This study was supported by the Russian Foundation for Basic Research (project no. 00-02-16095). We are grateful to participants of the Workshop at the Baksan Neutrino Observatory for a helpful discussion, to V.A. Rubakov, and to the referee for valuable remarks.

REFERENCES

1. G. Amelino-Camelia, J. Ellis, N. E. Mavromatos, *et al.*, Nature **393**, 763 (1998).
2. S. D. Biller, A. C. Breslin, J. Buckley, *et al.*, Phys. Rev. Lett. **83**, 2108 (1999).
3. S. Coleman and S. L. Glashow, Phys. Rev. D **59**, 116008 (1999).
4. G. Efstathiou, S. Moody, J. A. Peacock, *et al.*, astro-ph/0109152 (2001); Mon. Not. R. Astron. Soc. (in press).
5. J. Ellis, astro-ph/0010474 (2000).
6. J. Ellis, P. Kant, N. E. Mavromatos, *et al.*, Mod. Phys. Lett. A **13**, 303 (1998).
7. J. Ellis, N. E. Mavromatos, and D. V. Nanopoulos, CERN-2000-136; gr-qc/0005100 (2000a).
8. J. Ellis, K. Farakos, N. E. Mavromatos, *et al.*, Astrophys. J. **535**, 139 (2000b).
9. K. Hagiwara, K. Hikasa, K. Nakamura, *et al.*, Phys. Rev. D **66**, 010001-1 (2002).
10. S. Hawking, D. N. Page, and C. N. Pope, Nucl. Phys. B **170**, 283 (1980).
11. D. Huterer and M. S. Turner, Phys. Rev. D **60**, 081301 (1999).
12. J. Kujat, A. M. Linn, R. J. Scherrer, and D. H. Weinberg, astro-ph/0112221 (2001).
13. D. Q. Lamb and D. E. Reichart, Astrophys. J. **536**, 1 (2000).
14. T. Nakamura and T. Chiba, Mon. Not. R. Astron. Soc. **306**, 696 (1999).
15. D. V. Nanopoulos, Yad. Fiz. **63**, 1163 (2000) [Phys. At. Nucl. **63**, 1088 (2000)].
16. OSSE Collaboration, Gamma Ray bursts time profiles (1999); http://www.astro.nwu.edu/astro/OSSE/bursts/.
17. W. S. Paciesas, C. A. Melgan, G. N. Pendleton, *et al.*, Astrophys. J., Suppl. Ser. **122**, 465 (1999).
18. P. Peebles and B. Ratra, astro-ph/0207347 (2002).

19. V. A. Rubakov, Usp. Fiz. Nauk **171**, 913 (2001) [Phys. Usp. **44**, 871 (2001)].
20. V. Sahni and A. A. Starobinsky, Int. J. Mod. Phys. D **9**, 373 (2000).
21. T. D. Saini, S. Raichaudhury, V. Sahni, and A. A. Starobinsky, Phys. Rev. Lett. **85**, 1162 (2000).
22. A. A. Starobinsky, Pis'ma Zh. Éksp. Teor. Fiz. **68**, 721 (1998) [JETP Lett. **68**, 757 (1998)].
23. F. W. Stecker and S. L. Glashow, Astropart. Phys. **16**, 97 (2001).
24. E. G. Vertogradova and Yu. S. Grishkan, Astron. Zh. **77**, 1 (2000) [Astron. Rep. **44**, 142 (2000)].
25. X. Wang, M. Tegmark, and M. Zaldiaga, astro-ph/0105091 (2001).
26. J. Weller and A. Albrecht, astro-ph/0106079 (2001).

Translated by V. Astakhov

Astronomy Letters, Vol. 29, No. 2, 2003, pp. 70–76. Translated from Pis'ma v Astronomicheskiĭ Zhurnal, Vol. 29, No. 2, 2003, pp. 88–94.

Density Distribution in Massive Galactic Disks with a Central Black Hole

N. R. Sibgatullin[1,2*], A. Garcia[1], and V. S. Manko[1]

[1] *Center for Modern Research, National Polytechnical Institute (CINVESTAV–IPN), Mexico*

[2] *Moscow State University, Vorob'evy gory, Moscow, 119899 Russia*

Received August 14, 2002

Abstract—We developed an efficient method for determining the surface-density distribution in a self-gravitating disk with an isolated central point mass from a specified angular-velocity distribution in the disk. An upper limit for the galactic-disk mass is shown to exist at a given black-hole mass. This limit significantly depends on the choice of rotation curves. © *2003 MAIK "Nauka/Interperiodica".*

Key words: *galactic disks, rotation curve, black holes.*

INTRODUCTION

Supermassive black holes (BHs) in the nuclei of galaxies and quasars can provide a high luminosity of these objects through disk accretion (Lynden-Bell 1969). At present, there are strong arguments for this hypothesis for a number of disk galaxies (Rees 1998; for a discussion of the observational data suggesting the presence of compact nuclei in spiral galaxies, see Rubin and Graham 1987, Sofue 1996, Ratnam and Salucci, 2000). Therefore, determining the BH mass and the disk density distribution from a specified particle angular-velocity distribution in the galactic disk is of considerable astrophysical interest. The rotation curves are generally constructed from Doppler measurements of the 21-cm, Hα, and other lines (see Schmidt 1957; de Vaucouleurs 1959; Burbidge *et al.* 1960; Rubin *et al.* 1980; Carignan and Freeman 1985; Persic and Salucci, 1988; Sofue and Rubin, 2001). Burbidge *et al.* (1960), Brandt (1960), Brandt and Belton (1962), Toomre (1963), and Binney and Tremaine (1987) discussed the mathematical problem of restoring the mass surface density from the rotation curves in infinite disks (which model disk galaxies) in connection with the problem of dark mass. Mestel (1963) suggested a model of disk galaxies as self-gravitating disks of finite radius with a constant angular or linear velocity.

Another important physical aspect of the problem (which is not discussed here) is related to the formation of the massive outer parts of accretion disks in which the attraction to the disk, because of its mass, is larger than or of the order of the vertical attractive force from the BH. In this case, the outer part of the accretion disk considerably swells and the disk field plays a significant role in the thermal balance, in the pressure distribution, etc. (Paczyński 1978; Kozlowski *et al.* 1979; Kolykhalov and Sunyaev 1980). The accretion-disk mass over several million years of accretion can reach 0.001 of the BH mass through the outflow of angular momentum into the outer part of the accretion disk (Kolykhalov and Sunyaev 1980).

Here, we ignore the mass of the accretion disk around the BH and take into account only the gravitational field of the galactic disk itself. In the latter, we disregard the viscosity, pressure, and all deviations from purely rotational motion, as was done in classical papers (Schmidt 1957; Burbidge *et al.* 1960; Brandt 1960). Because of the low relative velocity dispersion, we emphasize that the gravitational fields of the dark matter and the bulge component affect the rotation curves in the same way as does the luminous galactic disk itself. Phenomenological expressions for these potentials are given in the monograph of Binney and Tremaine (1987, p. 42) and in Lovelace *et al.* (1999), although some of the authors are skeptical about the methods of separating these fields (Burstein and Rubin, 1985; Persic and Salucci, 1988).

Here, our goal is to discuss a new problem in the theory of the Newtonian potential for the gravitational field of a disk that extends to a certain distance from a central point mass.[1] The rotation curve in the disk is specified and the mass of the central object and the surface density distribution in the disk are required to be determined. The solution of the problem is represented as the two sequential quadratures (20), (21)

[*] E-mail: sibgatullin@fis.cinvestav.mx

[1] Note that disks with an isolated central body cannot be obtained by passing to the limit from confocal spheroidal shells, as was done in previous studies.

1063-7737/03/2902-0070$24.00

and formulas (19), (23) for the BH and disk masses, respectively. As an illustration of applying the general formulas, we provide a broad family of angular-velocity distributions and show a strong dependence of the upper limit for the disk mass on the choice of a family of rotation curves. Despite a number of strong assumptions (disregarding the bulge component; extrapolating the data on the circular motion of material to the outer parts of galactic disks where there is no emitting gas), our statement can be considered as a possible approach to solving the problem of hidden mass in galactic disks with a central black hole.

THE METHOD

In the axisymmetric case, the gravitational field of a thin infinite disk with a central body of mass M can be described by the Newtonian potential (in cylindrical coordinates ρ and z)

$$\phi(\rho,z) = 2G\int_0^\pi\int_a^\infty \frac{\sigma(\rho_0)\rho_0 \mathrm{d}\rho_0\mathrm{d}\varphi}{\sqrt{\rho^2+\rho_0^2-2\rho\rho_0\cos\varphi+z^2}} + \frac{GM}{r}, \qquad r=\sqrt{\rho^2+z^2}, \tag{1}$$

where G is the Newtonian gravitational constant. The disk matter is distributed in the $z=0$ plane outside the circumference of radius a. As follows from the condition of equilibrium between the gravitational and centrifugal forces,

$$\omega^2\rho + \left.\frac{\partial\phi}{\partial\rho}\right|_{z\to 0} = 0 \tag{2}$$

(here, we do not consider other forces such as the gas and radiation pressures).

Substituting potential (1) into Eq. (2), we easily obtain an integral equation with a singular kernel at $\rho=\rho_0$:

$$G\int_a^\infty \sigma(\rho_0)K(\rho,\rho_0)\mathrm{d}\rho_0 = \omega^2\rho - \frac{GM}{\rho^2}, \tag{3}$$

where

$$\frac{\rho}{2\rho_0}K(\rho,\rho_0) = \frac{\mathrm{sign}(\rho-\rho_0)E(\tau)}{\rho+\rho_0} + \frac{K(\tau)}{|\rho-\rho_0|}, \quad \tau = -\frac{4\rho_0\rho}{(\rho-\rho_0)^2}, \tag{4}$$

and $E(\tau)$ and $K(\tau)$ are the complete elliptic integrals.

Equation (3) is a complex singular non-Fredholm integral equation. Even the problem of determining ω from a specified surface density σ is difficult to solve not only analytically but also numerically. At the same time, from the standpoint of observational astronomy, it is much more important to solve the inverse problem, i.e., to determine the σ distribution from a specified ω distribution. This is because σ is difficult to observe in the galactic disk due to the problem of hidden (dark) mass,[2] whereas the rotation curves provide information on the periods of rotation around the galactic center (Schmidt 1957; Burbidge *et al.* 1960; Binney and Tremaine 1987) through the total gravitational field. In this statement (determining σ from ω), solving Eq. (3) appears hopeless even by using numerical methods.

To circumvent the problem of solving this complex equation, instead of (1), we chose ϕ in the form

$$\phi(\rho,z) = \frac{1}{2\pi^2}\int_0^\pi \mathrm{d}\theta\int_a^\infty \ln[(s-\rho\cos\theta)^2 + z^2]\alpha(s)\mathrm{d}s + \frac{GM}{r}, \tag{5}$$

where the real function $\alpha(s)$ has the meaning of source density.

This potential satisfies the Laplace equation everywhere, except the $z=0$ plane, with the disk sources being distributed outside the circle $\rho<a$. A major advantage of this representation over formula (1) is the possibility of using the powerful apparatus of analytic functions on the complex plane in the problem under consideration, because the first term on the right-hand side of Eq. (5) can be represented as $\int_0^\pi f(z+\mathrm{i}\rho\cos\theta)\mathrm{d}\theta$.

Let us show that

$$\left.\frac{\partial\phi}{\partial z}\right|_{z\to+0} = \begin{cases} 0, & 0<\rho<a \\ \dfrac{1}{\pi}\displaystyle\int_a^\rho \frac{\alpha(s_0)\mathrm{d}s_0}{\sqrt{\rho^2-s_0^2}}, & a\le\rho. \end{cases} \tag{6}$$

Indeed, we have from (5)

$$\frac{\partial\phi}{\partial z} = \frac{1}{2\pi^2}\int_0^\pi \mathrm{d}\theta\int_a^\infty \left(\frac{-\mathrm{i}}{s-\rho\cos\theta-\mathrm{i}z} + \frac{\mathrm{i}}{s-\rho\cos\theta+\mathrm{i}z}\right)\alpha(s)\mathrm{d}s - \frac{GMz}{r^3}. \tag{7}$$

Letting z tend to $+0$ for $\rho\cos\theta = s_0 > a$ and using the Sokhotskii–Plemel formula for Cauchy-type in-

[2] In practice, the density is generally restored from photometric data (Freeman 1970; for a critical discussion of this approach, see Burstein and Rubin 1985, Persic *et al.*, 1996.)

tegrals[3]

$$\lim_{Z\to s_0}\int\limits_{\mathcal{L}}\frac{\alpha(s)\mathrm{d}s}{s-Z}=\fint\limits_{\mathcal{L}}\frac{\alpha(s)\mathrm{d}s}{s-Z}\pm\pi\mathrm{i}\alpha(s_0),\qquad(8)$$

we obtain (in our case, $Z=s_0\pm\mathrm{i}z$)

$$\left.\frac{\partial\phi}{\partial z}\right|_{z\to+0}=\begin{cases}0, & 0<s_0<a\\ \dfrac{1}{\pi}\displaystyle\int\limits_0^{\pi}\alpha(s_0)\mathrm{d}\theta, & s_0\ge a.\end{cases}\qquad(9)$$

Formula (6) immediately follows from (9).

Consider now the dependence of ϕ on ρ for $\rho>a$ and $z\to 0$. We obtain from (8)

$$\left.\frac{\partial\phi}{\partial\rho}\right|_{z\to0}=-\frac{GM}{\rho^2}+\frac{1}{\pi\rho}\left(\int\limits_a^{\infty}\alpha(s)\mathrm{d}s\right.\qquad(10)$$
$$\left.-\frac{1}{\pi}\int\limits_a^{\infty}\alpha(s)s\mathrm{d}s\fint\limits_{-\rho}^{\rho}\frac{\mathrm{d}\rho'}{(s-\rho')\sqrt{\rho^2-\rho'^2}}\right).$$

Using now the formula

$$\frac{1}{\pi}\fint\limits_{-\rho}^{\rho}\frac{\mathrm{d}\rho'}{(s-\rho')\sqrt{\rho^2-\rho'^2}}=\begin{cases}0, & a<s<\rho\\ \dfrac{1}{\sqrt{s^2-\rho^2}}, & s>\rho,\end{cases}\qquad(11)$$

we rewrite Eq. (10) as

$$\left.\frac{\partial\phi}{\partial\rho}\right|_{z\to0}=-\frac{GM}{\rho^2}+\frac{1}{\pi\rho}\qquad(12)$$
$$\times\left(\int\limits_a^{\infty}\alpha(s)\mathrm{d}s-\int\limits_{\rho}^{\infty}\frac{\alpha(s)s\mathrm{d}s}{\sqrt{s^2-\rho^2}}\right).$$

Let us show that if the disk mass is finite, then the integral $\int_a^{\infty}\alpha(s)\mathrm{d}s$ becomes zero. Indeed, we have for $\rho\ge a$ from (6)

$$-4\pi G\sigma(\rho)=\left[\frac{\partial\phi}{\partial z}\right]=2\left.\frac{\partial\phi}{\partial z}\right|_{z\to+0}\qquad(13)$$
$$=\frac{2}{\pi}\int\limits_a^{\rho}\frac{\alpha(s_0)\mathrm{d}s_0}{\sqrt{\rho^2-s_0^2}};$$

hence, the disk mass is

$$M_{\mathrm{d}}=-\frac{1}{4\pi G}\int\limits_0^{2\pi}\mathrm{d}\varphi\int\limits_a^{\infty}\left[\frac{\partial\phi}{\partial z}\right]\rho\mathrm{d}\rho=-\frac{1}{G}\int\limits_a^{\infty}m(\rho)\mathrm{d}\rho,\qquad(14)$$

$$m(\rho)=\frac{1}{\pi}\int\limits_a^{\rho}\frac{\alpha(s_0)\rho\mathrm{d}s_0}{\sqrt{\rho^2-s_0^2}}.$$

For M_{d} to be finite, it is necessary that

$$\lim_{\rho\to\infty}m(\rho)=0\quad\Rightarrow\quad\int\limits_a^{\infty}\alpha(s)\mathrm{d}s=0.\qquad(15)$$

Substituting now (12) into the equilibrium condition (2) yields

$$\omega^2\rho-\frac{GM}{\rho^2}=\frac{1}{\pi\rho}\int\limits_{\rho}^{\infty}\frac{\alpha(s)s\mathrm{d}s}{\sqrt{s^2-\rho^2}}.\qquad(16)$$

After introducing the new variables $t=a^2/s^2$ and $x=a^2/\rho^2$, the latter equation reduces to the Abelian integral equation

$$\frac{a^2}{2\pi}\int\limits_0^{x}\frac{\alpha(t)\mathrm{d}t}{t^{3/2}\sqrt{x-t}}=\frac{a^3\omega^2}{x^{3/2}}-GM,\qquad(17)$$

and the standard formula for the solution of this equation gives (see, e.g., Sneddon 1956, p. 318)

$$\frac{a^2\alpha(x)}{2x^{3/2}}=\frac{\mathrm{d}}{\mathrm{d}x}\int\limits_0^{x}\frac{\mathrm{d}t}{\sqrt{x-t}}\left(\frac{a^3\omega^2}{t^{3/2}}-GM\right).\qquad(18)$$

After substituting (18) into condition (15), we derive a formula for the mass of the central body:

$$M=\frac{a^3}{2G}\int\limits_0^{1}\frac{\omega^2\mathrm{d}t}{t^{3/2}\sqrt{1-t}};\qquad(19)$$

i.e., the function $\alpha(x)$ is expressed only in terms of the known angular-velocity distribution:

$$\frac{\alpha(x)}{2ax^{3/2}}=\frac{\mathrm{d}}{\mathrm{d}x}\int\limits_0^{x}\frac{\omega^2\mathrm{d}t}{t^{3/2}\sqrt{x-t}}\qquad(20)$$
$$-\frac{1}{2\sqrt{x}}\int\limits_0^{1}\frac{\omega^2\mathrm{d}t}{t^{3/2}\sqrt{1-t}}.$$

The corresponding surface-density distribution derived from (13) takes the form

$$-4\pi G\sigma(x)=\frac{\sqrt{x}}{\pi}\int\limits_x^{1}\frac{\alpha(t)\mathrm{d}t}{t\sqrt{t-x}}.\qquad(21)$$

[3]Here, s_0 is a point on a smooth contour $\mathcal{L}$: $s_0\in\mathcal{L}$; $Z\to+s_0$ means that the point Z approaches s_0 from the left for the positive tracing of curve $\mathcal{L}$; the symbol $\fint$ denotes a principal-value integral.

It follows from (21) and (20) that the asymptotics of the surface density near the inner disk edge $\rho = a$ is given by

$$-4\pi^2 G\sigma(x) \approx A\sqrt{1-x}, \qquad A = a\int\limits_0^1 \qquad (22)$$
$$\times\left[\left(\frac{\omega^2}{t^{3/2}}\right)_{,t} - \frac{1}{2}\left(\frac{\omega^2}{t^{3/2}} - \frac{G(M+M_d)}{a^3}\right)\right]\frac{\mathrm{d}t}{\sqrt{1-t}}.$$

As follows from formulas (22), in the presence of a finite-mass central body, the surface density near the inner disk edge has no finite limit for $a \to 0$. The inequality $A \le 0$ imposes a physical constraint on the angular-velocity distribution.

Thus, we were able to express the density distribution in the disk only in terms of the presumably known angular-velocity distribution by using two quadratures. The latter can be easily calculated numerically in the general case and analytically for a broad family of special distributions.

The total disk mass, $M_\mathrm{d} = 2\pi\int\limits_a^\infty \sigma\rho\mathrm{d}\rho$, can be determined from formulas (18) and (21):

$$GM_\mathrm{d} = \lim_{t\to 0}\frac{a^2\alpha(t)}{2t} = \lim_{t\to 0}\frac{a^3\omega^2}{t^{3/2}} - GM. \qquad (23)$$

To analytically illustrate our results, consider a smooth angular-velocity distribution with Keplerian asymptotics of the form[4]

$$\omega^2\rho^3 = a_0 + a_2\frac{a^2}{\rho^2} + a_3\frac{a^3}{\rho^3} + \ldots + a_n\frac{a^n}{\rho^n} \qquad (24)$$
$$\equiv a_0 + \sum_{k=2}^{n} a_k t^{k/2}$$

(a_k are constant coefficients).

Substituting this expression into (18) yields

$$\frac{\alpha(x)}{x^{3/2}} = \frac{2}{\sqrt{x}}(a_0 - GM) \qquad (25)$$
$$+\sum_{k=2}^{n}(k+1)x^{(k-1)/2}B\left(\frac{1}{2}, 1+\frac{k}{2}\right)a_k,$$

where $B(x,y)$ is the Euler beta function.

We obtain a formula for the BH mass from condition (19):

$$2GM = 2a_0 + \sum_{k=2}^{n} B\left(\frac{1}{2}, 1+\frac{k}{2}\right)a_k. \qquad (26)$$

[4]The coefficient a_1 in (24) is equal to zero in view of Eqs. (17) and (18).

Substituting (25) into (21) gives

$$-4\pi^2 G\frac{\sigma(x)}{\sqrt{x}} = 4(a_0 - GM)\sqrt{1-x} \qquad (27)$$
$$+\sum_{k=2}^{n}(k+1)B\left(\frac{1}{2}, 1+\frac{k}{2}\right)a_k J_k,$$
$$J_k \equiv \int\limits_x^1 \frac{t^{k/2}\mathrm{d}t}{\sqrt{t-x}}.$$

Using integration by parts for the integrals J_k, we can easily derive the recurrence formula

$$(k+1)J_k = 2\sqrt{1-x} + kxJ_{k-2}. \qquad (28)$$

Its use in (27) gives an explicit expression for the surface density:

$$\sigma(x) = -\frac{x^{3/2}\sqrt{1-x}}{2\pi^2 G}\sum_{k=2}^{n} B\left(\frac{1}{2}, 1+\frac{k}{2}\right)a_k \qquad (29)$$
$$\times\left\{\frac{k}{k-1} + x\frac{k(k-2)}{(k-1)(k-3)} + \ldots + x^{[k/2]-1}\right.$$
$$\times\frac{k(k-2)\ldots(k-2[k/2]+2)}{(k-1)(k-3)(k-2[k/2]+1)}$$
$$\left.\times\left(1 + \frac{(k-2[k/2])x}{\sqrt{1-x}}\ln\frac{1+\sqrt{1-x}}{\sqrt{x}}\right)\right\}.$$

The inequality $A \le 0$ [(see (22)] imposes the following condition on the range parameters a_k:

$$\sum_{k=2}^{n} a_k\left[\frac{k}{2}B\left(\frac{1}{2}, \frac{k}{2}\right) - \frac{1}{2}B\left(\frac{1}{2}, 1+\frac{k}{2}\right)\right] \le 0. \qquad (30)$$

If the function $\omega^2\rho^3$ can be represented as a polynomial in inverse powers of ρ^2, $a_{2k+1} = 0, k = 1, 2, \ldots, N$, then the surface density is given by

$$\sigma(x) = \frac{x^{3/2}\sqrt{1-x}}{\pi^2 a^2 G}\sum_{s=1}^{N}\beta_s x^{s-1}, \qquad (31)$$
$$\beta_s = \sum_{k=s}^{N}\sum_{m=0}^{s}$$
$$\times\frac{2^k(k!)^2(-1)^{m+1}a_{2k}}{(2k-1)!!m!(k-s)!(s-m)!(2k+2m-2s+1)}.$$

EXAMPLES

(A) Consider the case where the rotation curves belong to the family of curves with Keplerian asymptotics of the form

$$\omega^2\rho^3 = GM + GM_\mathrm{d}(1 + b_1 x + b_2 x^2 + b_3 x^3), \quad (32)$$
$$a_i = GM_\mathrm{d}b_{2i}, \qquad x = a^2/\rho^2.$$

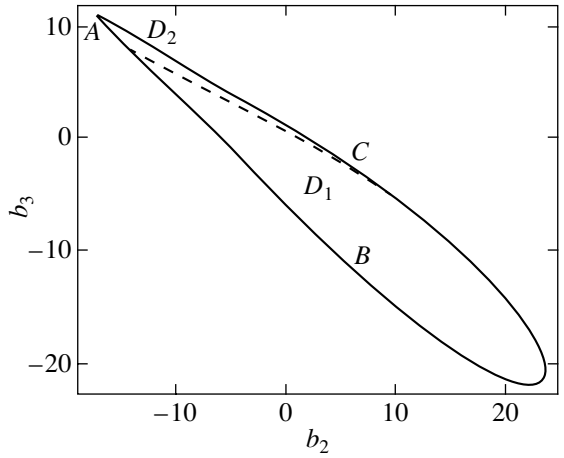

Fig. 1. The domain of positive $\sigma(\rho)$ on the (b_2, b_3) plane.

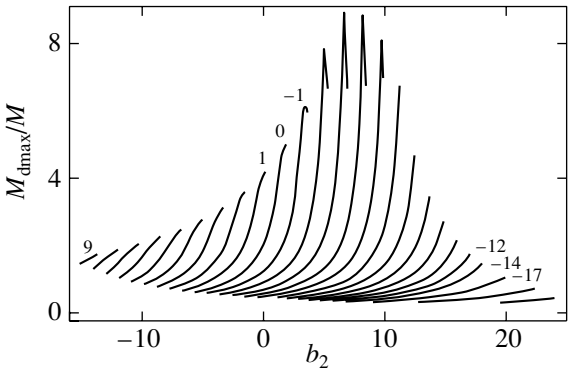

Fig. 2. M_{dmax}/M versus b_2 for various fixed b_3 ($b_3 = -21, -17, -14, -12, \ldots, -1, 0, 1, \ldots, 9$).

It follows from formula (26) that

$$b_1 = -\frac{3}{2} - \frac{4}{5}b_2 - \frac{24}{35}b_3. \qquad (33)$$

Using (33), we obtain the corresponding sought-for surface-density distribution from (31):

$$\sigma(\rho) = \frac{aM_{\mathrm{d}}\sqrt{1-a^2/\rho^2}}{\rho^3}\left[2 + \frac{16}{45}b_2 + \frac{64}{175}b_3 - \left(\frac{64}{45}b_2 + \frac{128}{175}b_3\right)x - \frac{256}{175}b_3x^2\right]. \qquad (34)$$

Formulas (32)–(34) describe the two-parameter family of angular-velocity distributions and of the corresponding surface-density distributions. Figure 1 shows the domain D on the (b_2, b_3) plane in which the right-hand side of (34) is positive and, hence, formula (34) has a physical meaning. The boundary of domain D consists of the following: (i) segments AB and AC tangent to the ellipse at points B and C (their equations are $1 + \frac{8}{45}b_2 + \frac{32}{175}b_3 = 0$, $1 - \frac{8}{15}b_2 - \frac{32}{35}b_3 = 0$);[5] (ii) the part of the ellipse between the points of contact whose equation can be obtained by setting the discriminant of the quadratic trinomial in the parentheses of the right-hand side of (34) equal to zero.

Denote the minimum value of the cubic polynomial $f(x)$ by $\mu(b_2, b_3)$:

$$f(x) \equiv 1 - \left(\frac{3}{2} + \frac{4}{5}b_2 + \frac{24}{35}b_3\right)x + b_2x^2 + b_3x^3 \qquad (35)$$

on segment $(0, 1]$. The maximum possible disk mass can then be calculated by using the condition that the right-hand side of (32) be nonnegative:

$$M_{\mathrm{dmax}}(b_2, b_3) = -M/\mu(b_2, b_3). \qquad (36)$$

The polynomial $f(x)$ can take on its minimum value either inside interval $(0, 1)$ or at its boundary $x = 1$. In Fig. 1, the dashed line separates domain D into two parts, D_1 and D_2. Inside D_1, in which $f(1)$ is the minimum value of $f(x)$ on interval $(0, 1)$, the function $\mu(b_2, b_3)$ has a simple form: $\mu = -\frac{1}{2} + \frac{1}{5}b_2 + \frac{11}{35}b_3$.

In Fig. 2, M_{dmax} is plotted against b_2 for fixed b_3. In this case, the points (b_2, b_3) belong to D. It follows from our analysis that the maximum possible disk mass can reach $9M$. The more complex is the angular-velocity distribution in the disk [i.e., the larger is n in polynomial (31)], the more massive can be the disk in principle: the maximum disk mass is $5M$ for the one-parameter family of angular-velocity distributions and increases to $9M$ for the two-parameter family.

Consider three special cases of distribution (32).

(1) The simplest special case, $b_2 = b_3 = 0$, was found by Lemos and Letelier (1994).[6] In this case,

$$\omega^2\rho^3 = GM + GM_{\mathrm{d}}\left(1 - \frac{3}{2}\frac{a^2}{\rho^2}\right), \qquad (37)$$

$$\sigma(\rho) = \frac{2aM_{\mathrm{d}}\sqrt{\rho^2 - a^2}}{\pi^2\rho^4}.$$

It follows from (35) and (36) that the disk mass cannot exceed two masses of the central body.

[5] The inequality $A \le 0$ is equivalent to the condition $1 - \frac{8}{15}b_2 - \frac{32}{35}b_3 \ge 0$.

[6] See Semerák and Žaček (2000) for analysis of the corresponding gravitational potential.

(2) The special case $b_2 = 15/8$, $b_3 = 0$ corresponds to the angular-velocity and surface-density distributions

$$\omega^2\rho^3 = GM + GM_{\rm d}\left(1 - 3\frac{a^2}{\rho^2} + \frac{15}{8}\frac{a^4}{\rho^4}\right); \quad (38)$$

$$\sigma(\rho) = \frac{8aM_{\rm d}(\rho^2 - a^2)^{3/2}}{3\pi^2\rho^6},$$

the disk mass cannot exceed $5M$.

(3) Choosing $b_2 = 45/8$ and $b_3 = -35/16$ gives

$$\omega^2\rho^3 = GM + GM_d\left(1 - \frac{9}{2}\frac{a^2}{\rho^2} + \frac{45}{8}\frac{a^4}{\rho^4} - \frac{35}{16}\frac{a^6}{\rho^6}\right), \quad (39)$$

$$\sigma(\rho) = \frac{16aM_d}{5\pi^2\rho^3}\left(1 - \frac{a^2}{\rho^2}\right)^{5/2},$$

and the disk mass cannot be larger than $6.69M$.

(B) To show that the galactic-disk mass can be arbitrarily large compared to the central BH mass, consider the rotation curves[7]

$$\omega^2(\rho^2 + c^2)^{3/2} = G(M + M_d), \quad c = \text{const}. \quad (40)$$

In this case, Eq. (23) holds automatically. Denote the parameter c^2/a^2 by b.

Calculating $\alpha(x)$ from formula (20), we obtain

$$\frac{\alpha(x)}{2ax^{3/2}} = -\frac{b(-1 + (3 + b) + bx^2)}{\sqrt{x}(1 + b)(bx + 1)^2}\frac{G(M + M_{\rm d})}{a^3}. \quad (41)$$

Substituting expression (41) into (21) yields a formula for the surface-density distribution:

$$\sigma(x) = \frac{(M + M_{\rm d})\sqrt{bx^3}}{\pi^2 a^2} \quad (42)$$

$$\times\left(\frac{\sqrt{b(1-x)}}{(1+b)(1+bx)} + \frac{\arctan\sqrt{b(1-x)/(1+bx)}}{(1+bx)^{3/2}}\right).$$

An unexpectedly simple formula for the disk mass follows from formula (19):

$$M_{\rm d} = bM. \quad (43)$$

The parameter b in formulas (41)–(43) can be an arbitrary positive number. Therefore, the galactic-disk mass (if the linear velocity $V = \rho\omega$ reaches its maximum at distances much larger than the accretion part of the disk, $b \gg 1$) can exceed the BH mass by many times. For $a \to 0$, the variable x also tends to zero, while b tends to infinity. It follows from formula (43) that $M \to 0$; the Toomre–Kuzmin result for the surface-density distribution that corresponds to the rotation curve (40) follows from formula (42):

$$\sigma(\rho) = \frac{cM_d}{2\pi(\rho^2 + c^2)^{3/2}}. \quad (44)$$

[7] The rotation curves (40) were first considered by Kyz'min (1956); they belong to the family of curves with Keplerian asymptotics for $\rho \to \infty$ proposed by Brandt (1960) for infinite disks without a central black hole as a special case.

CONCLUSIONS

Thus, we were able to solve the problem of determining the surface density in massive galactic disks with an isolated central black hole from specified rotation curves. The problem was reduced to determining the two sequential quadratures (20) and (21), which can be easily calculated numerically in the most general case of smooth angular-velocity distributions. We also showed how the masses of the central body and the galactic disk can be calculated if the rotation curve is known.

Analysis of our formulas leads us to the following two general conclusions:

(1) In each case, the mass of the galactic disk around the central body must be smaller than a certain upper limit, which depends on the concentration of matter near the inner disk boundary. The disk mass strongly depends on the shape of the rotation curve and can in principle exceed the BH mass by many times.

(2) For an arbitrary nondegenerate smooth angular-velocity distribution in the disk, the surface density at the inner boundary tends to zero as $\sqrt{1 - a^2\rho^{-2}}$. This corresponds to a parabolic disk-thickness profile for a finite volume density at the inner boundary. At infinity, the surface density decreases as ρ^{-3}.

In conclusion, note that the method developed here is not restricted only to the case of infinite massive disks with an attractive central body but it also allows finite disks and ring systems to be considered. The latter problems are being analyzed and developed and will become the subject of future publications.

ACKNOWLEDGMENTS

We wish to thank the referee and Prof. A. Toomre for helpful remarks. This study was supported by the COnaCyt projects 34222-E and 38495-E and by the Catedra Patrimonial SnI–COnaCyt Program (Mexico).

REFERENCES

1. J. Binney and S. Tremaine, *Galactic Dynamics* (Princeton Univ. Press, Princeton, 1987).
2. J. C. Brandt, Astrophys. J. **131**, 293 (1960).
3. J. C. Brandt and M. J. S. Belton, Astrophys. J. **136**, 352 (1962).
4. E. M. Burbidge, G. R. Burbidge, and K. H. Prendergast, Astrophys. J. **131**, 282 (1960).
5. D. Burstein and V. C. Rubin, Astrophys. J. **297**, 423 (1985).
6. C. Carignan and K. C. Freeman, Astrophys. J. **294**, 494 (1985).
7. K. C. Freeman, Astrophys. J. **160**, 811 (1970).
8. P. I. Kolykhalov and R. A. Sunyaev, Pis'ma Astron. Zh. **6**, 680 (1980) [Sov. Astron. Lett. **6**, 357 (1980)].
9. M. Kozlowski, P. J. Wiita, and B. Paczyński, Acta Astron. **29**, 157 (1979).
10. G. G. Kuz'min, Astron. Rep. **33**, 27 (1956).
11. J. P. S. Lemos and P. S. Letelier, Phys. Rev. D **49**, 5135 (1994).
12. R. V. E. Lovelace, L. Zhang, D. A. Kornreich, and M. P. Haynes, Astrophys. J. **524**, 634 (1999).
13. D. Lynden-Bell, Nature **223**, 690 (1969).
14. L. Mestel, Mon. Not. R. Astron. Soc. **126**, 553 (1963).
15. B. Paczyński, Acta Astron. **28**, 91 (1978).
16. M. Persic and P. Salucci, MNRAS **234**, 131 (1988).
17. M. Persic, P. Salucci, and F. Stel, MNRAS **281**, 27 (1996).
18. Ch. Ratnam and P. Salucci, astro-ph/0008121.
19. M. J. Rees, *Black Holes and Relativistic Stars* (Univ. of Chicago Press, Chicago, 1998), p. 79.
20. V. C. Rubin and J. A. Graham, Astrophys. J. **316**, 67 (1987).
21. V. C. Rubin, W. K. Ford, and N. Thonnard, Astrophys. J. **238**, 471 (1980).
22. M. Schmidt, Bull. Astron. Inst. Netherlands **14**, 17 (1957).
23. O. Semerák and M. Žaček, Class. Quantum Grav. **17**, 1613 (2000).
24. I. N. Sneddon, *The Use of Integral Transforms* (McGraw-Hill, New York, 1956).
25. Y. Sofue, Astrophys. J. **458**, 120 (1996).
26. Y. Sofue and V. C. Rubin, Ann. Rev. Astron. Astrophys. **39**, 137 (2001).
27. A. Toomre, Astrophys. J. **138**, 385 (1963).
28. G. de Vaucouleurs, in *Handbuch der Physik* (Springer-Verlag, Berlin, 1959), Vol. 53, p. 348.

Translated by V. Astakhov

Astronomy Letters, Vol. 29, No. 2, 2003, pp. 77–90. Translated from Pis'ma v Astronomicheskiĭ Zhurnal, Vol. 29, No. 2, 2003, pp. 95–110.

Detailed Kinematic Study of the Ionized and Neutral Gas in the Complex of Star Formation in the Galaxy IC 1613

T. A. Lozinskaya[1*], A. V. Moiseev[2], and N. Yu. Podorvanyuk[1]

[1] *Sternberg Astronomical Institute, Universitetskiĭ pr. 13, Moscow, 119992 Russia*

[2] *Special Astrophysical Observatory, Russian Academy of Sciences, Nizhnii Arkhyz, 357147 Karachai-Cherkessian Republic, Russia*

Received August 20, 2002

Abstract—We carried out detailed kinematic studies of the complex of multiple H I and H II shells that represent the only region of ongoing star formation in the dwarf irregular galaxy IC 1613. We investigated the ionized-gas kinematics by using Fabry–Perot Hα observations with the 6-m Special Astrophysical Observatory telescope and the neutral-gas kinematics by using VLA 21-cm radio observations. We identified three extended (300–350 pc) neutral shells with which the brightest H II shells in the complex of star formation are associated. The neutral-gas kinematics in the complex has been studied for the first time and the H I shells were found to expand at a velocity of 15–18 km s^{-1}. We constructed velocity ellipses for all H II shells in the complex and refined (increased) the expansion velocities of most of them. The nature of the interacting ionized and neutral shells is discussed. © *2003 MAIK "Nauka/Interperiodica"*.

Key words: *galaxy IC 1613, star formation, gas kinematics*.

1. INTRODUCTION

The giant complex of multiple ionized shells (Meaburn *et al.* 1988) in the northeastern sector of IC 1613 is the most prominent structure in narrow-band images of this Local-Group dwarf irregular galaxy located at a distance of 725–730 kpc (Freedman 1988a, 1988b; Dolphin *et al.* 2001) in the Hα, [O III], and [S II] lines.

Most of the bright H II regions (Sandage 1971; Lequeux *et al.* 1987; Hodge *et al.* 1990; Price *et al.* 1990; Hunter *et al.* 1993; Valdez-Gutierrez *et al.* 2001) and the only known supernova remnant in the galaxy [Lozinskaya *et al.* (1998) and references therein] belong to this complex.

The stellar population of the complex is represented by some twenty young stellar associations and clusters (Hodge 1978; Georgiev *et al.* 1999; and references therein).

This multishell complex and the rich stellar grouping represent the only site of ongoing star formation in the galaxy. This region of violent star formation in IC 1613 can probably be considered as a very young and small superassociation (Lozinskaya 2003).

Recent 21-cm radio observations of the complex have shown that extended neutral shells (supershells in standard terminology) are associated with multiple ionized shells (Lozinskaya *et al.* 2001, 2002; Lozinskaya 2002).

The ionized-gas velocities in the region were first measured by Meaburn *et al.* (1988); five spectrograms for the bright part of the complex with poor spatial coverage were used to determine the characteristic expansion velocities of the H II shells, ~30 km s^{-1}. Valdez-Gutierrez *et al.* (2001) constructed the ionized-gas radial-velocity field in the Hα and [S II] lines and estimated the shell expansion velocities from the splitting of the line profile integrated over each of the objects.

The H I and H II shells close up and partially overlap in the plane of the sky. If their sizes along the line of sight and in the plane of the sky are assumed to be comparable, then they can be assumed to be in physical contact with one another.[1]

Deep narrow-band Hα images revealed a chain of bright compact emission-line objects at the boundary of the two closing shells in the complex. Spectroscopic observations show that the compact objects are early-type giants and supergiants (Lozinskaya

[*] E-mail: lozinsk@sai.msu.ru

[1] The galaxy is inclined at an angle of 30° to the plane of the sky and the gaseous-disk thickness 500–700 pc, as estimated by Afanasiev *et al.* (2000), is comparable to the size of the multishell complex. Therefore, a chance projection of physically unrelated shells located at different distances is unlikely.

1063-7737/03/2902-0077$24.00

Table 1. A log of IFP observations for IC 1613

Date of observation	IFP type	T_{exp}, s	Seeing
Nov. 1, 2000	IFP235	32×240	$2''.0$
Sep. 12, 2001	IFP501	36×200	$1''.8$

et al. 2002). The characteristic ionized- and neutral-gas morphology suggests that the H I and H II shells physically interact in the region of the stellar chain (see also Section 3).

Thus, the complex of star formation shows evidence of the possible collision between expanding ionized and neutral shells, the interaction of ionized shells with the surrounding H I shells, and the like. This evidence suggests that the birth of new-generation stars triggered by shell collisions is probable here (Chernin and Lozinskaya 2003). That is why a detailed study of the structure and kinematics of the ionized and neutral gas in the multishell complex is of current interest.

The neutral-gas kinematics in the complex of star formation has not yet been investigated.

Our goal is to study in detail the kinematics of the neutral and ionized gas components in the shells that constitute the complex of star formation with high spatial and spectral resolutions.

To study the kinematics of the ionized shells, we carried out Hα observations with a scanning Fabry–Perot interferometer attached to the 6-m Special Astrophysical Observatory (SAO) telescope. The kinematics of the neutral shells was studied by using VLA 21-cm radio observations.

The techniques for optical and radio observations and for data reduction are described in Section 2. In Section 3, we use our ionized- and neutral-gas observations to analyze the overall structure of the multishell complex in the plane of the sky. The results of our kinematic study for the H I and H II shells in the complex are presented in Sections 4 and 5, respectively. Our results and conclusions regarding the nature of the multishell complex that follow from them are discussed in Section 6.

2. INTERFEROMETRIC Hα AND 21 cm OBSERVATIONS

Fabry–Perot Observations with the 6-m SAO Telescope and Data Reduction

Interferometric Hα observations were carried out at the prime focus of the 6-m SAO telescope using a scanning Fabry–Perot interferometer (IFP). The interferometer was placed inside the SCORPIO focal reducer, so the equivalent focal ratio was (F/2.9). A brief description of the focal reducer is given on the Internet (http://www.sao.ru/~moisav/scorpio/scorpio.html); the SCORPIO capabilities in IFP observations were also described by Moiseev (2002). The detector was a TK1024 1024×1024-pixel CCD array. The observations were performed with 2×2-pixel hardware averaging to reduce the readout time, so 512×512-pixel images were obtained in each spectral channel. The field of view was $4'.8$ for a scale of $0''.56$ per pixel. An interference filter with FWHM = 15 Å centered on the Hα line was used for premonochromatization.

A log of IFP observations is given in Table 1. For our observations, we used two different Queensgate ET-50 interferometers operating in the 235th and 501st orders of interference at the Hα wavelength (designated in Table 1 as IFP235 and IFP501, respectively). IFP235 provided a spectral resolution of FWHM $\approx$ 2.5 Å near the Hα line (or $\sim$110 km s^{-1}). The separation between neighboring orders of interference, $\Delta\lambda = 28$ Å, corresponded to a range of $\sim$1270 km s^{-1} free from order overlapping. The spectral resolution of IFP501 was $\sim$0.8 Å (or $\sim$40 km s^{-1}) for a range of $\Delta\lambda = 13$ Å (or $\sim$590 km s^{-1}) free from order overlapping.

During the exposure, we sequentially took interferograms of the object for various IFP plate spacings. Therefore, the number of spectral channels was 32 and 36 and the size of a single channel was $\delta\lambda \approx$ 0.87 Å ($\sim$40 km s^{-1}) and $\delta\lambda \approx$ 0.36 Å ($\sim$16 km s^{-1}) for IFP235 and IFP501, respectively.

We reduced our interferometric observations by using the software developed at the SAO (Moiseev 2002). After the primary data reduction, the subtraction of night-sky lines, and wavelength calibration, the observational material represents "data cubes" in which each point in the 512×512-pixel field contains a 32-channel or 36-channel spectrum. We performed optimal data filtering—Gaussian smoothing over the spectral coordinate with FWHM = 1.5 channels and spatial smoothing by a two-dimensional Gaussian with FWHM = 2–3 pixels—by using the ADHOC software package.[2]

The accuracy of the wavelength calibration using the calibration-lamp line was less than 3 km s^{-1}. Our radial-velocity measurements of the night-sky λ6553.617 Å line revealed a systematic shift when measuring the absolute values of the radial velocities: -8 ± 3 km s^{-1} for IFP501 and 15 ± 8 km s^{-1}

[2]The ADHOC software package was developed by J. Boulesteix (Marseilles Observatory) and is publicly available in the Internet.

for IFP235. It should be noted, however, that these values were most likely overestimated, because the sky-line intensity varied during the scanning time.

The bulk of the observational data used here were obtained with IFP501, which provided a higher spectral resolution. Only when analyzing the observational data for the supernova remnant, where the weak line wings were observed at velocities outside the range free from order overlapping for IFP501, did we additionally use observations with IFP235.

Observations in the 21-cm Line and Data Analysis

Based on VLA 21-cm observations, we mapped the H I distribution with a high angular resolution and studied the neutral-gas kinematics in an extended region of the galaxy that included the complex of star formation. An application for the project to study the neutral-gas structure and kinematics in IC 1613 was made by E. Wilcots; the first results were published by Lozinskaya *et al.* (2001).

The data given in Sections 3 and 4 were obtained by combining VLA observations in configurations B, C, and D; the width of a single channel in radial velocity was 2.57 km s^{-1}. We smoothed the data with the Hunning function. The data were calibrated by the standard method and transformed into maps using the AIPS software package.

The reduced data are presented in the form of a data cube with an angular resolution of $7''.4 \times 7''.0$, which corresponds to a linear resolution of $\sim$23 pc.

To map the integrated 21-cm line intensity distribution, we summed only 40 of the 127 possible spectral channels, because no galactic line emission was detected in the remaining channels.

3. THE OVERALL STRUCTURE OF THE COMPLEX OF STAR FORMATION IN THE PLANE OF THE SKY

Figure 1a shows the monochromatic Hα image of the multishell complex obtained by integrating the emission over all spectral channels (in the velocity range from -2 to -584 km s^{-1}) using our interferometric observations with IFP501. The arrows indicate the objects discussed in Section 5: the chain of early-type giants and supergiants mentioned above, the only Of star in the galaxy identified by Lozinskaya *et al.* (2002), the only known supernova remnant—the nebula S8 (Sandage 1971), and the bright H II region no. 40a, b from the list by Hodge *et al.* (1990). Also shown in the figure are the ionized-shell numbers from the list by Valdez-Gutierrez *et al.* (2001). (Below, we use the notation adopted in this paper for uniformity.)

All of the brightest ionized shells in IC 1613 are concentrated in the complex of star formation (Valdez-Gutierrez *et al.* 2001; Lozinskaya *et al.* 2002). In Fig. 1a, these brightest regions are overexposed to show the faintest H II shells. The faint filamentary structures in shells R6, R7, R8, and R3 are clearly seen in the figure; we also managed to detect weak emission from thin filaments in several other regions of the complex.

The chain of bright early-type stars is located at the bright boundary of the ionized shell R1 adjacent to shell R2. This region falls within square N27 in Fig. 3 from Valdez-Gutierrez *et al.* (2001) and includes the nebulae S10 and S13, according to the classification of Sandage (1971). Association no. 17 from the list by Hodge (1978) [its eastern part is designated as no. 25 in the list by Georgiev *et al.* (1999)] also lies here.

Our 21-cm H I observations in IC 1613 with a high angular resolution allow us to compare the H I and H II distributions in the complex of star formation. The results obtained from these observations are presented in Figs. 1b and 2a. Figure 1b shows the 21-cm image of the northwestern galactic sector obtained by integrating the emission over 40 channels in the velocity range from -279 to -178 km s^{-1} (indicated by shades of gray) superimposed on the monochromatic Hα image (indicated by isophotes). The latter is represented only by the brightest regions. The H I intensity distribution in the entire galaxy is shown in Fig. 2a (see Section 4).

Even the first observations by Lake and Skillman (1989) with an angular resolution of $60'' \times 60''$ showed that the complex of ionized shells is localized in the region of the brightest spot on the H I map of IC 1613. The multishell structure of this bright spot is clearly seen in Figs. 1b and 2a: the three most prominent H I shells in the galaxy surround the chain of bright ionized shells. Below, these bright neutral shells are called I, II, and III for definiteness.

The central coordinates, sizes, and expansion velocities of the shells estimated in Section 4 are listed in Table 2. The third column gives the shell sizes along two axes in arcsec (upper row) and the mean radius in pc determined by them (lower row).

The shells identified in the star-forming region are 300–500 pc in size. These sizes fall within the region of the peak in the size distribution of giant H I and H II shells in the LMC and SMC (see Meaburn 1980; Kim *et al.* 1999; Staveley-Smith *et al.* 1997).

In addition to these three brightest and most prominent H I shells, we identified much larger ring-shaped and arc-shaped structures in IC 1613, with sizes up to 1–1.5 kpc, supergiant shells in the terminology of Meaburn (1980). These are clearly

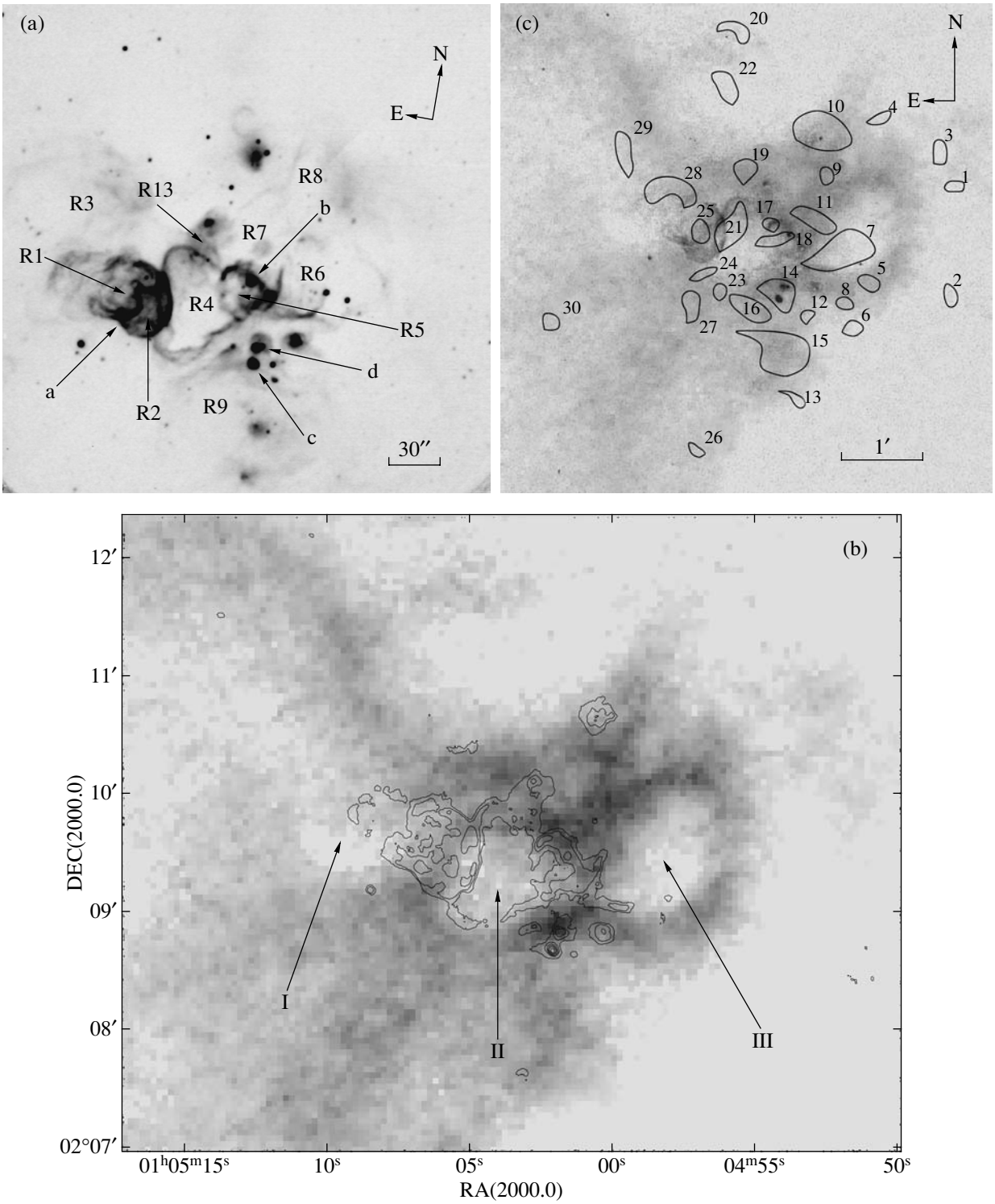

Fig. 1. (a) The monochromatic Hα image of the multishell complex obtained with a Fabry–Perot interferometer on the 6-m SAO telescope. The ionized shells R1–R9 and R13 from the list of Valdez-Guterrez *et al.* (2001) studied here are labeled. The arrows indicate: a—the chain of early-type supergiants at the boundary of shell R1; b—the only Of-type star identified by Lozinskaya *et al.* (2002); c—the only supernova remnant in IC 1613; d—object no. 40a, b from the list of H II regions by Hodge *et al.* (1990). (b) The H I intensity distribution (indicated by shades of gray) superimposed on the monochromatic Hα image of the region (the isophotes corresponding to the brightest regions in Fig. 1a are shown). The Roman numericals I, II, and III mark the three neutral shells investigated here. (c) The boundaries of the OB associations identified by Georgiev *et al.* (1999) superimposed on the intensity distributions in the 21-cm line (indicated by shades of light gray) and in the Hα line (indicated by shades of dark gray) .

Table 2. Parameters of the H I shells in the complex of star formation

Shell	Central coordinates (2000)	Size, arcsec R, pc	V(exp), km s^{-1}	Age, Myr
I	$1^h5^m10^s$	$\sim$97		
	2°9′45″	172		
II	$1^h5^m4^s.5$	73 × 81	12–17	5.6
	2°9′19″	136		
III	$1^h4^m58^s$	73 × 97	16–18	5.3
	2°9′32″	150		

seen in the 21-cm image of the entire galaxy shown in Fig. 2a (see also Section 6).

As follows from Figs. 1a and 1b, a one-to-one correspondence between the neutral and ionized structures in size and localization is observed only in one case: the ionized shell R4 fits well into its surrounding neutral shell II. The remaining bright H II shells are smaller than the neutral shells and are located irregularly: the ionized shell R1 lies within the neutral shell I near its western boundary rather than in the central cavity; R6 lies within shell III near its eastern boundary; the ionized shells R2 and R5 fall on the bars between shells I and II and between shells II and III, respectively. As was shown by Kim *et al.* (1999), the giant H I shells in the LMC are also interrelated differently with H II shells and supershells, which reflects the different evolutionary stages of star formation in the region. This issue is discussed in more detail in Section 6.

The boundary of the ionized shell R1 with the chain of blue giants and supergiants coincides with the thinnest arc-shaped H I bar between the two H I shell structures. The characteristic morphology of the ionized and neutral shells suggests that they are in physical contact: the thin neutral arc adjoins the ionized shell in the region of the stellar chain from the outside and the two shells in this region have the same radius of curvature.

The stellar component of the complex represented by some thirty stellar associations and clusters is superimposed on the Hα and 21 cm images in Fig. 1c. The figure shows the association boundaries that correspond to a new breakdown of the stellar population into separate groups in Georgiev *et al.* (1999). Here, a number of associations from the list by Hodge (1978) were split into several smaller groups.

4. NEUTRAL-GAS KINEMATICS IN THE COMPLEX

The data cube that we constructed from the 21-cm observations allows us to analyze the H I distribution and kinematics in the entire galaxy. The kinematics of the southeastern region of IC 1613 around a WO star was studied previously (Lozinskaya *et al.* 2001). Here, we consider in detail the neutral-gas kinematics in the complex of star formation for the first time.

Our 21-cm observations show that this complex stands out as the dynamically most active region in IC 1613. Velocities of internal neutral-gas motions from $-195\ldots-200$ to $-250\ldots-255$ km s^{-1} are observed in the region of the complex ($\Delta RA = 1^h2^m20^s$–$1^h2^m40^s$, $\Delta D = 1°52'$–$1°55'$) against the background of a smooth systematic variation in the mean H I velocity along the galaxy that was pointed out by Lake and Skillman (1989).

In searching for the possible expansion of the H I shells in the complex, we constructed position–radial velocity diagrams in several bands:

1—in the band that crosses the pair of shells I and II through their centers;

2—in the band that crosses the pair of shells II and III in the same way;

3—in the band that passes through the stellar chain at the boundary of shells I and II;

4, 5, and 6—in the bands that cross each of the three shells I, II, and III, respectively, in the directions perpendicular to scans 1 and 2;

7—in the band that includes scans 15 and 16 in the Hα line (see Section 5) and that passes through the only supernova remnant in IC 1613.

The directions of scans 1–7 on the H I map are shown in Fig. 2a. The position–radial velocity diagrams constructed for these scans are shown in Fig. 2b.

We chose the band width when scanning in such a way that only the central shell region and the two peripheral regions in the direction of each scan fell within this width, which corresponded to 11 pixels or 33″ in the sky.

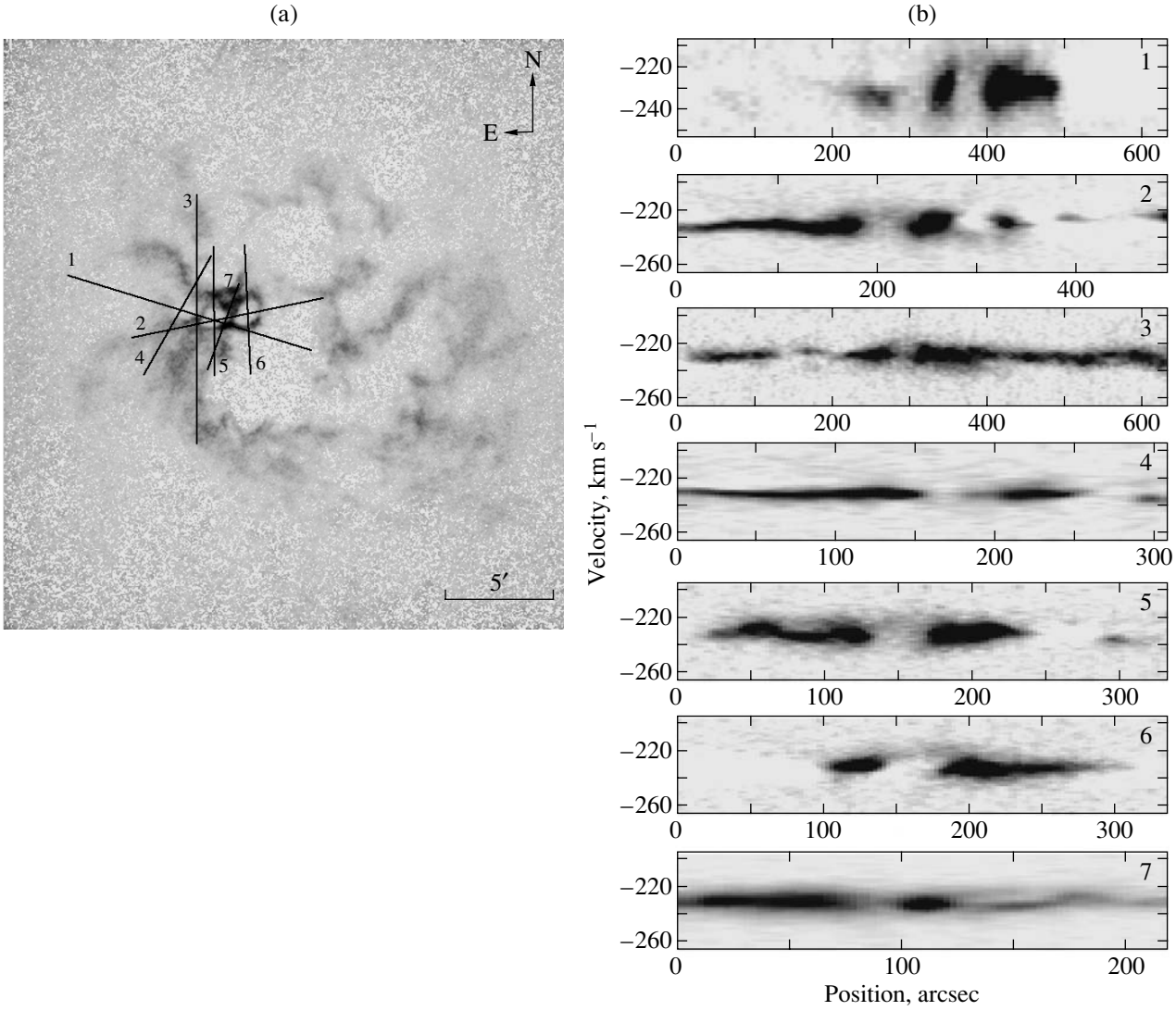

Fig. 2. (a) The localization of scans 1–7 shown in Fig. 2b on the H I map of the galaxy. The numbers are given at the beginning of each scan. (b) The position–H I velocity diagrams for scans 1–7 (the velocity is heliocentric).

The mean H I velocity in the region of the complex that was determined from the emission of "unaccelerated" gas detected on all scans 1–7 outside shells I, II, and III discussed below is $V_{\rm Hel} = -230 \pm 5$ km s^{-1}. This value is in good agreement with the estimate obtained by Lake and Skillman (1989) for this part of the galaxy from low-angular-resolution observations.

Figure 2b shows the radial-velocity variation with distance typical of an expanding shell at least for the two objects denoted by II and III. The characteristic arc-shaped pattern of velocity variation (half of the "velocity ellipse") is seen both on the scans along the pairs of shells I–II and II–III and on the scans that cross each of shells II and III in a perpendicular direction (see Fig. 2b). Evidence of shell-II expansion is seen on scan 1 (370–400 arcsec), scan 2 (180–230 acrsec), and scan 5 (130–170 arcsec). Scan 2 (280–310 arcsec) and scan 6 (140–190 arcsec) exhibit shell-III expansion. In both cases, one side of the expanding shell is clearly seen. The difference between the unaccelerated-gas velocities on the periphery of shell II (from −225 to −230 km s^{-1}) and on its approaching side (from −240 to −242 km s^{-1}) gives an expansion velocity $V(\exp) \sim 12$–17 km s^{-1}. For shell III, we find the expansion velocity from the difference between the unaccelerated-gas velocities on the periphery (from −228 to −230 km s^{-1}) and on the receding side (−212 km s^{-1}) to be $V(\exp) \sim 16$–18 km s^{-1}. The neutral shell I exhibits no distinct expansion.

The inferred expansion velocities of the two H I shells in IC 1613 fall within the region of the peak in

the velocity distribution of neutral supershells in the LMC (Kim *et al.* 1999).

The only supernova remnant in IC 1613 lies at the outer boundary of the densest H I layer in the galaxy that bounds shell II in the south (see Fig. 1). Another, fainter neutral shell in which the supernova remnant is located may adjoin the bright shell II in the south. Scan 7 (120–170 arcsec) shows traces of expansion of this fourth neutral shell. The supernova remnant lies at the inner boundary of this shell (~120 arcsec). This scenario—a supernova explosion inside a cavity surrounded by a dense shell and a collision of the expanding remnant with the shell wall—was suggested by Lozinskaya *et al.* (1998) to explain the peculiarity of this remnant, which combines the properties of young and old objects and which has high optical and X-ray brightnesses.

The region at the boundary between shells I and II where the chain of early-type giants and supergiants is located exhibits high neutral-gas velocities. A deficit of 21-cm brightness is observed in this region on scan 3 (280–310 arcsec). This deficit stems from the fact that emission from only the thin bar between shells I and II is detected here when scanning. However, this weak emission is observed over a wide velocity range, from $\simeq -250$ to $\simeq -210$ km s^{-1} at 20–30% I(max).

Our expansion velocities and the corresponding kinematic ages of the bright neutral shells in the complex of star formation are given in Table 2.

5. IONIZED-GAS KINEMATICS IN THE COMPLEX

To study in detail the kinematics of the ionized shells using our Hα observations with IFP501, we constructed position–radial velocity diagrams for thirty scans, which cover the entire complex of star formation almost uniformly. For each of the chosen directions, we constructed two or three scans of different widths: from 1 to 40 pixels (from 0.5 to 24″). Figure 3a shows the localization of some of these scans. The width of scans 14 and 17 is 21 pixels or 12″; the width of the remaining scans shown in Fig. 3 is 11 pixels or 6″.

The mean velocity of the unshifted feature in the H II emission line in the complex of star formation is from −230 to −240 km s^{-1}. We also observe a smooth velocity variation in the complex between −220 km s^{-1} in the southeast and −260 km s^{-1} in the northwest, in agreement with the results of Valdez-Gutierrez *et al.* (2001).

As was shown in Section 3, the elongated system of the brightest ionized shells, including R1, R2, R4, R5, and R6, is associated with the neutral shells I, II, and III.

Two scans (v1 and v2) cross this chain of bright shells in directions that roughly coincide with scans 1 and 2 over the neutral shells I–II and II–III, respectively (see Section 4).

The two scans clearly show Hα splitting along the entire length of the chain and reveal the characteristic configuration of the velocity ellipse for individual shells and, possibly, for the chain of bright shells as a whole. The typical velocities are about −290 . . . −300 km s^{-1} for the approaching sides of the elongated system of bright shells and about from −190 . . . −200 km s^{-1} for its receding sides. We successively consider all the ionized shells of this system.

Shells R1 and R2 and the Chain of Stars at Their Boundary

Shells R1 and R2 and the region at their boundary where the chain of young stars is located were scanned repeatedly, in different directions, and in bands of different widths. All of the scans passing through the central regions of these shells clearly reveal the characteristic configuration of the velocity ellipse related to their expansion.

The mean velocity of the unperturbed gas at the eastern boundary of shell R1 is −240 km s^{-1}. The local velocity ellipses on scan v2 suggest that the bright western part of shell R1 (45–55 arcsec) expands at a velocity of 50–60 km s^{-1} relative to this unshifted feature: the velocity of the approaching side is −290 km s^{-1}. In shell R2 (55–80 arcsec), the velocities of the bright approaching and faint receding sides are from −280 to −300 and −170 km s^{-1}, respectively. On scan v1 that crosses the same region in a different direction, we see a similar arc structure in region R2 and individual clumps in region R1.

Several scans that cross the system of bright shells in the directions perpendicular to v1 and v2 also clearly reveal an expansion of shells R1 and R2. Scans 3a, 3b, and 4 clearly show that shell R1 expands at a velocity of 60–70 km s^{-1} (up to 100 km s^{-1} in its bright southern part). The bright regions on the shell periphery exhibit the unshifted line component at a velocity of from −230 to −250 km s^{-1}; the velocities of the two sides of the expanding shell are −180 and −320 km s^{-1} (scan 3). Scan 4 also shows that the bright southern part of shell R1 expands faster than does its northern part: the velocity of the approaching side is the same in the entire shell, being about −300 km s^{-1}; the velocity of the receding side is −150 km s^{-1} in the south and −180 km s^{-1} in the north. Scan 2 that crosses the

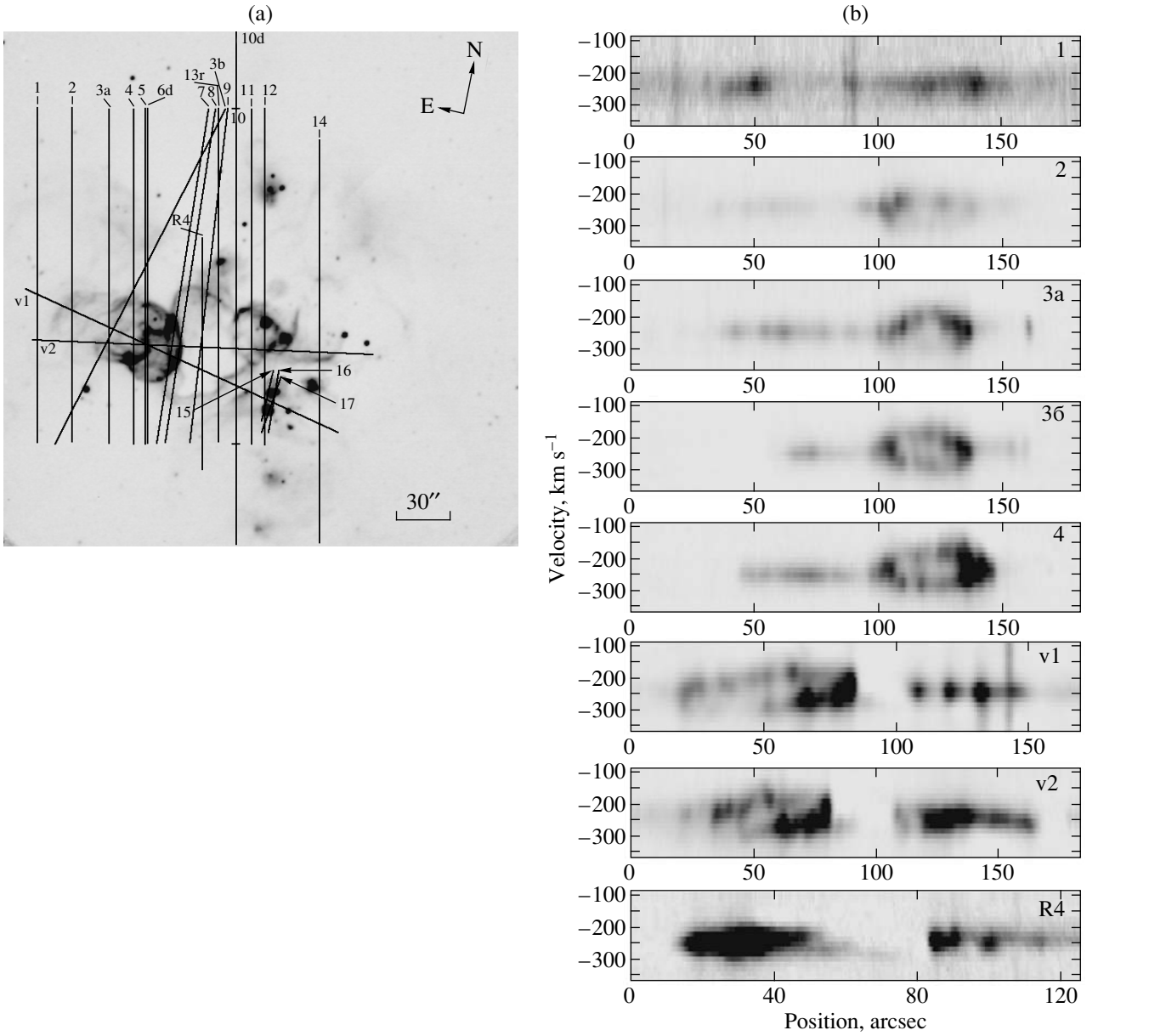

Fig. 3. (a) The localization of the scans shown in Figs. 3b, 3c, and 3d in the Hα image of the complex. The numbers are given at the beginning of each scan. (b) The position–H II velocity diagrams for scans nos. 1, 2, 3a, 3b, 4, v1, v2, and R4 (the velocity is heliocentric). (c) Same as Fig. 3b for scans nos. 5, 6d, 7, 8, 9, 10, and 10d. (d) Same as Fig. 3b for scans nos. 11, 12, 13r, 14, 15, 16, 17.

fainter eastern half of shell R1 also reveals evidence of its expansion. The unshifted features on the shell periphery have a velocity of -240 km s^{-1}, the bright clump in the northern part is observed at a velocity of -215 km s^{-1}, and the faint approaching side has a velocity of -300 km s^{-1}.

Valdez-Gutierrez *et al.* (2001) identified two features in the integrated line profile at velocities of -216 and -274 km s^{-1} in shell R1 and two features at velocities of -244 and -147 km s^{-1} in shell R2. All these values fall within the range determined by the velocity ellipses for these two shells.

The region at the boundary between shells R1 and R2 that, in the 21-cm line, corresponds to the thin bar between the neutral shells I and II, where the chain of early-type stars is located, is represented by scans 5 and 6d. Scan 6d exhibits a bright emission feature in the Hα line at a velocity of about $-270\ldots-280$ km s^{-1}, which corresponds to the bright part of shell R1 with the chain of stars, traces of stellar continuum emission, and a weaker emission feature

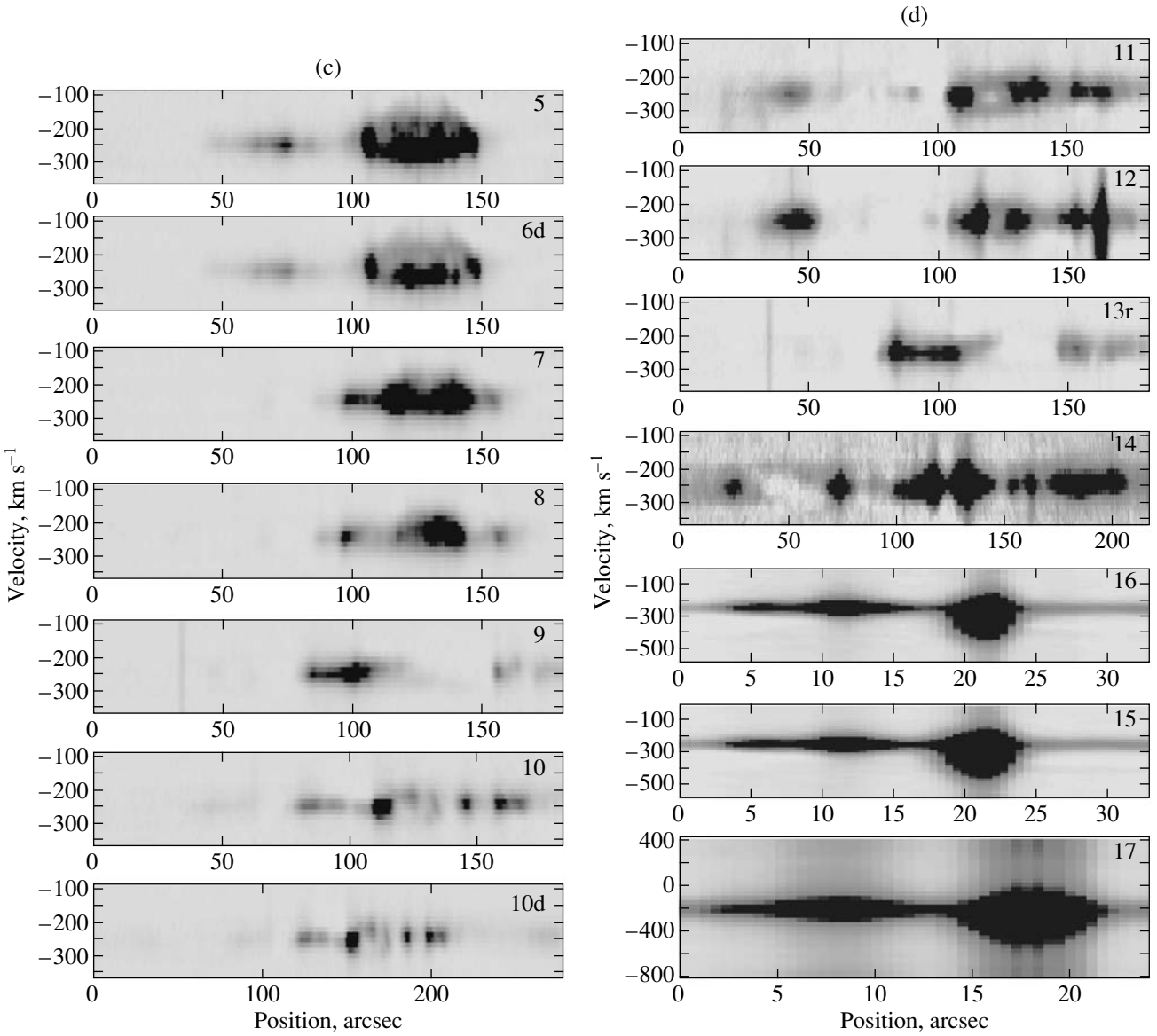

Fig. 3. (Contd.)

in the region of shell R2 at higher velocities, up to $-130\ldots-150$ km s^{-1}. This entire region on scan 6d (105–150 arcsec) widens toward the center, with the dense clumps on the periphery and the gas in the remote part (at 55–85 arcsec) emitting at a velocity of from -240 to -250 km s^{-1}. The observed picture suggests an asymmetric gas expansion in shell R2 at a velocity of about 30 km s^{-1} into a denser medium and at a velocity of about 100–110 km s^{-1} into a less dense medium. We associate this effect with shell R2, because the boundary of the expanding region on scan 6d coincides with the boundary of this shell. Scan 5 also exhibits irregular motions of the receding gaseous clumps up to velocities of from -150 to -160 km s^{-1}; these are probably related to the local action of the wind from the chain stars. The velocity of the near side of shell R2, which is brighter and more regular, reaches from -280 to -290 km s^{-1}. Since the bright clumps on the periphery of the velocity ellipse coincide with the boundaries of shell R2, which is larger than shell R1 here, we believe that the velocity ellipse on scans 6 and 5 also reflects the expansion of shell R2.

Shell R4 and Its Possible Collision with Shell R2

R4 is the most extended shell in the chain of bright shells and the only one that completely fits into the surrounding neutral shell. Its central regions

are characterized by weak emission. Scans R4, 9, v1, v2, and 13r show a deficit of gas in the central cavity and intense emission on the periphery at a velocity of about -240 km s^{-1}. The weak Hα emission features in the central cavity exhibit a blueshift and a redshift relative to this velocity. Weak diffuse emission is observed at velocities up to -200 km s^{-1} (scan R4, 40–55 arcsec; scan 9, 110–120 arcsec) in the north of the cavity and up to -290 km s^{-1} (scan R4, 55–70 arcsec; scan 9, 120–130 arcsec) in the south. The shell expansion velocity determined by these features is $\sim$45 km s^{-1}.

The monochromatic Hα image shows a characteristic lenticular structure at the boundary between shells R2 and R4. This structure can be a manifestation of the dense gaseous ring formed in the region of head-on collision between these shells and oriented almost edge-on to the observer. The formation of this ring follows from three-dimensional numerical simulations of the collision between two expanding shells [see Chernin *et al.* (1995) and references therein].

In the region that corresponds to the eastern boundary of shell R4 (scan 7, 95–115 arcsec), we see no significant deviations from the mean ionized-gas velocity of -240 km s^{-1} in the complex. The inclined ring in the region of collision with shell R2 is observed as two bright unaccelerated clumps and high-velocity motions between them (scan 7, 120 and 140 arcsec) and as a bright structure with high velocities of the internal motions (scan 8, from 120 to 140 arcsec). The velocities of the faint features between the bright clumps are at a maximum; they reach -140 and -340 km s^{-1} at 7% I(max) on scan 7a and -160 km s^{-1} at 10% I(max) on scan 8.

Shell R5

A characteristic arc structure (110–135 arcsec on scan 10 and 150–175 arcsec on scan 10d) is observed at the boundary between shells R4 and R5. This structure may represent the half of the velocity ellipse that corresponds to the receding side of shell R5. We estimated the expansion velocity to be 40–50 km s^{-1}.

Scan 11 (105–135 arcsec) also shows a symmetric expansion of shell R5 at a velocity of about 35–45 km s^{-1}; the velocities of the two sides of the shell are -220 and -310 km s^{-1}.

A compact group of stars with the only Of star identified in the galaxy (Lozinskaya *et al.* 2002) is located on the periphery of shell R5. Scan 12 shows this star in a region of 118 arcsec; the star is surrounded by a bright compact H II region. Given the IFP501 instrumental profile, the line width in the H II region at 0.5I(max) is 50 ± 5 km s^{-1}.

Shell R13 and the H II Region no. 55 from the List of Hodge et al. (1990)

Shell R13, which adjoins shell R4 in the north, consists of two components: a diffuse shell and the bright compact H II region no. 55 (Hodge *et al.* 1990). The bright H II region shows a mean velocity of about $-230 \ldots -240$ km s^{-1} [in agreement with the measurements of Valdez-Gutierrez *et al.* (2001)] and stellar continuum at the center (scan 13r, position 85 arcsec). A group of stars may be located here, because area of the stellar continuum is larger than that in other regions of the same scan. The line width in the bright H II region reaches 57 km s^{-1} at 0.5I(max).

The diffuse shell R13 also exhibits the mean radial velocity of from -230 to -240 km s^{-1} typical of the entire complex. We found no clear evidence of shell-R13 expansion.

Shells R6 and R8

According to our data, the expansion velocity of shell R6 does not exceed 20 km s^{-1}: the velocities of the northern and southern shell boundaries (scan 14, 75 and 120 arcsec, respectively) and the velocity in the central region (about 100 arcsec on the same scan) are about -255 km s^{-1}.

Shell R8 exhibits the characteristic arc-shaped pattern of radial-velocity variation of the far side. The velocity of the bright boundary regions (scan 14, 25 and 75 arcsec) is -255 km s^{-1} and the velocity of the faint far side reaches -190 km s^{-1}, which gives an expansion velocity of about 65 km s^{-1}. We detected no emission from the even fainter near side.

The Bright H II Regions nos. 40a,b and 39 (Hodge et al. 1990)

Valdez-Gutierrez *et al.* (2001) provided the following parameters averaged over the group of object nos. 40a,b and 39: the velocity at the line peak, -239 km s^{-1}, and the velocity dispersion, 10.4 km s^{-1}. We separately scanned the two bright sources no. 40a (scan 16) and no. 40b (scan 15); both also include the emission from the more extended and fainter region no. 39. As follows from Fig. 3d, the velocity at the peak of these three regions is -240 km s^{-1}. The H II region no. 39 is characterized by a narrow Hα line with no wings with the FWHM determined by the IFP501 instrumental profile along the entire length. At the same time, both bright compact H II regions nos. 40a and 40b (scans 16 and 15, respectively) exhibit weak emission at 10% I(max) in the velocity range from -310 to -175 km s^{-1}.

The Supernova Remnant

The bright nebula S8 (Sandage 1971), the supernova remnant, shows emission over the entire velocity range from 0 to -600 km s^{-1} determined by the IFP501 free spectral range (scans 15 and 16, 19–23 arcsec). The remnant emission is observed with IFP235 at least in the velocity range from $+200$ to -600 km s^{-1} (scan 17). An interfering emission emerges at higher velocities, $+400$ and -800 km s^{-1}. This emission is probably attributable to an improper allowance for the night-sky 6554-Å line.

This result is in complete agreement with previous observations of Lozinskaya *et al.* (1998) and Rosado *et al.* (2001).

All of the ionized shells in the complex of star formation for which we managed to reliably detect their expansion based on the velocity ellipse are collected in Table 3. For comparison, the fourth column of the table gives the expansion velocities of the same shells determined by Valdez-Gutierrez *et al.* (2001) from line-profile splitting. Since the shell sizes were measured from our deep images, they differ slightly from those of Valdez-Gutierrez *et al.* (2001). It should be noted that, given the irregular shape of most shells, the representation of the observed shells by regular ellipses is arbitrary and subjective in nature.

In estimating the kinematic ages of the shells from their radii and expansion velocities, we used the classical theory of wind-blown bubbles ($t = 0.6\ R/V$). In addition to the age, the mean radius and expansion velocity used for its estimation are given in parentheses (in the form R/V) in the last column of the table. The ages of shells R3 and R6 correspond to the data from Valdez-Gutierrez *et al.* (2001).

Table 3. Parameters of the bright ionized shells in the complex

Shell	Size, pc	V_{exp}, km s^{-1}	V_{exp}(V–G), km s^{-1}	Age, Myr
R1	188×138	60–75	29	0.7 (81/67)
R2	145×88	50–60	49	0.6 (58/55)
R3	258×209		30	1.9 (C–D)
R4	234×138	40–45	32	2.2 (93/42)
R5	113×113	30–50	38	0.8 (56/40)
R6	226×184	$\leq$20	25	2.0 (V–G)
R8	217×154	$\simeq$65	26	1.7 (185/65)

6. DISCUSSION

The radial-velocity variations with distance from the center of the ionized shells (velocity ellipses) found here are generally in agreement with the observations of Meaburn *et al.* (1988) and Valdez-Gutierrez *et al.* (2001), but they give a clearer picture of expansion. In the latter paper, the conclusions regarding expansion were drawn from integrated line profile splitting in the shells. Since bright peripheral regions or individual bright clumps can give a significant contribution when averaging over the shell or over its separate fields, the expansion velocity determined in this way can be underestimated. The large brightness difference between the approaching and receding sides of the shells can also cause the expansion velocity inferred from line splitting to be underestimated. The constructed velocity ellipses allow these difficulties to be circumvented. The expansion velocity can be determined from the velocity ellipse by taking into account the geometrical projection even if only one shell side is observed, as in the case of R8. Indeed, as we see from Table 3, our estimates of the expansion velocity in most shells gave higher values than those in Valdez-Gutierrez *et al.* (2001).

In several shells, we detected a distinct asymmetry in their expansion: the approaching and receding sides have different velocities.

On scans v1 and v2 crossing the entire chain of the brightest ionized shells, we clearly see that all of them generally have similar velocities but an irregular, clumpy brightness distribution. This irregular brightness distribution may have served as the basis for the conclusion of Valdez-Gutierrez *et al.* (2001) that shells R1 and R2 are at different distances, because they are observed at different radial velocities. These scans show that individual bright clumps on the two sides of these shells actually have different velocities but they all fall within our velocity ellipses. According to our measurements, the approaching and receding sides of the two shells have similar velocities: from -290 to -320 and from -170 to -190 km s^{-1}, as inferred from different scans in R1; from -280 to -300 and -170 km s^{-1} in R2. The far side is brighter in R1 and the near side is brighter in R2. We also noted that the southern part of shell R1 recedes faster ($V = -150$ km s^{-1}) than does its northern part ($V = -180$ km s^{-1}).

Taking into account the structure of R1 and R2 in different velocity ranges, we do not rule out the possibility that these shells generally constitute a single dumbbell-like structure formed on both sides of a dense neutral-gas layer. However, this assumption requires additional observational confirmation.

Valdez-Gutierrez *et al.* (2001) showed that the the energy of the stellar wind from nearby OB associations was enough for most of the ionized shells to be formed. The rapidly expanding shells R1 and R2

constitute an exception. We further increased the expansion velocity of these two objects (see Table. 3) but simultaneously found additional, most intense sources of the stellar wind at their boundary—early-type supergiants and giants (Lozinskaya *et al.* 2002), which removes the problem of the mechanical energy sources.

Recall also that the two mentioned shells R1 and R2 exhibit an intense emission feature in the [S II] 6717/6731 Å lines (see Valdez-Gutierrez *et al.* 2001; Lozinskaya *et al.* 2002), typical of the radiation of the shock waves generated by a supernova explosion.

The neutral shells produced by the combined effect of the wind and supernovae in OB associations are being widely searched for in nearby galaxies (see, e.g., the review article by Brinks 1994; Kim *et al.* 1999; Oey *et al.* 2002 and references therein). In most cases, the 21-cm observations either do not reveal any distinct neutral-gas shell structure around OB associations at all or do not allow the neutral-gas structures to be unambiguously associated with H II shells. The studies of neutral gas in the vicinity of the three well-known ionized supershells in the LMC carried out by Oey *et al.* (2002) serve as a clear example.

The complex of star formation in IC 1613 constitutes a lucky exception. We do not know any other examples of such a distinct interaction between multiple ionized and neutral shells that is observed in the complex under discussion.

Here, we have studied the kinematics of the identified neutral shells I, II, and III for the first time. We have also detected expansion and measured the expansion velocity for the first time.

As was mentioned in Section 3, the derived radii and expansion velocities of the H I shells in IC 1613 fall within the region of the peak in the distribution of neutral shells in the LMC and SMC in size and expansion velocity. The age of the H I shells in the complex of star formation in IC 1613 (5.3–5.5 Myr) is also in complete agreement with the peaks in the age distributions of H I supershells in the LMC (4.9 Myr; Kim *et al.* 1999) and in the SMC (5.4 Myr; Staveley-Smith *et al.* (1997).

We estimated the kinematic ages of the neutral shells II and III in Table 2 from their mean radii and expansion velocities by using the classical theory of a constant stellar wind in a homogeneous medium. This assumes that the mechanical luminosity of the wind from the association stars responsible for the shell formation does not vary with time and that all stars were formed simultaneously. Of course, both assumptions are not valid, although they are universally accepted. Allowance for sequential star formation and for variations in the mass loss rate during the evolution of a rich association as well as for the clumpy structure of the interstellar medium can change the age estimate by a factor of 1.5 to 3 (see, e.g., Shull and Saken 1995; Oey *et al.* 1996; Silich *et al.* 1996; Silich and Franco 1999; and references therein). Nevertheless, we may conclude that the derived ages of shells II (5.6 Myr) and III (5.3 Myr) agree with the ages of the stellar associations in the complex of star formation. Shell I, whose expansion we failed to detect, is similar in size to shells II and III and is most likely similar in age.

The three-color photometry of stars in IC 1613 performed by Hodge *et al.* (1991) gave a minimum age of the stars in their field no. 1, where the neutral shells that we identified are located, equal to 5 Myr. This field includes associations nos. 10, 12, 13, 14, 15, and 17 from the list by Hodge (1978), whose mean and minimum ages were estimated by Hodge *et al.* (1991) to be 17 and 3 Myr, respectively. Recent estimates by Georgiev *et al.* (1999) yielded similar results: the age of the youngest nearby associations nos. 10 and 14 is about 5 Myr and the age of the oldest associations (nos. 12, 19, and 19) reaches 20 Myr.

The mechanical wind luminosity that is required for the neutral shells observed in the complex to be formed and that is determined by using the classical model (with all of the reservations made above) is 5×10^{38}, 5×10^{37}, and 5×10^{36} erg s^{-1} in a medium with an initial density of 10, 1, and 0.1 cm^{-3}, respectively. These values seem reasonable enough for the stars found in the region—the sources of a strong stellar wind (see Valdez-Gutierrez *et al.* 2001; Lozinskaya *et al.* 2002). It should be emphasized, however, that the spectra of bright stars in the region are required to adequately discuss the sources of mechanical energy. Lozinskaya *et al.* (2002) obtained the spectra of stars only in three small fields of the star-forming complex and detected stars with strong winds, blue supergiants and Of stars, in two of them.

Despite the "suitable" age and input of mechanical energy, we do not consider it possible to unequivocally associate the formation of neutral shells with the action of the stellar wind from the OB associations identified by Georgiev *et al.* (1999) for the following reasons.

First, most of the H I supershells identified in the LMC, the SMC, and other Local-Group galaxies are several-fold younger than the corresponding OB associations (see, e.g., Kim *et al.* 1999; Staveley-Smith *et al.* 1997, and references therein). Therefore, it may well be that the H I shells that we detected in IC 1613 were also formed by an older population that the groups of young stars shown in Fig. 1c.

As follows from Table 3 and from similar estimates by Valdez-Gutierrez *et al.* (2001), the ages of most of the ionized shells in the complex lie within the range from 0.6 to 2.2 Myr. These ages are much younger

than the ages of the OB associations that could be responsible for their formation. Such a situation is observed in most galactic and extragalactic ionized shells and supershells. In general, to explain this mismatch, either noncoeval star formation is assumed or the shells are assumed to be formed only by stars at a late evolutionary stage—WR, Of, and BSG with a short-duration, but intense wind. The situation in the complex under consideration is more complicated, because the bright ionized shells are localized inside or at the boundary of the older neutral shells and their evolution differs significantly from the standard theory.

In addition, a number of observed facts actually suggest noncoeval star formation in the complex.

Figure 1c suggests that all of the young OB associations in the region are localized not at the center but in the dense peripheral parts of the H I shells [the only association no. 7 from the list by Georgiev *et al.* (1999) is partly located inside shell III). In general, this picture may provide evidence for the formation of these associations in dense H I shells. We emphasize that the new association boundaries delineated by Georgiev *et al.* (1999) split the associations of Hodge (1978) into smaller groups, which are believed to be the young nuclei of the corresponding associations. The scenario for triggered star formation in expanding shells was considered by many authors [see, e.g., Elmegreen *et al.* (2002) and references therein].

Comparison of the ages and mutual localizations of the ionized and neutral structures in the complex also suggests noncoeval star formation. All the ionized shells are several-fold younger than the neutral shells. As was pointed out in Section 3, most of the bright ionized shells are located in the dense peripheral parts of the H I shells. The only exception is shell R4, which completely fits into the neutral shell II from the inside. According to our measurements, this ionized shell is oldest and all the young nuclei of the OB associations are located in its boundary regions (see Fig. 1c).

However, these arguments for sequential or triggered star formation, which refer to the neutral shells of the complex studied in detail here, are speculative, because the age difference between the H I and H II shells is small.

The multishell complex itself, which represents the only region of violent ongoing star formation in IC 1613, may have been produced by the collision of two older and more massive giant neutral supershells (Lozinskaya 2002, 2003). Indeed, in addition to the three bright and relatively small H I shells considered here, a giant H I ring south of the star-forming complex and a giant arc structure in the north, which probably also represents part of the neutral supershell, can be identified in Fig. 2a. The characteristic size of the two structures is ~1–1.5 kpc. The complex of ongoing star formation lies at their common boundary, where the collision of these two giant supershells could trigger violent star formation. We are planning to consider this scenario in detail.

7. CONCLUSIONS

We studied in detail the structure and kinematics of the neutral and ionized gas components in the only known complex of star formation in the irregular dwarf galaxy IC 1613.

To study the kinematics of the ionized shells, we carried out Hα observations with a scanning Fabry–Perot interferometer attached to the 6-m SAO telescope. The monochromatic Hα image of the multishell complex obtained from our interferometric observations reveals new faint filamentary structures in several regions of the complex.

We constructed position–radial velocity diagrams, which cover the entire complex of star formation almost uniformly. The characteristic velocity variation with distance from the center, the velocity ellipse, was used to refine (increase) the expansion velocities of most ionized shells in the complex estimated by Valdez-Gutierrez *et al.* (2001). The expansion in several shells was found to be asymmetric: the approaching and receding sides of the shells have different velocities.

Based on our VLA 21-cm observations, we have studied the neutral-gas kinematics in the complex of star formation for the first time. The mean H I velocity in the complex is $V_{\rm Hel} = -230 \pm 5$ km s^{-1}, in good agreement with the estimate obtained by Lake and Skillman (1989) for this part of the galaxy from low-angular-resolution observations.

We identified three extended (300–350 pc) neutral shells with which the brightest ionized shells in the complex of star formation are associated. The two H I shells were found to expand at a velocity of 15–18 km s^{-1}.

The sizes, expansion velocities, and kinematic ages of the neutral shells in the complex fall within the regions of the peaks in the corresponding distributions for giant shells in the LMC and SMC.

We identified an incomplete H I shell with the only known supernova remnant in the galaxy located at its inner boundary. This confirms the scenario for a supernova explosion inside a cavity surrounded by a dense shell and a collision of the remnant with the shell wall suggested by Lozinskaya *et al.* (1998) to explain the peculiarity of this remnant, which combines the properties of young and old objects.

We found evidence of the physical interaction between the H I and H II shells in the region of the chain

of stars, early-type giants and supergiants, detected by Lozinskaya *et al.* (2002). The region at the boundary of the two shells where the stellar chain is located was shown to be the dynamically most active part of the star-forming complex. The highest H II and H I velocities are observed here.

The relative positions and ages of the H I and H II shells and OB associations in the complex suggest sequential or triggered star formation in the expanding neutral shells.

In addition to the three brightest and most prominent H I shells, we found supergiant arches and ring structures in the galaxy whose sizes are comparable to the gaseous-disk thickness. These may be assumed to be the traces of preceding starbursts in IC 1613.

ACKNOWLEDGMENTS

This study was supported by the Russian Foundation for Basic Research (project nos. 01-02-16118 and 02-02-06048mas), the Federal Central Research Program (contract 40.022.1.1.1102), and CONACYT (Mexico, project 36132-E). The observational data were obtained with the 6-m SAO telescope financed by the Ministry of Science of Russia (registration number 01-43). We are grateful to the 6-m Telescope Committee for allocating observational time. The National Radio Astronomy Observatory (NRAO) is operated by the Association of Universities Inc. under a contract with the NSF. We wish to thank S.A. Silich for helpful remarks.

REFERENCES

1. V. L. Afanas'ev, T. A. Lozinskaya, A. V. Moiseev, and E. Blanton, Pis'ma Astron. Zh. **26**, 190 (2000) [Astron. Lett. **26**, 153 (2000)].
2. E. Brinks, in *Violent Star Formation from 30 Doradus to QSOs,* Ed. by G. Tenorio-Tagle (Cambridge Univ. Press, Cambridge, 1994), p. 145.
3. A. D. Chernin, Yu. N. Efremov, and P. A. Voinovich, Mon. Not. R. Astron. Soc. **275**, 313 (1995).
4. A. D. Chernin and T. A. Lozinskaya, Astron. Astrophys. Trans. **21** (3) (2003).
5. A. Dolphin, A. Saha, E. D. Skillman, *et al.*, Astrophys. J. **550**, 554 (2001).
6. B. G. Elmegreen, J. Palous, and S. Ehlerova, Mon. Not. R. Astron. Soc. **334**, 693 (2002).
7. W. Freedman, Astrophys. J. **326**, 691 (1988a).
8. W. Freedman, Astron. J. **96**, 1248 (1988b).
9. L. Georgiev, J. Borissova, M. Rosado, *et al.*, Astron. Astrophys., Suppl. Ser. **134**, 21 (1999).
10. P. W. Hodge, Astrophys. J., Suppl. Ser. **37**, 145 (1978).
11. P. Hodge, M. G. Lee, and M. Gurwell, Publ. Astron. Soc. Pac. **102**, 1245 (1990).
12. P. W. Hodge, T. R. Smith, P. B. Eskridge, *et al.*, Astrophys. J. **369**, 372 (1991).
13. D. A. Hunter, W. N. Hawley, and J. S. Gallagher, Astron. J. **106**, 1797 (1993).
14. S. Kim, M. A. Dopita, L. Staveley-Smith, and M. S. Bessell, Astron. J. **118**, 2797 (1999).
15. G. Lake and E. D. Skillman, Astron. J. **98**, 1274 (1989).
16. J. Lequeux, N. Meysonnier, and M. Azzopardi, Astron. Astrophys., Suppl. Ser. **67**, 169 (1987).
17. T. A. Lozinskaya, Astron. Astrophys. Trans. **21** (3) (2003).
18. T. A. Lozinskaya, *Proceedings of Conference "Seeng Through the Dust: The Detection of HI and the Exploration of the ISM of Galaxies," Penticton, Canada, 2001,* Ed. by R. Taylor, T. Landecker, and T. Willis (2002) (in press).
19. T. A. Lozinskaya, O. K. Silchenko, D. J. Helfand, and M. W. Goss, Astron. J. **116**, 2328 (1998).
20. T. A. Lozinskaya, A. V. Moiseev, V. L. Afanas'ev, *et al.*, Astron. Zh. **78**, 485 (2001) [Astron. Rep. **45**, 417 (2001)].
21. T. A. Lozinskaya, V. P. Arkhipova, A. V. Moiseev, and V. L. Afanas'ev, Astron. Zh. **79**, 19 (2002) [Astron. Rep. **46**, 16 (2002)].
22. I. Meaburn, Mon. Not. R. Astron. Soc. **192**, 365 (1980).
23. J. Meaburn, C. A. Clayton, and M. J. Whitehead, Mon. Not. R. Astron. Soc. **235**, 479 (1988).
24. A. V. Moiseev, Preprint SAO RAN No. 166, 1 (2002).
25. M. S. Oey, Astrophys. J. **467**, 666 (1996).
26. M. S. Oey, B. Groves, L. Staveley-Smith, and R. C. Smith, Astron. J. **123**, 255 (2002).
27. J. S. Price, S. F. Mason, and C. A. Gullixson, Astron. J. **100**, 420 (1990).
28. M. Rosado, M. Valdez-Guterrez, L. Georgiev, *et al.*, Astron. Astrophys. **122**, 194 (2001).
29. A. Sandage, Astrophys. J. **166**, 13 (1971).
30. J. M. Shull and J. M. Saken, Astrophys. J. **444**, 663 (1995).
31. S. A. Silich, J. Franco, J. Palous, and G. Tenorio-Tagle, Astrophys. J. **468**, 722 (1996).
32. S. A. Silich and J. Franco, Astrophys. J. **522**, 863 (1999).
33. L. Staveley-Smith, R. J. Sault, D. Hatzidimitriou, *et al.*, Mon. Not. R. Astron. Soc. **289**, 225 (1997).
34. M. Valdez-Gutierrez, M. Rosado, L. Georgiev, *et al.*, Astron. Astrophys. **366**, 35 (2001).

Translated by V. Astakhov

Astronomy Letters, Vol. 29, No. 2, 2003, pp. 91–95. Translated from Pis'ma v Astronomicheskiĭ Zhurnal, Vol. 29, No. 2, 2003, pp. 111–115.

Detection of Giant Pulses from the Pulsar PSR B1112+50

A. A. Ershov and A. D. Kuzmin*

Pushchino Radio Astronomy Observatory, Astrospace Center, Lebedev Physical Institute, Russian Academy of Sciences, Pushchino, Moscow oblast', 142292 Russia

Received August 29, 2002

Abstract—We detected giant pulses from the pulsar PSR B1112+50. A pulse with an intensity that is a factor of 30 or more higher than the intensity of the average pulse is encountered approximately once in 150 observed pulses. The peak flux density of the strongest pulse is about 180 Jy. This value is a factor of 80 higher than the peak flux density of the average pulse. The giant pulses are narrower than the average profile by approximately a factor of 5 and they cluster about the center of the average profile.

Key words: *pulsars, neutron stars and black holes, giant pulses.*

INTRODUCTION

Giant pulses (GPs) are short-duration burstlike increases in the intensity of individual radio pulses from pulsars. These are rare events observed only in three pulsars: the Crab pulsar PSR B0531+21 (Staelin and Sutton 1970), the millisecond pulsar PSR B1937+21 (Wolszczan *et al.* 1984), and PSR B1821−24 (Romani and Johnston 2001).

For normal pulsars, the intensity of individual pulses exceeds the intensity of the average pulse by no more than several factors (Hesse and Wielebinski 1974; Ritchings 1976). The GPs in the Crab pulsar PSR B0531+21 exceed the average level by a factor of 20 to 2×10^3 (Lundgren *et al.* 1995). The GPs in the millisecond pulsar PSR B1937+21 and PSR B1821−24 exceed the average level by factors of 20 to 300 (Wolszczan *et al.* 1984; Cognard *et al.* 1996) and 20 to 80 (Romani and Johnston 2001), respectively.

Kuzmin and Losovskii (2002) detected an extremely high brightness temperature $T_B \geq 4 \times 10^{35}$ K of GPs in the millisecond pulsar PSR B1937+21.

The GP duration is much shorter than the duration of the average pulses from these pulsars. The GP width for the millisecond pulsar PSR B1937+21 at frequencies of 430, 1420, and 2380 MHz does not exceed 10 μs, which is a factor of 10 smaller than the width of the average profile, 100 μs (Kinkhabwala and Thorsett 2000). The GP position is stable inside the average profile.

A characteristic feature of the pulsars with GPs is a two-component intensity distribution: lognormal for most of the pulses and a power-law $N \propto S^\alpha$ for GPs with intensities above a certain level (Argyle and Gower 1972; Lundgren *et al.* 1995).

The power-law index for the Crab pulsar is $\alpha = -3.3$ (Argyle and Gower 1972; Lundgren *et al.* 1995). The boundary at which the distribution changes its pattern corresponds to about a 30-fold intensity of the average pulse. GPs account for about 2.5% of the total number of pulses (Lundgren *et al.* 1995). Pulses that exceed the average level by a factor of 50 occur approximately once in 10^5 pulses (Argyle and Gower 1972). The power-law index of the intensity distribution for PSR B1937+21 is equal to $\alpha = -1.8 \pm 0.1$. Pulses that exceed the average level by a factor of 20 occur approximately once in 10^4 pulses. An excess up to 100 times above the average level is encountered approximately once in 10^5 pulses (Cognard *et al.* 1996; Kinkhabwala and Thorsett 2000).

Johnston *et al* (2001), Cramer *et al.* (2002), and Johnston and Romani (2002) reported the discovery of a new type of GP−GP-microstructure in the Vela pulsar and PSR B1706−44. The intensity distribution of this microstructure also contains a power-law branch with indices of −2.85 and −2.7, respectively. However, in contrast to classical GPs (in PSR B0531+21, PSR B1821−24, and PSR B1937+21), the excess of the intensity of microstructural GPs above the intensity of the average pulse is less than a factor of 10 and 4 for the Vela pulsar and PSR B1706−44, respectively.

Attempts to find GPs in other pulsars (Phinney and Taylor 1979; Johnston and Romani 2002) have failed thus far.

*E-mail: akuzmin@prao.psn.ru

1063-7737/03/2902-0091$24.00

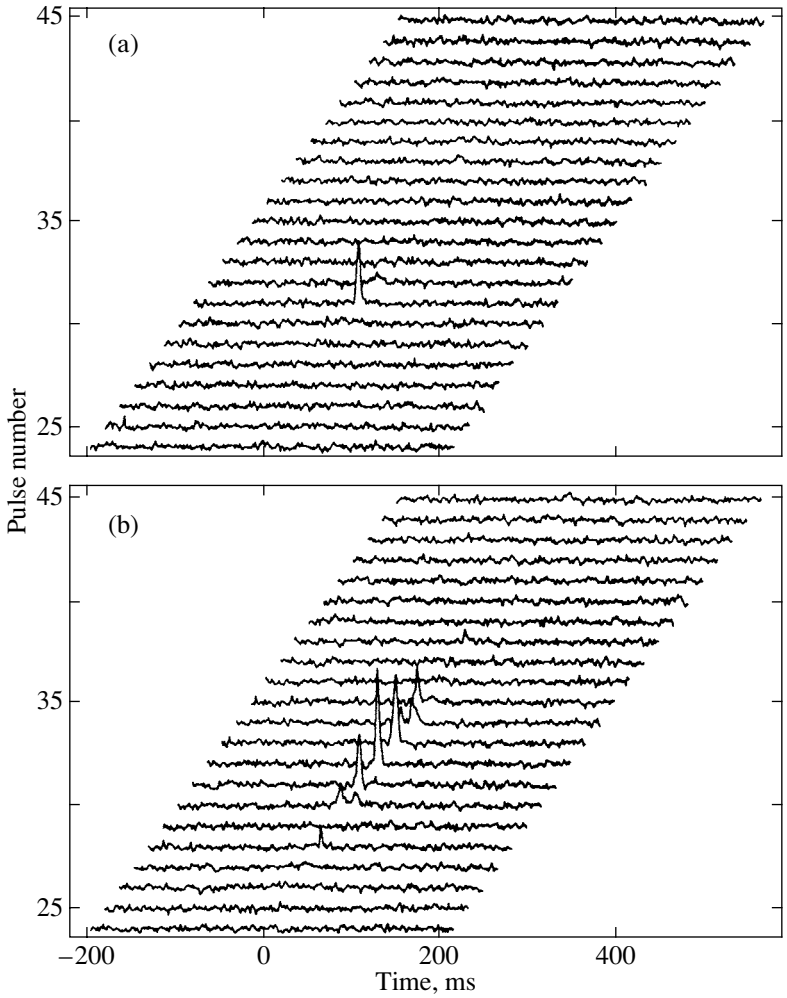

Fig. 1. Examples of GPs from PSR B1112+50: (a) a single GP with a peak intensity of 120 Jy, (b) the strongest GP with a peak intensity of about 180 Jy, which belongs to the series of six strong pulses.

We detected GPs from PSR B1112+50, which exhibit the characteristic features of GPs.

OBSERVATIONS AND DATA REDUCTION

Our observations were carried out from January 9 through June 30, 2002, with the Large-Aperture Synthesis (BSA) Radio Telescope at the Pushchino Radio Astronomical Observatory of the Astrospace Center of the Lebedev Physical Institute. The telescope has an effective area of about 30 000 square meters at zenith. One linear polarization was received. We used a 128-channel receiver with the channel bandwidth $\Delta f = 20$ kHz. The frequency of the first (highest frequency) channel was 111.870 MHz, the sampling interval was 0.922 ms, and the time constant was $\tau = 1$ ms. We observed individual pulses. The duration of one observing session was about 5 min; 180 pulses were observed during one session.

We measured the GP flux densities using the calibration method based on noise measured from discrete sources with known flux densities in units of radio telescope flux sensitivity δS. The pulsar peak flux density of the observed pulse $S_{\max_{\rm obs}}$ was determined from the relation

$$S_{\max_{\rm obs}} = \delta S / k_{\rm PSR} \times (\Delta f \tau)^{-1/2} \times ({\rm S/N}),$$

where $k_{\rm PSR} = \sin(h_{\rm PSR})$ is the factor that takes into account the dependence of the effective area of the radio telescope on pulsar height $h_{\rm PSR}$, $\Delta f = 2.56$ MHz is the total system bandwidth, $\tau = 1$ ms is the time constant of the output device, and S/N is the signal-to-noise ratio. According to Kuzmin and Losovsky (2000), δS was represented as

$$\delta S = \delta S_{1000}(a + bT_{\rm bb}),$$

where δS_{1000} is the flux sensitivity of the radio telescope toward a sky region with the brightness temperature $T_0 = 1000$ K and $T_{\rm bb}$ is the brightness tem-

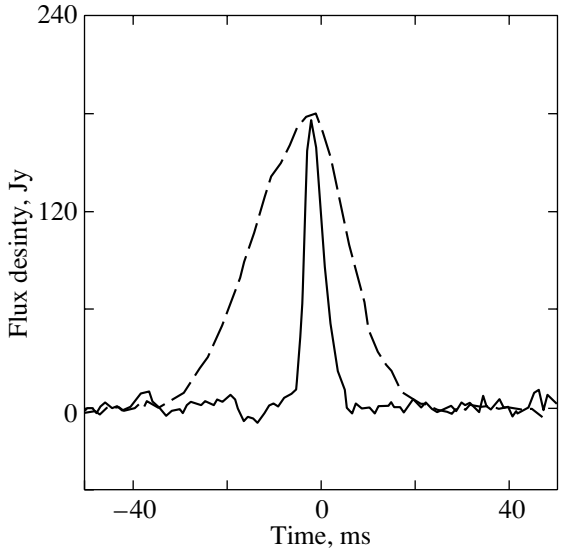

Fig. 2. The strongest GP from PSR B1112+50 (solid line) shown with the average pulse (dashed line). The amplitude of the average profile was increased by a factor of 80.

perature of the sky background toward the pulsar. We assumed δS_{1000} to be 100 mJy/MHz/s (Kutuzov 2000) and took $a = 0.4$ and $b = 0.0006$ from Kuzmin and Losovsky (2000).

Over the above period, we carried out a total of 105 observing sessions containing 18 900 pulsar periods. The peak flux density of the average pulse was $S_{\max_{obs}} \cong 2.3$ Jy. The period-averaged flux density was $S \cong 56$ mJy.

We detected 126 pulses whose peak fluxes exceeded that of the pulse averaged over 105 days of observations by more than a factor of 30; for 17 of them (one pulse per 1100 observed pulses), this excess was more than a factor of 50. The total flux densities of 114 pulses exceeded the total flux density of the average pulse by a factor of 10.

Figure 1 shows two GPs as examples. Figure 1a shows pulse no. 31 of April 23 with a peak flux density of ~120 Jy, which is a factor of 50 higher than the peak flux density of the average pulse.

Of the 126 pulses whose intensity exceeds the intensity of the average pulse by a factor of 30 or more, 36 belong to neighboring pairs or triples; hence, we can estimate the duration of enhanced pulsar activity to be several seconds. An example of such a GP group is shown in the Fig. 1b, which presents the strongest individual pulse in all 105 days of observations (pulse no. 32 of January 16). This pulse has a peak flux density of ~180 Jy, which is a factor of 80 higher than that of the average pulse, and the total flux density of this pulse exceeds that of the average pulse by a factor of 16. The large increase in pulsar activity lasted for six periods, i.e., ~10 s.

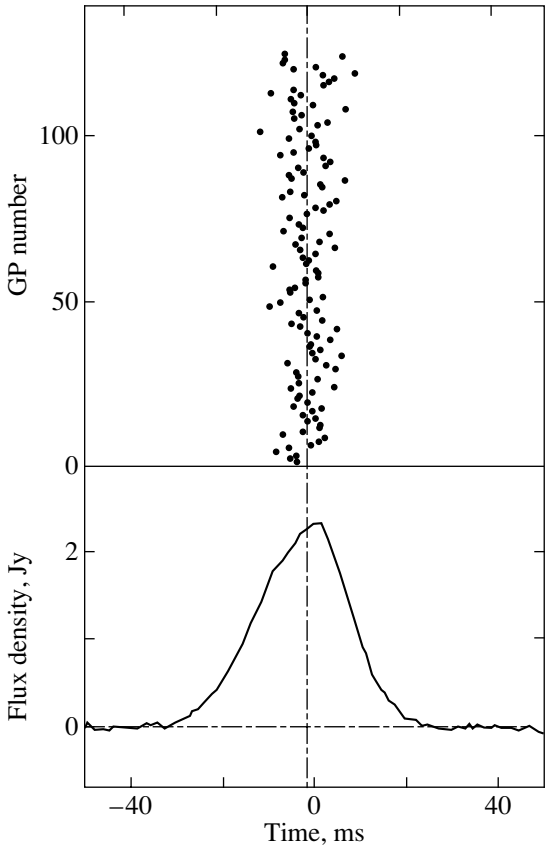

Fig. 3. The phases of the observed GPs relative to the center of the average profile.

Figure 2 shows one of the GPs (January 16, 2002) in comparison with the average profile. The peak flux density of the average pulse is about 1/10 of the width of the noise track of the GP. Therefore, we increased the average profile by a factor of 80 for convenience. The GP width is $w_{50} = 4$ ms $= 0.^{\circ}9$ at a 0.5 level and $w_{10} = 7$ ms $= 1.^{\circ}5$ at a 0.1 level. The mean width of the 126 GPs is $w_{50} = 5.1 \pm 1.2$ ms $= 1.1 \pm 0.^{\circ}3$ at a 0.5 level and $w_{10} = 9 \pm 2$ ms $= 2 \pm 0.^{\circ}4$ at a 0.1 level. The dispersion broadening $\Delta t_{DM} = 1.1$ ms and the receiver time constant 1 ms have virtually no effect on the GP width. The width of the pulsar profile averaged over 105 observing sessions is $w_{50} = 24$ ms $= 5.^{\circ}2$ and $w_{10} = 44$ ms $= 9.^{\circ}6$ at 0.5 and 0.1 levels, respectively. Thus, the GPs are narrower than the average pulse by approximately a factor of 5, typical of the GPs.

Figure 3 shows the phases of the observed GPs relative to the center of the average profile. The positions of GPs are stable inside the average profile and they cluster in the middle part of the average profile. The phase difference between the GPs and the av-

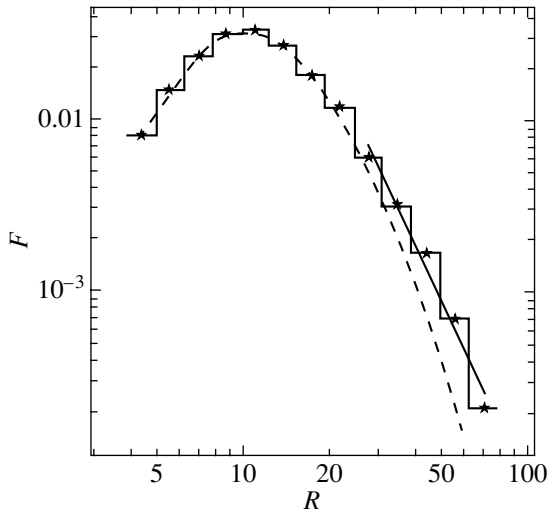

Fig. 4. The distribution of peak intensities of individual pulses from PSR B1112+50. The ratio R of the GP peak flux density to the peak flux density of the average profile is plotted along the x axis. Equal intervals correspond to an increase in the GP flux density by the same factor. The ratio of the number of GPs exceeding the peak flux density of the average profile to the total number of observed pulses is plotted along the y axis. The dashed line represents the least-squares-fitted lognormal distribution $F(\log R) = A\exp(-B(\log R - C)^2)$ and the solid line represents the power-law distribution $F \propto (I_{\rm GP}/I_{\rm AP})^{\alpha}$.

erage profile is $\Phi_{\rm GP} - \Phi_{\rm AP} = -1 \pm 4$ ms $\cong (-0.02 \pm 0.1)w_{10}$.

The GP brightness temperature is

$$T_{\rm B} = S\lambda^2/2k\Omega,$$

where λ is the wavelength of the received radio emission, k is the Boltzmann constant, and Ω is the solid angle of the radio emitting region. Assuming the size of the radio emitting region to be $l \le cw_{50\,\rm GP}$, where c is the speed of light, and the distance to the pulsar to be $d = 0.54$ kpc (Taylor *et al.* 1995), we obtain $T_{\rm B} \ge 10^{26}$ K for $w_{50} = 4$ ms and $S = 180$ m Jy .

The GPs that we detected are not scintillations. At the frequency of our observations (111 MHz), the interstellar scintillation time scale (the time correlation radius) for a pulsar with the dispersion measure $DM = 9.16$ pc cm^{-3} is about 1 min and 1000 days, respectively, for refraction and diffraction scintillations (Shishov *et al.* 1995), which significantly exceeds the duration of the observed GPs (less than several seconds). No GPs were detected in several pulsars with similar or lower dispersion measures observed during this period.

DISCUSSION

The GPs that we detected from PSR B1112+50 exhibit the characteristic features of classical GPs from PSR B0531+21 and PSR B1937+21. The GP peak intensity exceeds the peak intensity of the average pulse by more than a factor of 30. The fraction of GPs (0.7%) and the boundary of change in the distribution pattern ($\approx$30 intensities of the average pulse) for PSR B1112+50 are comparable to the same parameters of GPs in the Crab Nebula and PSR B1937+21 (2.5% and 0.02% of the total number of pulses and $\approx$30 and 15 intensities of the average pulse, respectively). The GPs are several-fold narrower than the average pulse and their positions are stable inside the average profile.

Figure 4 shows distribution of the ratio R of the peak flux densities of individual pulses from PSR B1112+50 to the peak flux density of the average pulse (in equal bins of the ratio R) inferred from our observations. The distribution was constructed from 3320 pulses whose intensity exceeds the sensitivity threshold of our radio telescope. It exhibits the features of a two-component structure characteristic of GPs: a lognormal distribution for $I_{\rm GP}/I_{\rm AP} < 30$ and a power-law distribution for $I_{\rm GP}/I_{\rm AP} > 30$. The dashed line represents the least-squares-fitted lognormal distribution $F(\log R) = A\exp(-B(\log R - C)^2)$, where $A = 0.03$, $B = 9.4$, and $C = 1.03$. Here, F is the ratio of the number of pulses with a given $\log R$ to the total number of pulses. The solid line represents the power-law distribution $F \propto (I_{\rm GP}/I_{\rm AP})^{\alpha}$. The index $\alpha \cong -3.6$ of the power-law part of the distribution needs to be refined because of poor statistics.

The absence in our observations of GPs exceeding the average pulse by more than a factor of 80 observed for PSR B0531+21 and PSR B1937+21 may stem from the relatively small (because of the long period of PSR B1112+50) number of observed periods, 18 900 (compared to more than 10^6 for PSR B0531+21 and PSR B1937+21). For these pulsars, pulses that exceed the average level by a factor of 80 occur approximately once in 10^5 pulses.

Note that PSR B1112+50 does not belong to the group of pulsars with the strongest magnetic fields on the light cylinder, an integrated radio luminosity, and a potential difference in the polar-cap gap (Kuzmin 2002). Therefore, the GP of this pulsar may be different in nature.

CONCLUSIONS

We detected GPs from the pulsar PSR B1112+50. At 111 MHz, the peak flux density of the strongest pulse is 180 Jy, which is almost a factor of 80 higher than the peak flux of the average pulse. Pulses whose peak intensities exceed the peak intensity of the average pulse by more than a factor of 30 occur

approximately once in 150 periods. The GPs are approximately a factor of 5 narrower than the average profile and they cluster in the middle part of the average profile. The brightness temperature of the observed GPs is $T_B \geq 10^{26}$ K.

ACKNOWLEDGMENTS

We are grateful to V. V. Ivanova and A. S. Aleksandrov for the assistance during observations. This work was supported in part by the Russian Foundation for Basic Research (project nos. 01-02-16326 and 00-02-17447) and the Program of the Presidium of the Russian Academy of Sciences "Nonstationary Processes in Astronomy."

REFERENCES

1. E. Argyle and J. F. R. Gower, Astrophys. J. Lett. **175**, L89 (1972).
2. J. Cognard, J. A. Shrauner, J. H. Taylor, and S. E. Thorsett, Astrophys. J. Lett. **457**, L81 (1996).
3. K. H. Hesse and R. Wielebinski, Astron. Astrophys. **31**, 409 (1974).
4. S. Johnston and R. W. Romani, Mon. Not. R. Astron. Soc. **332**, 109 (2002).
5. S. Johnston, W. van Straten, M. Kramer, and M. Bailes, Astrophys. J. Lett. **549**, L101 (2001).
6. A. Kinkhabwala and S. E. Thorsett, Astrophys. J. **535**, 365 (2000).
7. M. Kramer, S. Johnston, and W. van Straten, Mon. Not. R. Astron. Soc. **334**, 523 (2002).
8. A. D. Kuzmin, Astron. Zh. **79**, 501 (2002) [Astron. Rep. **46**, 451 (2002)].
9. A. D. Kuzmin and B. Ya. Losovsky, Pis'ma Astron. Zh. **26**, 581 (2000) [Astron. Lett. **26**, 500 (2000)].
10. A. D. Kuzmin and B. Ya. Losovsky, Pis'ma Astron. Zh. **28**, 25 (2002) [Astron. Lett. **28**, 21 (2002)].
11. S. M. Kutuzov, private communication (2000).
12. S. C. Lundgren, J. M. Cordes, M. Ulmer, *et al.*, Astrophys. J. **453**, 433 (1995).
13. S. Phinney and J. H. Taylor, Nature **277**, 117 (1979).
14. R. T. Ritchings, Mon. Not. R. Astron. Soc. **176**, 249 (1976).
15. R. W. Romani and S. Johnston, Astrophys. J. Lett. **557**, L93 (2001).
16. V. I. Shishov, V. M. Malofeev, A. V. Pynzar', and T. V. Smirnova, Astron. Zh. **72**, 485 (1995) [Astron. Rep. **39**, 428 (1995)].
17. D. H. Staelin and J. M. Sutton, Nature **226**, 69 (1970).
18. J. H. Taylor, R. N. Manchester, A. G. Lyne, *et al.*, Catalog of 706 Pulsars (1995), unpublished work.
19. A. Wolszczan, J. M. Cordes, and D. R. Stinebring, *Millisecond Pulsars,* Ed. by S. P. Reynolds and D. R. Stinebring (NRAO, Green Bank, 1984), p. 63.

Translated by A. Dambis

Astronomy Letters, Vol. 29, No. 2, 2003, pp. 96–104. Translated from Pis'ma v Astronomicheskiĭ Zhurnal, Vol. 29, No. 2, 2003, pp. 116–124.

Peculiarities of Processing VLBI Observations of Pulsars

K. V. Semenkov[1]*, M. V. Popov[1], V. A. Soglasnov[1], and H. Hirabayashi[2]

[1] *Astrospace Center, Lebedev Physical Institute, Russian Academy of Sciences, Profsoyuznaya ul. 84/32, Moscow, 117810 Russia*

[2] *Japanese Institute for Aeronautics and Space Research, Sagamihara, Japan*

Received August 29, 2002

Abstract—We determined the features of pulsars that were disregarded in standard amplitude-calibration procedures for VLBI observations. We suggest additional amplitude-calibration methods. These methods were used to process the VLBI observations of the pulsar PSR B0329+54 carried out with the HALCA ground–space interferometer. Data from the space radio telescope are corrected for a nonuniform reception band. We estimated the diameter of the scattering disk for this pulsar at a frequency of 1600 MHz: $<1''.8 \times 10^{-3}$. © *2003 MAIK "Nauka/Interperiodica".*

Key words: *pulsars, neutron stars, and black holes.*

INTRODUCTION

The overwhelming majority of VLBI experiments are observations of extragalactic sources. Therefore, the AIPS (NRAO) and DifMap (CalTech) post-correlation data processing software packages are naturally designed to process precisely this type of data. The radio emission from pulsars exhibit features that are disregarded by the standard data processing packages. From an observational point of view, the pulsars are compact (less than $1'' \times 10^{-7}$ in angular size) periodic sources of pulsed radio emission. The pulse repetition periods range from 1.5 ms to 8.5 s; the pulse duration is generally less than 0.1 of the period. The pulsars are highly variable sources whose radio intensity varies randomly from pulse to pulse (the modulation index is $\langle \delta I^2 \rangle / \langle I \rangle^2 \approx 1$, where I is the intensity of the received emission and the angular brackets denote averaging), although each pulsar is characterized by a certain fluctuation spectrum.

The radio emission from pulsars is scattered by interstellar electron plasma inhomogeneities. The effects that are important for VLBI observations include interstellar dispersion, scintillations, distortions of the frequency radiation spectrum by scattering, and angular broadening of the source. We will describe how these effects show up in observational data and how they should be taken into account.

PERIOD INCOMMENSURABILITIES

The correlator output contains the correlation functions integrated over some time interval (usually several seconds). At the same time, the pulsar period is generally incommensurable with the integration interval; i.e., the correlator integration interval includes a noninteger number of pulsar pulses. Therefore, the variations in the amplitude of the correlation function caused by this effect arise:

$$\frac{\{T_{\rm int}/P\}+1}{\{T_{\rm int}/P\}}, \qquad (1)$$

where $T_{\rm int}$ is the correlator integration interval, P is the pulsar period, and $\{\cdot\}$ is the integer part.

This effect is particularly noticeable if the correlation is done in the so called gate regime. The pulsar signal occupies about 10% of the period, while, during the remaining 90% of the time, noise is received. Hence, to increase the signal-to-noise ratio, the data should be correlated only within the time intervals containing the pulse. This correction method is called gating. The gating regime is realized on the VLBA (NRAO, USA; see Romney 1995; Benson 2000), S2 (Penticton, Canada; see Carlson *et al.* 1999), and K4 (Kashima, Japan, see Sekido 2001; Sekido *et al.* 1998) correlators. Using gating increases the signal-to-noise ratio by a factor of $\sqrt{(T_{\rm int}/kW_{\rm g})}$, where k is the number of pulses within the integration interval (generally, a noninteger number) and $W_{\rm g}$ is the correlator gate width, but also increases the beating in the amplitudes of the correlation functions (see Fig. 1).

For many problems that do not require accurate amplitude calibration, for example, for pulsar parallax and proper motion determinations, period incommensurability may be disregraded. In addition, if

*E-mail: kirill@anubis.asc.rssi.ru

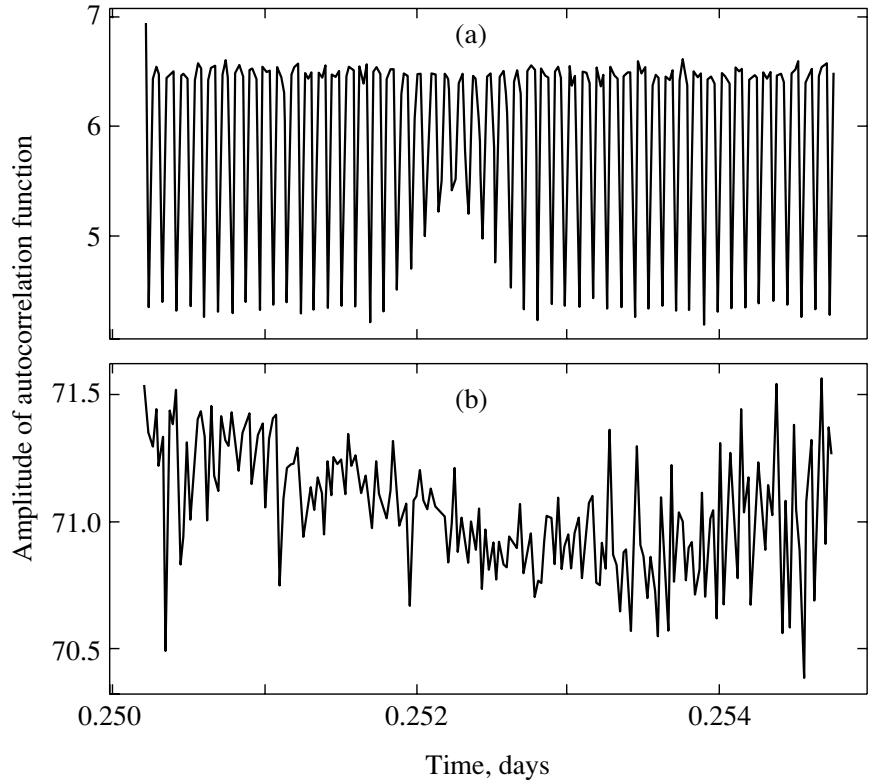

Fig. 1. Results of the correction for incommensurability of the pulsar period and the correlator integration interval: the data before (a) and after (b) the correction. The amplitude of the autocorrelation function is plotted against time for the Fort Davis antenna.

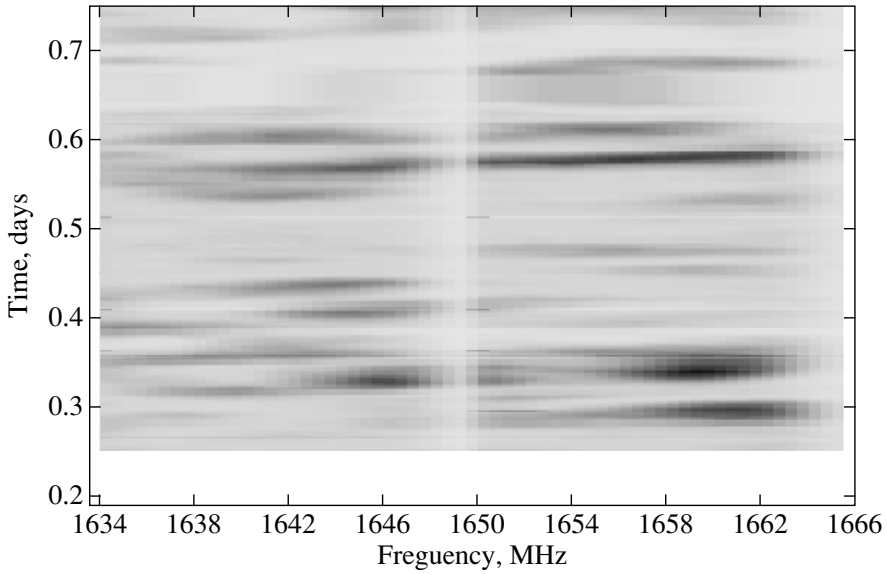

Fig. 2. The dynamic cross spectrum (time variation of the power cross spectrum) for the pulsar PSR B0329+54. The correction methods described here were not used to obtain the dynamic spectrum. The amplitude calibration was made in the AIPS package; the spectra from all antennas were then summed and averaged over 1 min.

the pulsar period is much shorter than the correlator integration time, the beating becomes negligible. If, however, accurate amplitude calibration is required, then the correlation functions must be corrected for

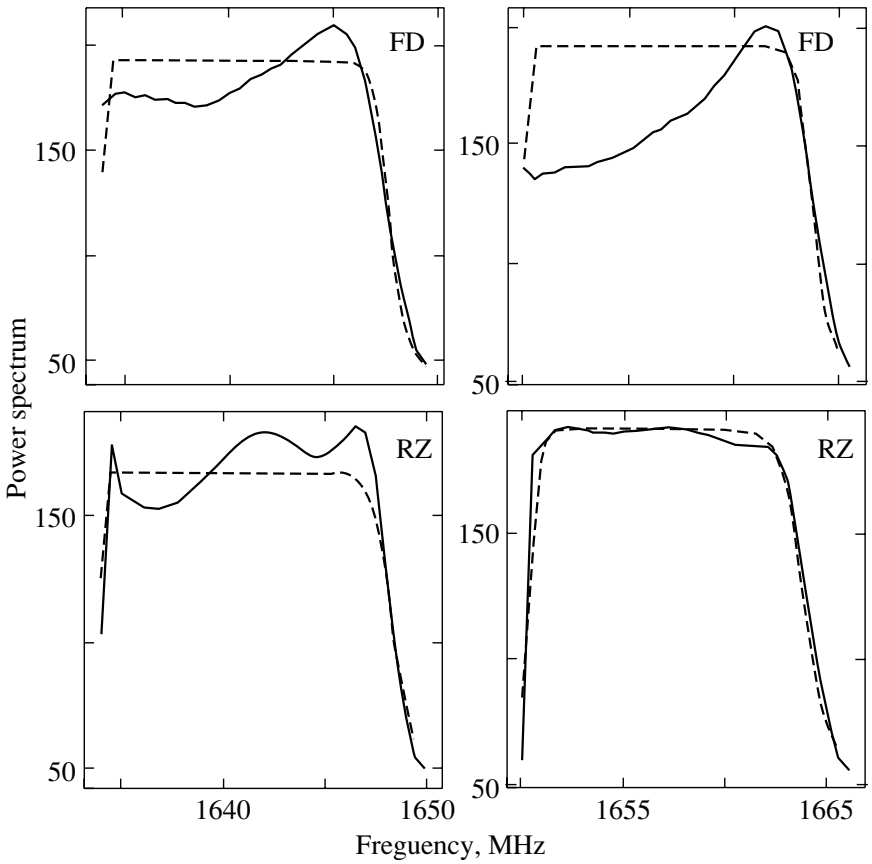

Fig. 3. Results of the correction for a nonuniform reception band for the Fort Davis (FD) and space radio telescope (RZ) antennas. The power spectrum of the signal from PSR B0329+54 is shown; the spectrum integration interval is approximately 1.96 s (the correlator integration time). The solid and dashed lines represent the noncorrected and corrected spectra, respectively.

incommensurability of the correlator integration interval and the pulsar period using the formula

$$C_c = \frac{C_n}{kW_g/T_{int}}, \qquad (2)$$

where C_c is the corrected correlation function and C_n is the noncorrected correlation function.

The quantity kW_g for the observed pulsar depends on the gating model used on the correlator. It is desirable that the table of kW_g values be contained in the data obtained from the correlator, as is the case, for example, on the VLBA correlator, where the output contains a table of coefficients kW_g/T_{int}.

THE CORRECTION FOR A NONUNIFORM RECEPTION BAND

Interstellar scattering severely distorts the pulsar radio spectrum (see Fig. 2). The characteristic "scintillation spots" caused by the loss of signal coherence in frequency and time intervals exceeding the characteristic values appear in the source dynamic spectrum, i.e., in the dependence of the signal power on frequency and time. These characteristic values are called the decorrelation band and scintillation time, respectively. For example, for PSR B0329+54, the decorrelation band at a frequency of 1.6 GHz is about 10 MHz and the scintillation time is about 15 min (the estimate was obtained by interpolating the data from Popov and Soglasnov (1984) and Kondrat'ev *et al.* (2001). In addition, the reception band has a certain amplitude–frequency characteristic typical of the receiving–recording complex on a given radio telescope, and it is first necessary to make a correction for the amplitude–frequency characteristic.

The band correction methods for ground-based VLBI systems have long been known. They were developed and implemented in VLBI data processing software packages, for example, in the AIPS (Astronomical Image Processing System) package, which is a standard software product used to process astrophysical VLBI data. The point is that, during the session of a ground-based VLBI experiment, one or more extragalactic pointlike reference sources are commonly observed (calibrators). Since the calibra-

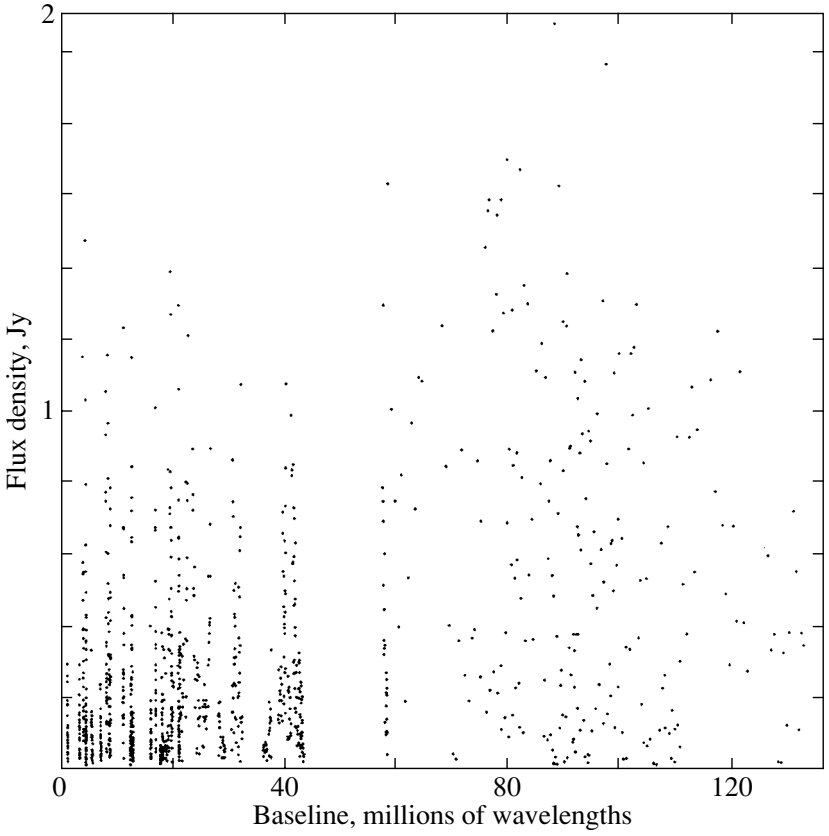

Fig. 4. The amplitude of the visibility function versus baseline. The correction methods described here were not used to obtain this dependence. The amplitude calibration was made in the AIPS package; the data were then averaged over time within 1 min.

tor spectrum is generally noisy, it is assumed that the deviation of the power spectrum for a reference source from the ideal band shape is caused by instrumental effects, the calibration function is calculated, and the calibration results are applied to the main-source data. However, this technique cannot be used to processes the pulsar observations with a ground–space interferometer, because the space radio telescope cannot observe calibration sources because of its pointing peculiarities. However, if there are observations of a noise source with a space radio telescope carried out at a different time, then one can attempt to correct the data for a nonuniform reception band of the space radio telescope by assuming that it did not change significantly in the time elapsed between the two observations.

To calibrate the pulsar observational data, we wrote a software package based on CFITSIO (http://heasarc.gsfc.nasa.gov/docs//software/fitsio/fitsio.html), a library of functions working with FITS data. The VLBI observational data in the FITS file are recorded as the spectra averaged over the correlator integration time (several seconds). The record contains only harmonics with positive numbers. Harmonics with negative numbers can be restored by using the relation

$$A(-j) = A^*(j), \quad C(-j) = 0, \quad j = 1, \ldots, N,$$

where $A(j)$ is the power spectrum, $C(j)$ is the power cross spectrum, N is the number of harmonics (spectral channels), and * denotes a complex conjugate. Since the power spectrum is a real quantity, we have $A^*(j) = A(j)$.

We obtained the noise power spectrum by averaging the autospectra of extragalactic calibration sources. Next, the correction for a nonuniform band for each of the antennas was made as follows.

(1) The mean power spectrum $A_{\rm ref}(j)$ of the reference source (in this section, j is the frequency channel number) was computed for each antenna.

(2) The function $B_{\rm id}(j)$ that specifies the ideal reception band is chosen. In the simplest case, the band is rectangular ($B_{\rm id}(j) = {\rm const}$); however, the actual band falls off to the edges in some, occasionally large frequency range. Therefore, as $B_{\rm id}(j)$, we used a function that also fell off to the edges (see. Fig. 3):

$$B_{\rm id}(j) = \begin{cases} \dfrac{B_{\max} - B_{\min}}{\sqrt{1 + \exp\dfrac{(j - j_{\rm l})(j - j_{\rm r})}{\gamma_{\rm l}(j_{\rm r} - j_{\rm l})}}} + B_{\min}, & 0 \le j \le N/2 \\ \delta\dfrac{B_{\max} - B_{\min}}{\sqrt{1 + \exp\dfrac{(j - j_{\rm l})(j - j_{\rm r})}{\gamma_{\rm r}(j_{\rm r} - j_{\rm l})}}} + B_{\min}, & N/2 < j \le N, \end{cases} \quad (3)$$

$$\delta \stackrel{\rm def}{=} \frac{\sqrt{1 + \exp\dfrac{(N/2 - j_{\rm l})(N/2 - j_{\rm r})}{\gamma_{\rm r}(j_{\rm r} - j_{\rm l})}}}{\sqrt{1 + \exp\dfrac{(N/2 - j_{\rm l})(N/2 - j_{\rm r})}{\gamma_{\rm l}(j_{\rm r} - j_{\rm l})}}},$$

where $B_{\max}$ and $B_{\min}$ are the maximum and minimum values of the power spectrum $A_{\rm ref}(j)$, respectively; B is the reception bandwidth; $j_{\rm l}$ and $j_{\rm r}$ are the lower and upper boundaries of the ideal band; $\gamma_{\rm l}$ and $\gamma_{\rm r}$ are the slopes of the left and right band wings; and δ is the amplitude joining coefficient. At this stage, the boundaries of the ideal band and the slopes of the edges are specified by the operator; we used $j_{\rm l} = 1$, $j_{\rm r} = 27$, $\gamma_{\rm l} = 6000$, $\gamma_{\rm r} = 35\,000$.

(3) The correcting function of the amplitude spectrum is calculated:

$$F_{\rm corr}(j) = \sqrt{B_{\rm id}(j)/A_{\rm ref}(j)}.$$

(4) The power cross spectrum is corrected for a nonuniform reception band:

$$C^{lm}_{\rm corr}(j) = C^{lm}_{\rm real}(j) F^{l}_{\rm corr}(j) F^{m}_{\rm corr}(j),$$

where $C^{lm}_{\rm corr}(j)$ is the corrected power cross spectrum, $C^{lm}_{\rm real}$ is the noncorrected power cross spectrum, the superscripts l and m are the numbers of the antennas involved in the correlation.

Figure 3 presents the results of the band correction for one of the ground-based antennas and for the HALCA space radio telescope.

THE CORRECTION FOR INTRINSIC VARIABILITY AND FOR SCINTILLATION-RELATED VARIATIONS

The intrinsic variability of pulsar radio emission (the emission intensity greatly varies from pulse to pulse) and the variability attributable to interstellar scintillations distort the dependence of the amplitude of the visibility function on baseline. (see Fig. 4). In imaging, the data are usually averaged over several minutes. If the pulsar is a short-period one (its period is much shorter than the averaging interval) or if the scattering is large (the decorrelation time is shorter than the averaging interval and the decorrelation band is much narrower than the reception bandwidth), then this averaging procedure can actually considerably reduce the effect of pulsar variability. However, one or both above conditions are often not satisfied. An example is the pulsar PSR B0329+54 with a period of 0.714 s and a decorrelation time of ~15 min at a frequency of 1.6 GHz. One or two minutes of averaging are sufficient neither to obtain the average pulse profile nor to average the scattering effects. The intrinsic short-period pulsar variability should not affect the image quality, but it must be taken into account in flux calibration, while scintillations can generally give rise to spurious features in the image and can make it difficult to interpret the results obtained.

The variability effects could be easily taken into account if each antenna recorded the intensities of individual pulsar pulses. However, the currently available VLBI terminals are not equipped with such recorders of the detected signal. Therefore, we propose to extract information on the relative power of the variable pulsar signal from comparison of the autocorrelation functions obtained on a correlator in the "gating" regime and in the "standard" regime.

Indeed, let $A_{\rm g}$ and $A_{\rm k}$ be the autocorrelation functions obtained in the "gating" and "standard" correlation regimes, respectively. For each antenna, they can be expressed in terms of the noise and signal powers as

$$A_{\rm g} = W_{\rm g} S_{\rm n}^2 + S_{\rm s}^2,$$
$$A_{\rm k} = W_{\rm k} S_{\rm n}^2 + S_{\rm s}^2,$$
$$W_{\rm g} = g W_{\rm k},$$

where the coefficient g is assumed to be known, $W_{\rm k}$ is the correlator integration time (usually several seconds), $W_{\rm g}$ is the total duration of the correlator gates within the integration interval, $S_{\rm n}^2$ is the noise power, and $S_{\rm s}^2$ is the signal power. Hence, we obtain

$$S_{\rm s}^2 = \frac{A_{\rm g} - g A_{\rm k}}{g(1 - g)}. \quad (4)$$

Next, we assume that on small baselines, the source is not resolved. Consequently, the expected visibility function on short baselines is

$$|V_{ij}^{\rm exp}| = \sqrt{S_{i,{\rm s}}^2 S_{j,{\rm s}}^2}, \quad (5)$$

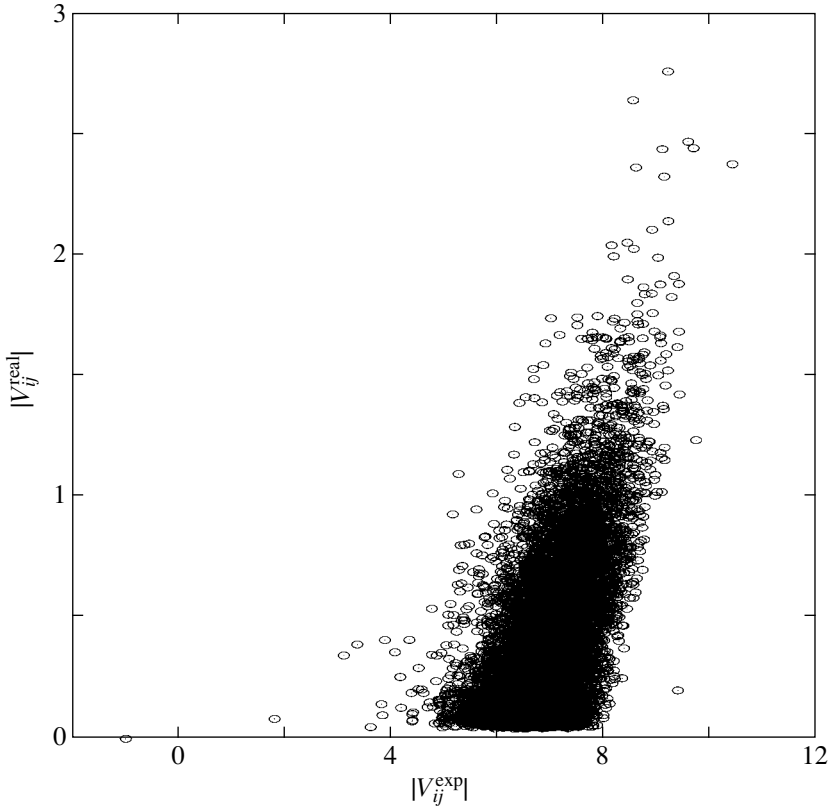

Fig. 5. The real amplitudes of the visibility function *versus* the expected visibility function $|V_{ij}^{\mathrm{exp}}|$ on the Fort Davis–Kitt Peak baseline.

where the subscripts i and j denote the antenna numbers. The actual visibility functions can then be corrected using the formula

$$V_{ij}^{*} = V_{ij}/|V^{\mathrm{exp}}|, \tag{6}$$

where $|V^{\mathrm{exp}}|$ is the result of averaging (5) over all small baselines.

REAL DATA PROCESSING

We used the approach described in previous sections to process the VLBI observations of the pulsar PSR B0329+54. The goal of these observations was to measure the circle of confusion for the pulsar. The diameter of the scattering disk is one of the parameters that describe interstellar electron plasma turbulence.

The visibility function from a source whose emission has passed through scattering plasma is known (see, e,g., Cordes *et al.* 1985) to be

$$V(\mathbf{r}) = V_0(\mathbf{r}) \exp\left[-D(\mathbf{r})/2\right]. \tag{7}$$

Here, $\mathbf{r}$ is the baseline vector, $V_0(\mathbf{r})$ is the visibility function in the absence of scattering, and $D(\mathbf{r})$ is the phase structural function, defined as

$$D(\mathbf{r}) \stackrel{\mathrm{def}}{=} \langle[\varphi(\mathbf{s}+\mathbf{r}) - \varphi(\mathbf{s})]^2\rangle$$

$$= 8\pi r_{\mathrm{e}}^2 \lambda^2 \int dz' \int dq\, q[1 - J_0(qr)P(q, z'),$$

where r_{e} is the classical electron radius, λ is the emission wavelength, $P(q, z')$ is the spatial spectrum of electron plasma density inhomogeneities. If the inhomogeneity spectrum is a power law (e.g., a Kolmogorov one), i.e.,

$$P(q) = C_{\mathrm{n}}^2 q^{-\gamma}, \quad q_0 \le q \le q_1, \quad C_{\mathrm{n}}^2 = \mathrm{const},$$

then formula (7) becomes

$$V(\mathbf{r}) = V_0(\mathbf{r}) \exp\left[-(r/r_{\mathrm{c}})^{\gamma-2}\right]. \tag{8}$$

The angle $\theta_{\mathrm{s}} = \lambda/2\pi r_{\mathrm{c}}$ is called the scattering angle or the angular diameter of the scattering disk and the quantity r_{c} is related to the coefficient C_{n}^2:

$$r_{\mathrm{c}} \propto \left[LC_{\mathrm{n}}^2 \frac{\Gamma(2-\gamma/2)}{(\gamma-2)(\Gamma(\gamma/2))}\right]^{-1/(\gamma-2)},$$

where $\Gamma(\cdot)$ is the gamma function. Thus, measuring the scattering angle can give information on the nature of the line-of-sight turbulence. VLBI observations provide a direct method for measuring the scattering disk and can also be used to check other methods of estiming this quantity.

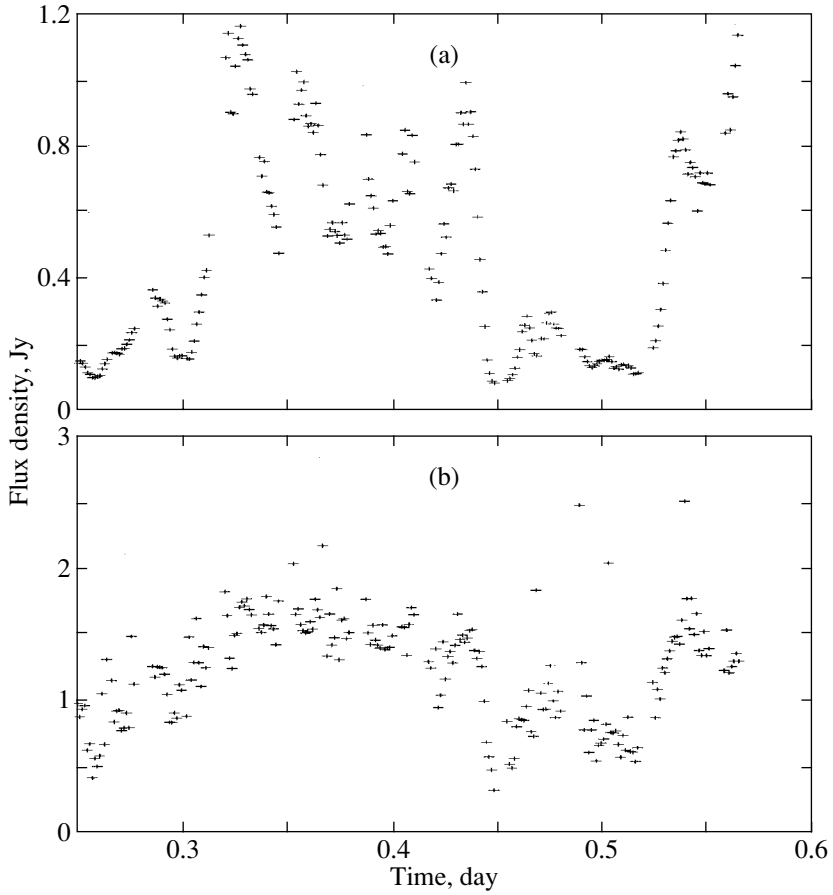

Fig. 6. The amplitude of the visibility function versus time before (a) and after (b) the correction for intrinsic variability and scintillation-related variations. The data were averaged over frequency within the band, over time within 1 min, and over all baselines.

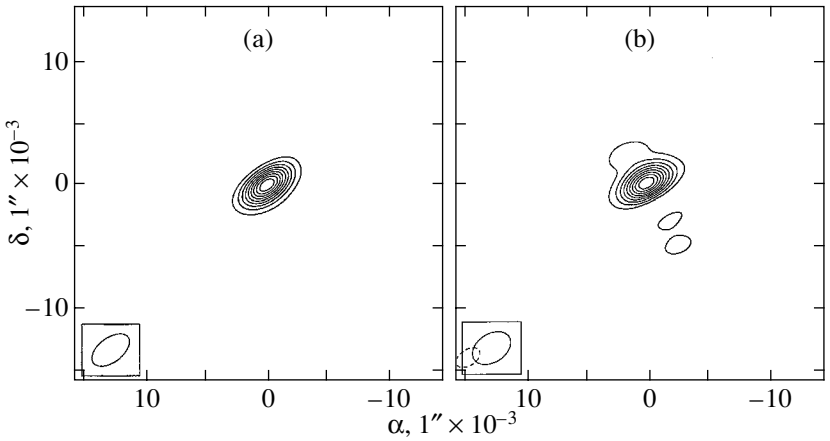

Fig. 7. The image of PSR B0329+54 after one self-calibration cycle: the images constructed from (a) corrected and (b) noncorrected data.

PSR B0329+54 (J0332+5434) is one of the brightest pulsars; its period-averaged flux density at a frequency of 1.4 GHz is 200 mJy, the period is 0.714 s, the dispersion measure is 26.8 pc cm^{-3}, and the equivalent pulse width is 8.7 ms (Taylor *et al.* 1993). The VLBI observations of this object aimed at measuring the circle of confusion were also carried out previously. Thus, for example, Britton

et al. (1998) observed several pulsars, including PSR B0329+54, during an intercontinental VLBI experiment at a frequency of 323 MHz. They were unable to resolve the scattering disk; based on indirect data, they estimated its size to be $4''.3 \times 10^{-3}$. Bartel *et al.* (1985) observed the pulsar at 2.3 GHz; the following three telescopes were involved in this experiment: Effelsberg (Germany), Green Bank (USA), and Owens Valley (USA). The authors obtained an upper limit on the diameter of the scattering disk, $1'' \times 10^{-3}$.

Using the HALCA space radio telescope allows us to increase the angular resolution and to measure the diameter of the scattering disk more accurately: the maximum angular resolution of the ground–space interferometer at a frequency of 1.6 GHz is approximately $1''.5 \times 10^{-3}$.

The observations were carried out on August 22, 1998, during 12 h. Eleven antennas, including eight antennas of the VLBA network, two DSN antennas, and the HALCA space radio telescope, were involved in them. The data were recorded in two adjacent 16-MHz bands at frequencies of 1634 and 1650 MHz. The correlation was done on the VLBA NRAO correlator in the "gating" and "standard" regimes. The correlator integration interval was ~2 s; the data in each of the bands were broken down into 32 500-kHz frequency channels.

As we see from Fig. 2, which shows the average power cross spectrum, the scintillations are strong; the duration of the scintillation spot is 20–30 min.

The data were sequentially corrected for a nonuniform reception band, for incommensurability of the pulsar period and the correlator integration time, and for source variability.

Figure 3 shows the power autospectra of the pulsar radio emission for the ground-based antenna (as an example, the Fort Davis antenna of the VLBA network was chosen) and for the HALCA space radio telescope before and after the corrections for a nonuniform reception band. To correct the HALCA reception band, we used the observational data for the source J0238+16 provided by L.I. Gurvits (JIVE, Holland).

Figure 1 shows the results of the data correction for incommensurability of the pulsar period and the correlator integration time.

Subsequently, we made the correction for source variability. Because of the scaling effects of the autocorrelation functions on the correlator, the values of $|V_{ij}^{\rm exp}|$ calculated with formula (5) differ from the real values of $|V_{ij}|$. The dependence of $|V_{ij}^{\rm exp}|$ on $|V_{ij}|$ was found to be satisfactorily fitted by a linear function: $|V_{ij}^{\rm real}| = A|V_{ij}^{\rm exp}| + b$ (see Fig. 5). The coefficients of the linear function were determined by the bisector least-square method (Isobe and Feigelson 1990) for each baseline and each intermediate frequency. Since these coefficients for each pair of the antennas slightly differ, we used the values averaged over short (less than 1000 km) baselines: $a = (0.52 \pm 0.01,\ 0.54 \pm 0.01)$, $b = (-3.172 \pm 0.03,\ -3.174 \pm 0.03)$. The two values of a and b correspond to the two intermediate frequencies (1634 and 1650 MHz). After the correction of the relation between $|V_{ij}^{\rm exp}|$ and $|V_{ij}|$ by our technique, we made the correction using formula (6).

It turned out that the procedure of correction for source variability eliminated the systematic variation in the amplitude of the visibility function due to scintillations but the spread in corrected values remained significant, approximately 0.9 (see Fig. 6). This is presumably because rapid source variability is disregarded for the existing technique of observations and correlation of pulsar data. It results in the violation of the conditions optimal for two-bit signal quantization, which distorts the correlation function [see Chapter 8 in Thompson *et al.* (1986) and Kogan (1995)]. To compensate for these intensity variations, an automatic gain control (AGC) system is included in the receiving channels. However the AGC system has a certain triggering time constant and is not designed to track short pulsar pulses. Note that when deriving formula (4) we assumed the receiving channel gain to be constant, i.e., we ignored the AGC effect.

Thus, the technique for VLBI observations of pulsars must be changed. More specifically, AGC must be switched off and the intensities of individual pulsar pulses must be recorded independently on each of the antennas involved in the VLBI experiment.

The data corrected for the three effects described above were saved in FITS format and subsequently processed using the AIPS package. We made amplitude calibration, a global lobe search, time averaging of the data, and self-calibration imaging (see Fig. 7). Note that we were unable to reproduce the processing results of the same experiment obtained by Minter (2000), i.e., to construct a double image of the pulsar, with and without additional amplitude correction. Therefore, we consider that in this case the double-image effect is spurious.

The proposed amplitude calibration methods allow us to obtain an image of acceptable quality with a smaller number of iterations. However, the unremoved large spread in amplitudes does not allow us to accurately measure the scattering disk. Analysis of our images suggests that the source could not be resolved and that the diameter of the scattering disk is $\theta_{\rm s} < 1''.8 \times 10^{-3}$. This result is consistent with a priori estimates of $\theta_{\rm s}$.

CONCLUSIONS

When processing the VLBI observations of PSR B0329+54, we found that the data calibration methods existing and implemented in standard data processing packages, disregard some pulsars features, more specifically, the pulsed pattern of the emission, intrinsic amplitude variability, amplitude and frequency scintillations. We proposed calibration methods that took into account these features and applied them to the observations of PSR B0329+54. The correlated data have retained a considerable spread in values (about 0.9). The presumed cause of this effect is that the "standard" VLBI signal recording technique is not applicable to pulsars. We estimated the diameter of the scattering disk for this pulsar to be $\theta_s < 1''.8 \times 10^{-3}$.

ACKNOWLEDGMENTS

We wish to thank J. Benson (NRAO, USA) for consultations on the issues related to gating regime on the VLBA NRAO correlator, E. Fomalont (NRAO, USA) for advice on source imaging, and L.I. Gurvits (JIVE, Holland) whose provided the observational data obtained for J0238+16 with the HALCA space radio telescope. This work was supported by the Russian Foundation for Basic Research (project no. 01-02-16871) and the Program of the Presidium of the Russian Academy of Sciences "Nonstationary Phenomena in Astronomy." We are grateful to the VSOP project operated by the Japanese Institute of Space and Astronautical Science in cooperation with numerous organizations and radio telescopes of the world.

REFERENCES

1. N. Bartel, M. I. Ratner, I. I. Shapiro, *et al.*, Astron. J. **90**, 2532 (1985).
2. J. Benson, *Implementing the Pulsar Gate in the VLBA Correlator,* http://www.aoc.nrao.edu/jbenson/pulsar_gate.ps (2000).
3. M. C. Britton, C. R. Gwinn, and M. J. Ojeda, Astrophys. J. Lett. **501**, L101 (1998).
4. B. R. Carlson, P. E. Dewdney, T. A. Burgess, *et al.*, Publ. Astron. Soc. Pac. **111**, 1025 (1999).
5. J. M. Cordes, J. M. Weisberg, and V. Boriakoff, Astrophys. J. **288**, 221 (1985).
6. T. Isobe and E. D. Feigelson, Astrophys. J. **364**, 104 (1990).
7. L. Kogan, VLBA Sci. Memo. No. 9 (1995).
8. V. I. Kondratiev, M. V. Popov, V. A. Soglasnov, and S. V. Kostyuk, Astrophys. Space Sci. **278**, 43 (2001).
9. A. Minter, in *Proceedings of the VSOP Symposium,* Ed. by H. Hirabayashi, P. G. Edwards, and D. W. Murphy (ISAS, Sagamihara, Japan, 2000), p. 113.
10. M. V. Popov and V. A. Soglasnov, Astron. Zh. **61**, 727 (1984) [Sov. Astron. **28**, 424 (1984)].
11. J. D. Romney, Bull. Am. Astron. Soc. **27**, 815 (1995).
12. M. Sekido, *Pulsar Astrometry by VLBI,* PhD Theses (Grad. Univ. Adv. Stud., Tokyo, 2001).
13. M. Sekido, S. Hama, H. Kiuchi, *et al.*, Astron. Soc. Pac. Conf. Ser. **144**, 403 (1998).
14. J. H. Taylor, R. N. Manchester, and A. G. Lyne, Astrophys. J., Suppl. Ser. **88**, 529 (1993).
15. A. R. Thompson, J. M. Moran, and G. W. Swenson, Jr., *Interferometry and Synthesis in Radio Astronomy* (Wiley, New York, 1986; Mir, Moscow, 1989).

Translated by V. Astakhov